Department of Physics
Imperial College London

Interpreting atmospheric escape observations from close-in exoplanets

Ethan Schreyer

Submitted in part fulfilment of the requirements for the degree of
Doctor of Philosophy at Imperial College London, October 2024

Copyright Declaration

Statement of Originality

This thesis is my own work, except where specifically indicated in the text. Some parts of this thesis are based on work completed in collaboration with others, and some have also been published as journal articles:

- Chapter 2 is based on work that has been completed in collaboration with J. E. Owen, R. O. P. Loyd and R. Murray-Clay, and is published as:

  ***Schreyer E.**, Owen J. E., Loyd R. O. P., Murray-Clay R. Using Lyman-α transits to constrain models of atmospheric escape, MNRAS, 533, 3296 (2024)*

  In this work, I developed the model and ran the retrieval. R. O. P. Loyd reduced the HST data. J. E. Owen and R. Murray-Clay provided discussion and advice.

- Chapter 3 is based on work that has been completed in collaboration with J. E. Owen, J. J. Spake, Z. Bahroloom, S. Di Giampasquale, and is published as:

  ***Schreyer E.**, Owen J. E., Spake J. J., Bahroloom Z., Di Giampasquale S. Using Helium 10830 Å transits to constrain planetary magnetic fields, MNRAS, 527, 5117 (2024)*

  In this work, I ran the all models. Z. Bahroloom and S. Di Giampasquale performed proof of concept work. J.E Owen and J. J. Spake provided discussion and advice.

- Chapter 4 is based on ongoing work in collaboration with R. Murray-Clay

  In this work, I ran all the models. R. Murray-Clay provided discussion and advice.

- Chapter 5 is based a paper that has completed with the authors listed below, led by R. O. P Loyd and a successful Hubble Space Telescope Proposal, led by R. O. P Loyd and S. Vissapragada.

  *Loyd, R. O. P., **Schreyer, E.**, Owen, J. E., Rogers, J. G., Broome, M., Shkolnik, E., Murray-Clay, R., Wilson, D. J., Peacock, S., Teske, J., Schlichting, H. E., Duvvuri, G. M., Youngblood, A., Schneider, P. C., France, K., Giacalone, S., Batalha, N. E., Schneider, A., Longo, I., Barman, T., Ardila, D. R., Hydrogen Escaping from a Pair of Exoplanets Smaller than Neptune, Nature, 638, 8051, 636-639, (2025)*

  In this work, I ran the retrievals.

  HST Program 17804: STELα: Survey of Transiting Exoplanets in Lyman-alpha

In this proposal, I produced synthetic Lyman-α transits for $\sim$ 200 planets to determine the optimal targets to observe.

Abstract

Exoplanet searches have uncovered a large population of planets at small orbital separations. Due to the proximity of these planets to their host stars, they receive intense irradiation. This irradiation intensely heats the upper atmospheres of the planets, making them susceptible to undergoing hydrodynamic escape. For small, gas-rich planets, the cumulative effect of this mass loss is thought to be capable of stripping their primordial atmospheres. Evolutionary modelling of this process is used to infer the properties of the planet population at birth. However, the inferred planetary properties are sensitive to modeled escape rates, so accurate escape models are necessary to ensure confidence in any conclusions. Direct observations of atmospheric escape from transiting exoplanets provide an opportunity to test these models. This thesis focuses on modelling hydrodynamic escape, with the specific goal of using these models to interpret observations.

Acknowledgements

I owe my deepest gratitude to many people, without whom my time at Imperial would not have been as successful or fulfilling.

Firstly, I extend my sincere thanks to my supervisor, James. Without you, I would not have found my way into exoplanetary science (which I'm counting as a positive thing!). Your support, advice, and patience throughout my PhD has been invaluable, and it has been a privilege to work with you. Thank you also to Ruth for mentoring me in my last year.

I am profoundly grateful to my parents and siblings, whose scientific curiosity and unwavering support made it possible for me to embark on this journey in the first place. You have always been and continue to be there for me. I hope I have made you proud.

To the entire Stars and Planets Group, thank you for fostering a rare community—one that has been both scientifically inspiring and personally enriching. Your friendship has made coming to work a true pleasure.

To my housemates Harry, Jimmy and Luke, thanks for creating a wonderful, and enjoyable place away from work. The past three and half years living together has been immense fun.

To my partner Georgia, whose support and companionship during the last years of my PhD helped me get over line.

Contents

List of Tables

List of Figures

Chapter 1

Introduction

One of the most intriguing questions in astronomy is how similar or different other planetary systems are compared to our own. This question remained largely unexplored until 1992, when the discovery of two planets orbiting the pulsar PSR 1257 + 12 marked a breakthrough moment in planetary science (Wolszczan & Frail, 1992). Just a few years later, the detection of 51 Pegasi b in 1995 (Mayor & Queloz, 1995), the first planet found orbiting a Sunlike star, opened the door to a new era of exoplanet exploration. In the past 30 years, the field has undergone a revolution, with over 5,000 exoplanets discovered, many of which are unlike anything in our Solar System.

Despite this rapid growth, exoplanet science is still in its infancy, with many mysteries left to unravel. Characterizing these distant worlds is a complex challenge. Many of the key properties we would like to know about exoplanets cannot be observed directly, and unlike planets in our Solar System, we cannot send probes to explore them in situ. Therefore, theoretical models are essential for interpreting observations and inferring crucial information about exoplanets. One such observable process is atmospheric escape, which plays a pivotal role in planetary evolution. By studying atmospheric escape in detail, we can gain valuable insights into the composition, formation, and evolution of these planets.

In this thesis, I will explore the theoretical modeling of atmospheric escape and examine what insights can be gained from direct observations of this process.

1.1 Exoplanet Detection and Demographics

Presently, there are more than 5,700 confirmed exoplanets, as reported by the NASA Exoplanet Archive. These are shown in Figure 1.1, labeled by the detection method. Of these techniques, transits and radial velocity searches have dominated the number of detections. Both these methods are more sensitive to large planets that are close to their host stars, which is why the observed exoplanet planet distribution is heavily weighted towards close-in exoplanets. As other methods, such as direct imagining, astrometry and microlensing, which have a greater sensitivity to longer period planets become more common, the current picture will radically change.

Transit Method

In the transit method, the flux of a potential planet-hosting star is measured for a period of time. If an orbiting planet passes in front of the star, the measured stellar flux will drop. The transit depth is defined as:

$$\delta \equiv \frac{F_{\text{out}} - F_{\text{in}}}{F_{\text{out}}}, \tag{1.1}$$

where F_{out} is the measured flux when the planet is not transiting the star and F_{in} in the measured flux when the planet is in transit. The transit depth represents the fraction of the stellar disk obscured by the planet during its transit (not accounting for any potential inhomogeneities in the stellar surface):

$$\delta \sim \left(\frac{R_p}{R_*}\right)^2. \tag{1.2}$$

where R_p is the radius of the planet and R_* is the radius of the star. The stellar radius is nowadays known fairly precisely from surveys such as Gaia, therefore the radius of the planet can be inferred from the transit depth. Multiple transits are needed to confirm the transit of a planet, from which a precise planetary orbital period can be measured. Using Kepler's laws and the measured stellar mass, the orbital separation of the planet can be calculated.

The measured transit depth depends on the wavelengths of light used to measure the flux of the

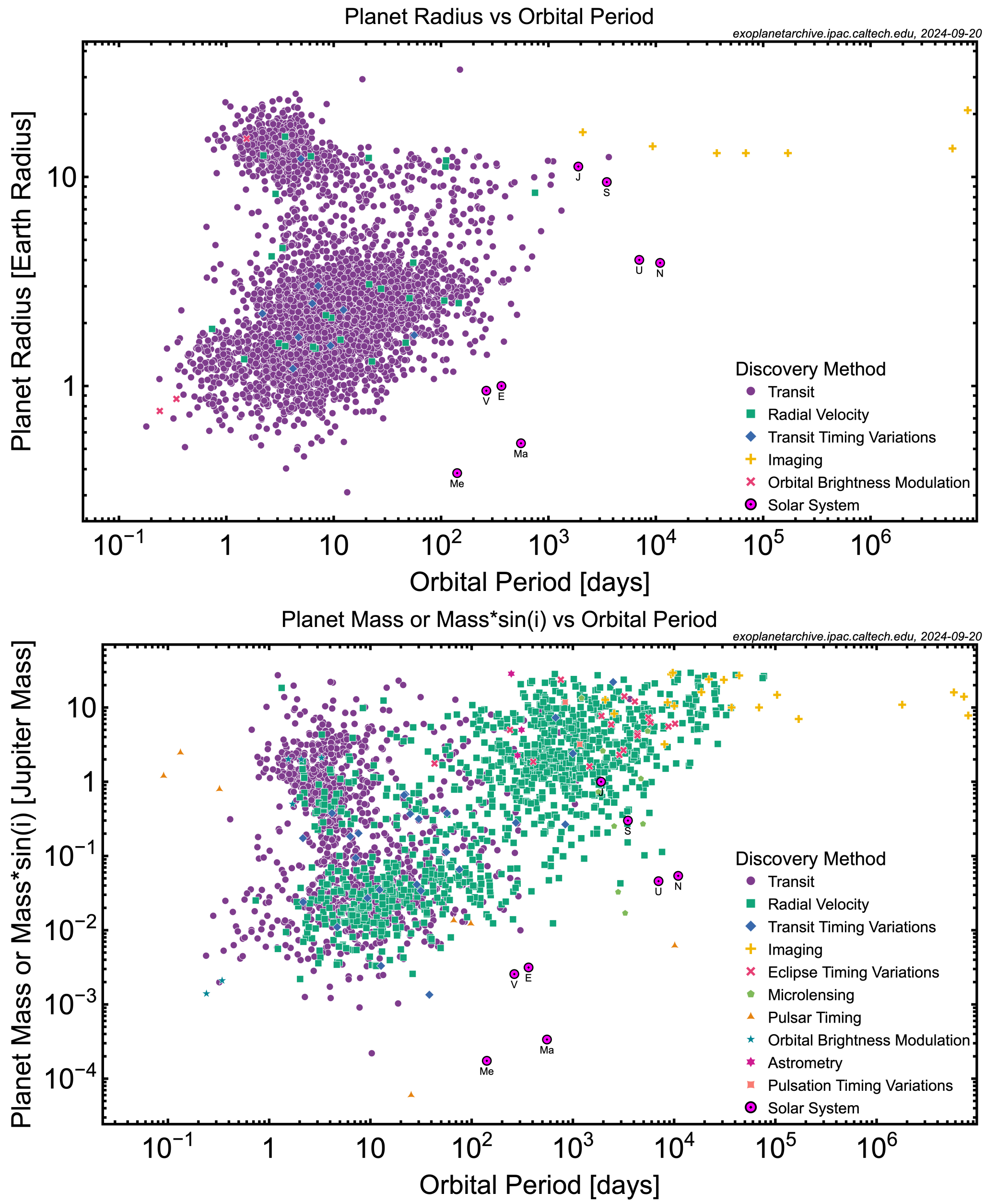

Figure 1.1: The population of confirmed exoplanets, labelled by the initial method of detection. The sample of planets in radius vs period plot (left) and the mass vs period plot (right) are different because all planets with measured radii have a measured mass and vice-versa. Data taken from NASA exoplanet archive, accessed 20/09/2024.

star. Transit surveys usually measure the broadband optical; therefore, the planet radius measured is the radius at which the planet becomes opaque to optical light. For planets without an atmosphere, this measures the radius of the surface. In contrast, planets with extended atmospheres become opaque to optical light at low pressures (Fortney, 2005), usually near the photosphere of the planet (Heng, 2017). Therefore, the atmosphere contributes to the transit depth. The optical depth of the atmosphere depends on the wavelength of light used; therefore, the observed planet radius is a function of wavelength. This forms the basis of transit spectroscopy, which is used to detect the presence of specific species in the atmospheres of planets.

Radial Velocity

The basis of the radial velocity technique is that planets exert a gravitational force on their parent star. As the star and planet rotate around the barycenter of the system, small changes in the projected velocity of the star cause the observed stellar lines to be Doppler-shifted. By measuring the Doppler shift of the stellar lines as a function of time, one can determine the orbital period of the planet and the quantity $M_{\mathrm{p}} \sin i$, where M_p is the mass of the orbiting planet, and i is the orbital inclination. Since $\sin \leq 1$, this places an upper limit on the mass of the orbiting planet. Radial velocity is the primary method used to measure a planet's mass, and often combined with transit data to find the planet's density, offering valuable insights into its composition.

Direct Imaging

In direct imaging, the light from the star and planet is spatially resolved, allowing for direct detection of the planet. Typically, this is achievable for young (and hence luminous) planets at long orbital periods. The fundamental property that direct imaging measures is the luminosity of the planet, which can be translated into a mass (with much uncertainty) using evolution models (Currie et al., 2023). Analyzing the emission spectrum of directly imaged planets enables the characterization of their atmospheres (Patapis et al., 2022; Currie et al., 2023).

Other Methods

At present, microlensing and astrometry have led to few detections; however, they are likely to lead to many more in the future (Green et al., 2012; Perryman et al., 2014). Microlensing works by measuring the light of a distant star. When a foreground star passes in front of this background star, gravitational lensing magnifies the light measured from the background star. If the foreground star has a planet orbiting it, the planet may produce a small secondary lensing event. The lensing event can be modelled to put constraints on the mass of the orbiting planet (Tsapras, 2018). An advantage of microlensing is that it can detect small planets at longer orbital periods than the transit or radial velocity methods, opening up a new parameter space to explore planets. However, these planets cannot be studied further, meaning that their atmospheres cannot be characterized. The upcoming *Nancy Grace Roman Telescope* is predicted to detect thousands of exoplanets (Green et al., 2012).

Astrometry precisely measures the position of a star in the sky over time, looking for small wobbles resulting from an orbiting planet. To get the astrometric precision required to distinguish these wobbles from the background motion of the star requires tracking of the star's position over a long period of time (> 5 years). ESA's Gaia mission is predicted to detect tens of thousands of exoplanets upon completion (Perryman et al., 2014).

Demographics

The diversity of observed planetary systems suggests that a variety of planet-forming environments, as well as different formation and evolutionary processes, are necessary to account for the observed planetary population. To advance our understanding, it is crucial to systematically characterize these planets.

As I have illustrated, the array of techniques and instruments used to detect exoplanets is diverse. These are sensitive to planets in some regions of parameter space and not others. For example, none of the current techniques are yet sensitive to Earth-like planets around solar-like stars. Therefore, the observed exoplanet population is a biased sample and an inaccurate representation of the true exoplanet population.

Demographic studies, which aim to reveal the underlying planet population from a detected sample by accounting for detection biases, play a key role in this effort. These studies help us to draw connections between the exoplanet population and the physical processes that govern the formation and evolution of planetary systems.

The largest-scale demographics survey to date was the *Kepler* mission. The space-based telescope continuously photometrically monitored $\sim 150,000$ stars in visible light (Borucki et al., 2011), with a magnitude-limited selection function that made it possible to quantify biases in the survey (Christiansen et al., 2013). This paved the way for rigorous estimates of planet occurrence rates (Howard et al., 2012; Ferraz-Mello, 2013a; Morton & Swift, 2014; Fulton et al., 2017; Dattilo et al., 2023). These studies revealed that planets with radii between Earth and Neptune, known as "super-Earths" and "sub-Neptunes" are ∼ 100 times more common than hot Jupiters (e.g., Dattilo et al., 2023)). Figure 1.2 shows the comparison between the observed planet population and the completeness-corrected intrinsic occurrence rate.

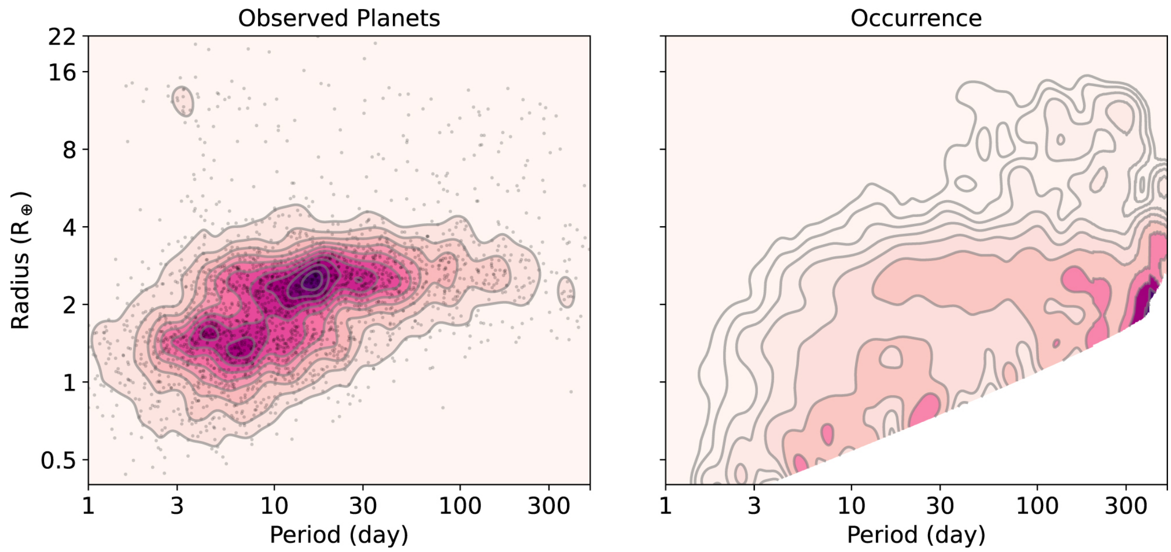

Figure 1.2: Kernel Density Estimator (KDE) maps of the FGK planet population observed by *Kepler* (left) and the completeness-corrected intrinsic occurrence (right). A darker colour corresponds to a higher density of planets. The structure of the maps is different, highlighting that observed planet frequency is not proportional to the intrinsic occurrence rate. For quantitative *Kepler* occurrence rate estimates, see Dattilo et al. (2023). Figure taken from Dattilo et al. (2023).

Kepler, as a transit survey, primarily measured the radii and orbital periods of planets. While useful, these two parameters alone provide limited information about a planet's composition and internal structure. Are these planets rocky worlds like those in the inner Solar System with thin/no atmosphere? Or are they more like ice giants, containing a mix of rock, hydrogen, helium, and volatile ices such as water and ammonia? Alternatively, could they be mini versions of gas giants like Jupiter and Saturn, with dense cores and thick hydrogen/helium atmospheres? Or might they represent a completely different type of planet?

To advance this understanding, follow-up radial velocity observations were conducted to determine the masses of some of these transiting planets. The bulk densities of these planets could be compared

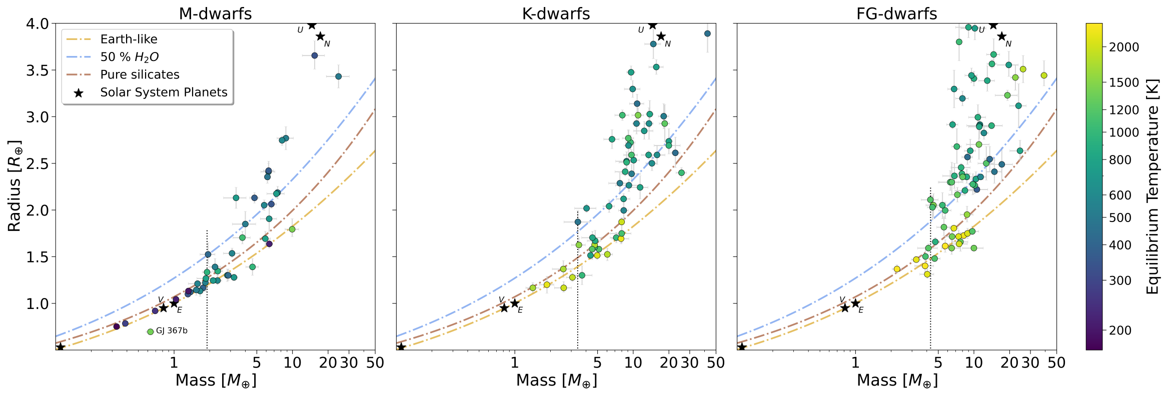

Figure 1.3: Mass-radius diagrams for observed exoplanets from the PlanetS catalog (Parc et al., 2024) The lines are mass-radius relations for planets of different compositions. Figure taken from Parc et al. (2024)

to theoretical structure models, to constrain possible compositions (see Figure 1.3). Many of these planets are consistent with having an Earth-like composition: a rocky composition of iron and magnesium silicates (Dressing et al., 2015). Others, however, are underdense, suggesting a substantial presence of volatiles. Some of these planets are so low in density that the only plausible explanation includes an extended hydrogen/helium atmosphere (e.g., Jontof-Hutter et al., 2016), while others exhibit intermediate densities which can be explained by a multitude of different compositions.

Other information must be used to break these degeneracies. One way to do this is studying the atmospheric composition of the planet using transit spectroscopy. The transformative *James Webb Space Telescope (JWST)* allows small planets to be observed from the visible to mid-infrared wavelengths (0.6 to 28 microns), where a host of molecular lines of C-, N-, O- and S- bearing species occur. These lines can be used to constrain the composition of the upper atmospheres of small planets to make inferences about the interior structure of the planet.

The modeling of these observations is still in its early stages, and theoretical uncertainties have led to a wide range of proposed atmospheric structures. For example, despite the detection of a variety of molecules in the atmospheres of K2-18 b and TOI-270 d, there is considerable disagreement regarding their planetary structures. (e.g., Madhusudhan et al., 2023; Wogan et al., 2024; Benneke et al., 2024)

Whilst K2-18 b and TOI-270 d are found to host clear atmospheres which aided the detection of molecules in their upper-atmospheres, other observed planets show remarkably featureless transmission spectrum (e.g., GJ1214 b Kreidberg et al. 2014; Kempton et al. 2023 or TOI-836 c Wallack et al. 2024). In this case, the high mean molecular weight and pressure of the opaque cloud layer are degenerate, so the atmospheric composition and consequently the structure of the planet cannot be tightly constrained.

Another approach to breaking the degeneracies in the composition of exoplanets is by tracing the evolutionary history of a planet. By studying the thermal, chemical, and dynamical processes that drive this evolution, we can link the observable features of a planet today to its composition, structure and formation history. The atmospheres of gas-rich exoplanets undergo significant evolution. Over time, these atmospheres cool and contract, while simultaneously being subjected to processes such as atmospheric escape and possible interactions with surface magma oceans on molten or rocky planets. For highly irradiated exoplanets, the escape of atmospheric gases, can dramatically alter the mass and composition of a planet's atmosphere, even stripping it entirely. Therefore, understanding atmospheric escape is key to characterizing the planet population.

1.2 Atmospheric Escape from Exoplanets: Theory

In the simplest terms, the physics of atmospheric escape is a competition between the kinetic energy and the gravitational potential energy of particles in the atmosphere. If an upwards-directed particle exceeds the escape velocity and does not collide with another particle (or become trapped by the magnetic field of the planet), then it is able to escape. It is possible for particles deep in the atmosphere to attain escape velocity, but lose this energy because of collisions with other particles. Therefore, escape typically occurs in the upper atmosphere, around the location in which the gas density becomes so rarefied that the mean free path of a gas particle is larger than the scale height of the atmosphere, termed the *exobase*.

There are a variety of mechanisms in which particles can gain the required energy to escape from the planet, which can be roughly categorized into thermal escape, non-thermal escape and impact erosion (Gronoff et al., 2020). Thermal escape is when the energy required to escape is provided by the internal energy (i.e. temperature) of the atmospheric gas. When the average thermal energy of a particle in the atmosphere is much less than its gravitational potential energy, only a small fraction of particles exceed the energy required to escape: those in the high velocity tail of the Maxwell-Boltzmann distribution. This is called Jeans escape. When the average thermal energy of a particle nears the gravitational potential energy, the bulk of the gas has the energy to escape. In this case the atmosphere is no longer static, and flows outwards as a collisional fluid, termed hydrodynamic escape. As the bulk atmosphere flows outwards, the condition that escape occurs at the exobase is relaxed; therefore, the mass loss rate of hydrodynamic outflows generally dwarfs those of Jeans escape.

Non-thermal escape occurs when particles attain the energy to escape from chemical or ionic interactions. The most significant non-thermal processes are: photochemical escape, where dissociative reactions impart sufficient energy for a particle to escape; charge exchange, where a high energy magnetospheric ion, which was trapped by the planet's magnetic field, undergoes charge exchange to produce a high energy neutral that can escape; sputtering, where collisions with high energy particles in the stellar wind or radiation belts accelerate particles up to escape velocity, and the polar wind, which is a supersonic outflow of ions from polar ionosphere accelerated by ambipolar electric fields (Gronoff et al., 2020). For planets in the Solar System, Jeans escape or non-thermal processes dominate the present day mass loss (Gronoff et al., 2020), however for close-in exoplanets with extended volatile atmospheres the escape rates for these processes are significantly lower than expected for hydrodynamic escape (Tian et al., 2005). Given the importance of hydrodynamic escape compared to non-thermal processes for close-in exoplanets, I will focus on hydrodynamic escape for the rest of the thesis.

Another possible driver of atmospheric escape is impact erosion, where escape is triggered by collision events. These impacts can vary in scale, from small planetesimals to massive bodies like moons or planets. Escape can occur in two ways: first, at the impact site, expansion plumes can expel the atmosphere locally (e.g., Melosh & Vickery, 1989; Schlichting et al., 2015). Secondly, giant impacters can create a strong shock that propagates through the interior to the atmosphere driving global atmospheric escape (e.g., Schlichting et al., 2015). This mechanism may be important for determining the atmospheric mass fraction of close-in planets and therefore observed demographics (Chance et al., 2022; Izidoro et al., 2022).

1.2.1 Basics of Hydrodynamic Escape

The origin of hydrodynamic escape theory comes from considerations of the dynamics of the solar corona. Eugene Parker (Parker, 1958) showed that the assumption of a hydrostatic solar corona (which was the prevailing model at the time) led to unphysically large gas pressure and densities far from the Sun. His solution was to propose that the corona is expanding transonically into what is known today as the stellar wind. This model explained the observations that comet tails always pointed anti-Sunward (Biermann, 1951, 1952, 1957).

Isothermal Parker Wind

The original and simplest model of a transonic wind formulated by Parker (Parker, 1958) is found by solving the spherically-symmetric, isothermal fluid equations. Mass conservation is given by:

$$\frac{1}{r^2}\frac{\partial}{\partial r}(\rho u r^2) = 0, \tag{1.3}$$

where ρ is the density and u is the velocity of the outflow. This is equivalent to the statement that the mass loss rate is constant:

$$\dot{M} = 4\pi\rho u r^2 = \text{const.} \tag{1.4}$$

Momentum conservation is given by:

$$u\frac{\partial u}{\partial r} + \frac{1}{\rho}\frac{\partial P}{\partial r} + \frac{GM}{r^2} = 0. \tag{1.5}$$

where P is the pressure, M is the mass of the body and G is the gravitational constant. Using the isothermal equation of state, $P = \rho c_s^2$, and substituting in Eq. 1.3, this can be re-arranged to:

$$\frac{1}{u}\frac{\partial u}{\partial r} = \left(\frac{2c_s^2}{r} - \frac{GM}{r^2}\right) \Big/ \left(u^2 - c_s^2\right), \tag{1.6}$$

where:

$$c_s = \sqrt{\frac{k_b T}{\mu m_H}} \tag{1.7}$$

is the isothermal speed of sound, T is the temperature of the gas, μ is the mean molecular weight of the gas and m_H is the mass of a hydrogen atom. The velocity can be solved numerically and there are six different classes of solutions, shown in Figure 1.4.

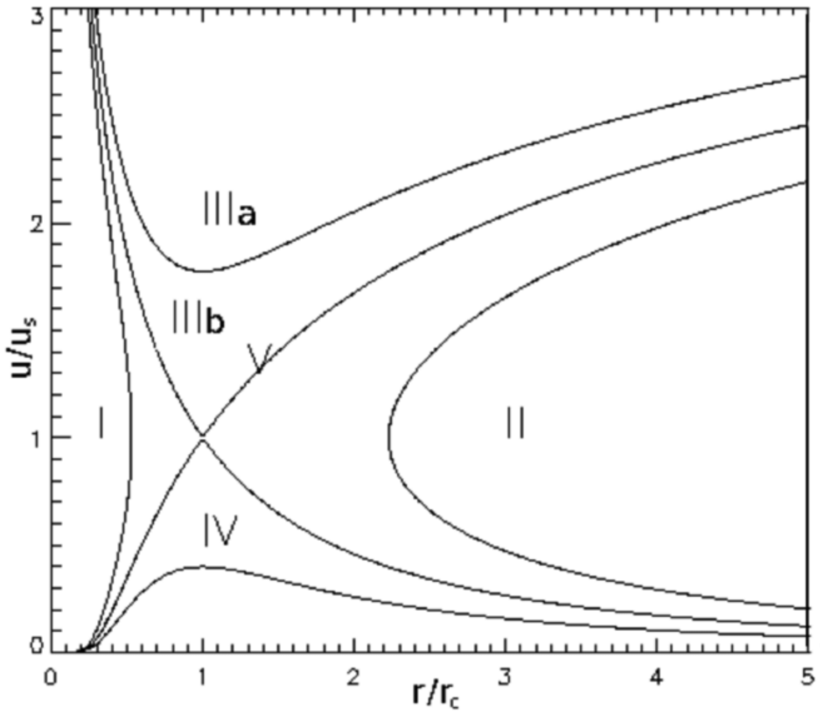

Figure 1.4: Solutions to the spherically symmetric isothermal wind equations. The transonic solution for an outflowing wind is given by V and a representative breeze solution is illustrated by IV. All other solutions are either unphysical or do not apply to a outflowing planetary wind. Figure from (Krista, 2011)

The interiors of stars/planets are observed to be in approximate hydrostatic equilibrium; therefore, at the base of the flow the velocity should be subsonic. As a result, the only plausible solutions are class IV and class V (class I is multi-valued and therefore not physical). These correspond to a subsonic breeze and a transonic wind respectively. The subsonic breeze, like the hydrostatic solution, has a large gas density and pressure far away from the body. This is not physical, unless the pressure is matched at the outer boundary of the breeze. Examples of this are planets immersed in their parent protoplanetary disk (e.g., Rogers et al., 2024a) or confined by particularly strong stellar winds (e.g., McCann et al., 2019). Conversely, for the transonic solution, the pressure vanishes at large distances.

This is valid for the Sun immersed in the low pressure interstellar medium and planets immersed in typical low pressure environments.

Note that the transonic solution must pass through a unique sonic point r_c, with the condition:

$$u(r_c) = c_s \tag{1.8}$$

$$r_c = \frac{GM}{2c_s^2} \tag{1.9}$$

in order for the derivative of the velocity to allow a finite solution. For the solution to be valid, the flow must remain collisional up to the sonic point. Beyond this point, the flow becomes supersonic as it is causally disconnected from the base of the flow. As a result, the mass loss rate at the sonic point specifies the mass loss of the planet.

Energy Equation

In the previous model, the outflow was chosen to be isothermal. In an isothermal outflow, the specific internal energy of the fluid is constant. However, in a realistic outflow, energy is transported through, into, and out of the fluid; therefore, these processes need to be accounted for with the addition of an energy equation. The basis of the energy equation comes from the first law of thermodynamics, which is an expression of energy conservation:

$$dU = dQ - dW \tag{1.10}$$

where dU is the change in internal energy of the gas, dQ is heat transfer into/out of the gas and dW is the work done by the gas. The general inviscid energy equation is:

$$\frac{\partial E}{\partial t} + \boldsymbol{\nabla} \cdot [(E + P)\mathbf{u}] = -\rho \mathbf{u} \cdot \boldsymbol{\nabla}\psi + Q \tag{1.11}$$

where $E = \frac{1}{2}\rho u^2 + \rho e$ is the total energy of the flow, e is the internal energy, ψ is the gravitational potential and Q is the heating/cooling rate per unit volume. The heating/cooling term accounts for how heat is transported throughout the flow. The primary forms of energy transport are through conduction, convection and radiation. In the atmospheres of close-in exoplanets, energy transport is dominated by convection and radiation.

In optically thick mediums, where the mean free path of a photon is much smaller than the length scale of interest, this occurs as a diffusion process. In optically thin mediums, the photons free stream through the medium, and the energy transport occurs at the speed of light. The deep atmosphere of planets, which are optically thick to radiation, are thought to be convectively unstable (Fortney et al., 2007; Rogers et al., 2011; Piso & Youdin, 2014; Lee et al., 2014). In the upper atmosphere, due to external heating, the temperature gradient is reduced such that it becomes convectively stable, and energy transport is dominated by radiation. The boundary between these two regions is called the radiative-convective boundary.

1.2.2 Models of Hydrodynamic Escape

Escape models can broadly be partitioned into two categories based on the energy source driving the escape: photoevaporation, in which the energy comes from stellar X-rays and extreme ultraviolet photons (XUV) or bolometrically driven mass loss, in which the energy comes from the stellar bolometric radiation. As the bolometric luminosity of a star exceeds the XUV luminosity by orders of magnitude, one might naively think that bolometrically driven escape dominates the mass loss of a planet. However, not all the received energy from the star is translated into escape; much of it is re-radiated away. For example, solar EUV and UV radiation absorbed in Earth's thermosphere is primarily conducted downwards and re-radiated away by CO_2, rather than being used to drive escape (e.g., Johnstone et al., 2018). The critical part of modeling escape is figuring out how energy is transported through the atmosphere, and how much of the absorbed energy can be transferred into driving escape.

Photoevaporation

Photoevaporation is hydrodynamic escape driven by the heating of the upper atmosphere by incident stellar XUV radiation. High-energy XUV photons ionize atoms/molecules in the upper atmosphere, producing energetic photoelectrons that heat up the surrounding gas (e.g., Shematovich et al., 2014). One of the first numerical models of photoevaporation was performed by Yelle (2004) to study atmospheric escape of hot Jupiters. This model included a chemical network consisting of hydrogen and helium and energy transport: conduction, radiative cooling, adiabatic cooling. The simulations showed that H_2 was dissociated in the upper atmosphere, and that it is dominated by atomic hydrogen with temperatures on the order of $10,000$ K, since hydrogen atoms are poor at radiating away energy below this temperature. This is because below $\sim 10^4$ K, collisions are not energetic enough to excite the electron transitions which lead to radiative cooling. This is the principle reason why photoevaporation works as a mechanism to drive escape: the absorbed energy cannot be effectively radiated away, and therefore the atmosphere becomes over-pressurized leading to an outflowing wind.

Murray-Clay et al. (2009) investigated escape from hot Jupiters using radiation-hydrodynamics simulations and found that the efficiency of escape decreases for higher EUV fluxes. The explanation is that the higher incident flux leads to a hotter outflow which has significantly increased radiative losses due to enhanced Lyman-α cooling. Typically the efficiency of the outflow is parametrized in terms of the energy-limited mass loss rate:

$$\dot{M}_p = \eta \frac{R_p^3 F_{\mathrm{XUV}}}{G M_p}, \tag{1.12}$$

where R_p is the radius of the planet, F_{XUV} is the incident XUV flux, M_p is the mass of the planet and η a parameter denoting the efficiency of the escape process. Many numerical studies of radiation-hydrodynamic escape have focused on calculating the efficiency as a function of gravity and XUV flux (e.g., Owen & Jackson, 2012; Owen & Alvarez, 2016; Kubyshkina et al., 2018; Caldiroli et al., 2022). These works illustrated that the efficiency typically decreases with increasing gravitational potential due to the increased radiative cooling from hotter flows with longer flow timescales.

These works considered pure hydrogen outflows; however, the metallicity of the upper atmosphere of planets undergoing escape is expected to be a least solar, in the case of hot Jupiters, and may be high metallicity in the case of sub-Neptunes. The effect of metals is two-fold: firstly, they increase the mean molecular weight of the outflow, which leads to lower outflow velocities. More importantly, metals are better radiative coolants than hydrogen or helium (Spitzer, 1978), therefore they reduce the energy available to drive escape.

Although the assumption of spherical symmetry is convenient so that simulations may be done in 1D, it is not an accurate representation of planet undergoing escape. Anisotropic irradiation means an unequal heat distribution around the planet. This is maximized for close-in planets, that are thought to be tidally locked (Ferraz-Mello, 2013b), and therefore have a permanent day and night side. Additionally, beyond the planet's Roche lobe, the effects of stellar gravity, radiation pressure, and interactions with the stellar wind on the outflow are inherently asymmetric. As a result, multi-dimensional models are essential for accurately representing the outflow dynamics. Self-consistent multi-dimensional simulations showed that the resulting outflow is extremely asymmetric (e.g., Stone & Proga, 2009; Owen & Adams, 2014; Tripathi et al., 2015; Khodachenko et al., 2019; McCann et al., 2019; Carolan et al., 2021a; Hazra et al., 2022). Despite this, the average mass loss rates found are similar to those found from one-dimensional calculations (McCann et al., 2019), therefore the motivation behind the many of the advanced three dimensional simulations is to compare to observations of atmospheric escape, rather than calculating mass loss rates. I will discuss this further in Section 1.4.

Bolometrically-driven Mass Loss

In bolometrically-driven escape (also known as core-powered mass loss), the outflow is driven by the planet's cooling luminosity and stellar bolometric luminosity (Ginzburg et al., 2018; Gupta & Schlichting, 2019). For this mechanism to be effective, the planet typically needs to have low gravity and have a high effective temperature. This is generally true for young planets, whose atmosphere is still hot from formation. To sustain mass loss as the planet radiates away energy, the atmosphere needs to remain puffy and hot by being resupplied with heat by the thermally coupled silicate core (Misener & Schlichting, 2021). The mass loss rate of the outflow is sensitive to the structure of the planet (e.g. atmospheric mass fraction, radiative-convective boundary position) and the opacity structure in the atmosphere, as these set the density and the temperature of the wind (Misener et al., 2024).

Magnetic Fields

The works discussed so far have investigated hydrodynamic outflows from non-magnetized planets, however real outflows may be altered by any magnetic field of a planet. By nature, photoevaporative outflows are highly ionized and therefore will be influenced by a magnetic field. Analytical work by Adams (2011) and Trammell et al. (2011) showed that photoevaporative outflows from hot Jupiters are well approximated by ideal MHD, and consequently that the magnetic field is frozen into the plasma. The degree to which the planetary magnetic field controls the outflow is determined by the ratio of the magnetic pressure to the thermal/ram pressure of the outflow. If the magnetic pressure dominates near the planetary surface, then the gas is constrained to the topology imposed by the planet's magnetic field. For this "magnetically controlled" case, analytical and numerical studies showed that the planetary atmosphere consists of two distinct regions (e.g., Trammell et al., 2011; Adams, 2011; Trammell et al., 2014; Owen & Adams, 2014; Khodachenko et al., 2015; Matsakos et al., 2015; Arakcheev et al., 2017). In a region near the equator, the magnetic field lines are closed and the gas is trapped in a "dead zone". At higher latitudes, the pressure of the outflow is able to open up the magnetic field lines and drive a transonic wind. Alternatively, if the thermal/ram pressure of the gas dominates everywhere, the outflow opens all the magnetic field lines (dragging the magnetic field with the flow). In this "hydrodynamics case", the outflow represents those seen in purely hydrodynamic simulations.

In magnetically controlled outflows, only a fraction of the planetary surface supports open field lines where the gas can escape, therefore the mass loss rate is suppressed compared to hydrodynamic outflows. 2D MHD simulations have suggested that surface magnetic field strengths as low as $\sim 0.3-3$ Gauss can suppress the mass loss rate of hot Jupiters by an order of magnitude (Trammell et al., 2014; Owen & Adams, 2014; Khodachenko et al., 2015). The critical magnetic field strengths required to suppress mass loss rates are smaller or comparable to many of the planetary magnetic field strengths in our Solar System (e.g. Jupiter's dipole moment is ~4 Gauss, Stevenson 2003; Connerney et al. 2022). Therefore it is important to consider the effects of magnetic fields on escape for exoplanets and understand how to determine their impact observationally. 3D MHD simulations that include the stellar wind also found the planetary mass loss rate decreases with planetary magnetic field strength (Khodachenko et al., 2021). However, similar simulations run by Carolan et al. (2021b) show the opposite dependence, and the differences are yet to be fully understood.

1.3 Atmospheric Escape from Exoplanets: Evolution and Demographics

Planets accrete their primordial hydrogen/helium atmospheres from the protoplanetary disk. The thermal energy gained through the formation process means that planets start hot and luminous with extended atmospheres. As the planet cools, the atmosphere contracts becoming denser and smaller. Simultaneously the atmosphere will evolve as a result of mass loss due to hydrodynamic escape or impacts and interactions with a surface magma ocean (e.g., Kite & Barnett, 2020; Kite & Schaefer, 2021; Rogers et al., 2024b).

Mass loss is most pronounced during the early stages of a planet's evolution. Firstly, at this time, the planet's atmosphere is hot and extended, making it easier to remove gas since less energy is required to overcome the gravitational binding. As the planet cools over time, its atmosphere contracts and sits deeper within the gravitational potential well, making mass loss less efficient. Secondly, the large size of the early atmosphere means that the total area to absorb X-ray/EUV radiation from the star is increased. Thirdly, young stars are more active than older stars and emit a higher fraction of their total luminosity in X-ray and EUV radiation (e.g., Jackson et al., 2012; King & Wheatley, 2021). These latter two effects mean that the total amount of high-energy radiation received by the planet is greatest early in the planets lifetime.

The evolution giant planets and low mass planets due to thermal evolution and mass loss follow different trajectories, therefore, need to be treated separately. This is primarily due to the different mass-radius relations for small and giant planets (e.g., Chen & Kipping, 2017; Bashi et al., 2017). For gas-rich small planets, structure models indicate that the radius of the planet decreases as the atmospheric mass decreases (for constant core mass Lopez & Fortney 2013). In contrast, for giant planets, the radius weakly decreases as a function of planetary mass, with an empirically observed relation of $R \sim M^{-0.04}$ (Chen & Kipping, 2017). The inverse relationship between radius and mass arises from the fact that these objects are partially supported by degenerate matter (Chabrier & Baraffe, 2000).

Giant Planets

Evolutionary calculations of giant planets indicate that they are generally stable against photoevaporative mass loss, typically losing no more than a few percent of their atmospheric mass (Hubbard et al., 2007; Jin et al., 2014; Owen & Wu, 2013). However, if the planet migrates close enough to their host star to experience Roche lobe overflow, mass loss rates may be orders of magnitude higher than those caused by photoevaporation (Valsecchi et al., 2014, 2015), which can lead to runaway mass loss.

1.3.1 Low mass planets

Evolutionary models suggest that highly irradiated low-mass planets with substantial H/He atmospheres may undergo runaway atmospheric mass loss transiting from a gas-rich planet to a rocky planet (Valencia et al., 2010; Lopez & Fortney, 2013; Owen & Wu, 2013). The majority of the observed planets are billions of years old (Melo et al., 2006; Silva Aguirre et al., 2015), therefore already sculpted by atmospheric escape. The pertinent question is therefore: does the current observed exoplanet population reflect an initial population of planets that have been shaped by atmospheric escape processes?

Two prominent features in the observed exoplanet population are the radius valley and the hot-Neptune desert. The Neptune desert is the dearth of planets of masses around 20-200 Earth masses out to orbital periods of 3 days (Szabó & Kiss, 2011; Lundkvist et al., 2016). The lower boundary of the hot-Neptune desert is well explained by atmospheric escape from low-mass planets with large hydrogen/helium atmospheres (e.g., Owen & Lai, 2018). In contrast, the upper boundary cannot be reproduced by escape models. Supporting this, direct observations of helium escape from planets near this boundary show mass loss rates too low to be evolutionarily significant (Vissapragada et al., 2022). It is instead suggested that this upper boundary may be shaped by the distribution of giant planets undergoing high-eccentricity migration (Matsakos & Königl, 2016; Owen & Lai, 2018).

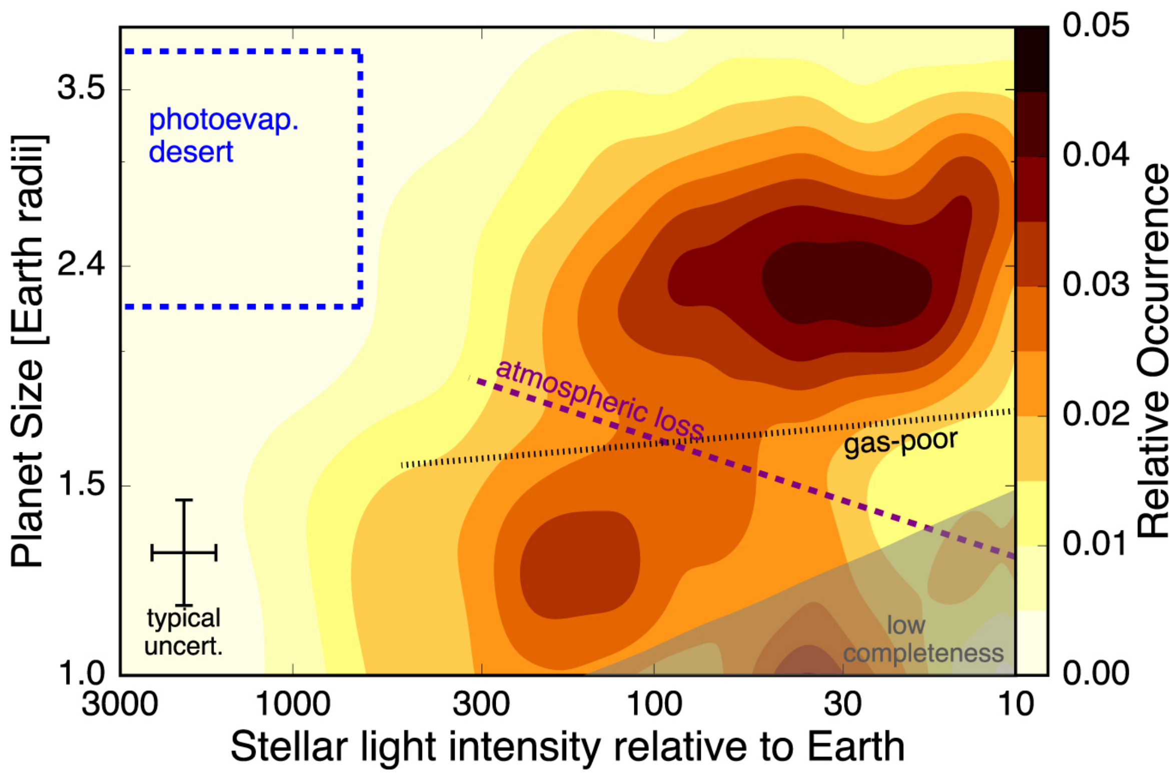

Figure 1.5: Occurrence rates of small planets calculated from the California Kepler Survey sample (Petigura et al., 2017). The sculpting of this bimodal distribution is attributed to atmospheric mass loss. Figure taken from Fulton et al. (2017).

The radius distribution of small, close-in exoplanets is bimodal distribution, with peaks at $\sim 1.3R_\oplus$ and $\sim 2.4R_\oplus$ (Fulton et al., 2017; Van Eylen et al., 2018), shown in Figure 1.5. In-between these populations, a dearth of planets was observed with a minimum $\sim 1.8R_\oplus$. In the period-radius plane, the location of the minimum decreased as a function of period. This is naturally explained by atmospheric escape theory (Lopez & Fortney, 2013; Owen & Wu, 2013). These models show that planets above the gap have extended H/He envelopes, but below the gap they are completely stripped. Below a $\sim 1\%$ atmospheric mass fraction, the mass loss timescale keeps decreasing; therefore, planets could not host arbitrarily small hydrogen/helium envelopes because at some point they would undergo runaway mass loss. The gap is formed by the difference in radii between planets with marginally stable atmospheres and those that are stripped to bare cores.

One key insight is that the location of the radius gap is influenced by the density of the planetary core. Core density affects the mass loss rate, which in turn determines the maximum core mass that can be stripped and the minimum atmospheric mass that remains stable. As a result, evolutionary escape models can use the radius gap to constrain the core composition of planets (Owen & Wu, 2017; Jin

& Mordasini, 2018; Rogers & Owen, 2021). However, different escape mechanisms—such as core-powered mass loss, photoevaporation, and magnetically controlled escape—predict varying outcomes for planetary properties (Gupta & Schlichting, 2019; Owen & Adams, 2019). This underscores the need for accurate escape models.

1.4 Atmospheric Escape from Exoplanets: Observations

Direct observations of ongoing atmospheric escape provide an avenue to test escape models. So far this has been done using transmission spectroscopy. To confirm that escape is occurring, planetary gas needs to be observed outside the Roche lobe of the planet, the teardrop-shaped region in which the gas is gravitationally bound to the planet. To show this, either the transit depth needs to be greater than the Roche lobe radius of the planet or the transit duration must extend beyond that which would come from gas inside the Roche lobe. The volume of the Roche lobe is approximately the same as that as a sphere with radius R_H, termed the Hill sphere radius:

$$R_H \approx a\sqrt{\frac{M_p}{3M_*}}, \tag{1.13}$$

where a is the semi-major axis of the planet, M_p is the mass of the planet and M_* is the mass of the star.

Hydrodynamic outflows are rarefied and typically atomic; therefore, they can only be observed in strong spectral lines. Since these outflows are primarily composed of hydrogen and helium, the principal tracers used to detect atmospheric escape are lines of hydrogen and helium: Lyman-α, the Balmer series and He 10830 Å line. Observing escape in metal lines is also possible; however, as the metal fraction in the upper atmosphere of planets with hydrogen/helium envelopes is low, these signals tend to be weak. Currently, there have been more than 28 detections of atmospheric escape from transiting planets (Dos Santos, 2023). In this section, I discuss these tracers in detail.

1.4.1 Lyman-α

Lyman-α was the first spectral line used to detect ongoing atmospheric escape from the transiting hot Jupiter HD209458 b (Vidal-Madjar et al., 2003). It was found to have an absorption depth of $\sim$ 15%. In comparison, the maximum transit depth from gas inside the Hill sphere is $\sim$ 13%. Further detections of escape from HD189733 b with a transit depth of 5% (Lecavelier des Etangs et al., 2004), GJ436 b with a transit depth of 56% (Kulow et al., 2014; Ehrenreich et al., 2015; Lavie et al., 2017) and GJ4370 b with an absorption depth of of 35% (Bourrier et al., 2018) solidified its usefulness as a tracer of atmospheric escape.

However, interpreting Lyman-α transit observations presents significant challenges. Lyman-α observations are contaminated by geocoronal emission, caused by the scattering of solar Lyman-α radiation by hydrogen in Earth's exosphere. Fortunately, this effect can be corrected with reasonable accuracy (e.g., Landsman & Simon, 1993; Vidal-Madjar et al., 2003). A more significant challenge arises from the strong absorption of stellar Lyman-α emission by neutral hydrogen in the local interstellar medium (ISM). As a result: 1) Lyman-α observations are only feasible for nearby stars, where neutral hydrogen column densities in the ISM are relatively low, and 2) even for close stars, the core of the Lyman-α line is often heavily extinguished (Landsman & Simon, 1993). The strength and wavelength range of the obscuration depends on the properties of the interstellar medium in the line of sight of the star and the peculiar velocity of star, but generally the stellar Lyman-α line is completely extinguished between $\sim$ [-50, 50] km s^{-1} (in the rest frame of the star). Consequently, the outflow properties must be inferred from absorption in the Lyman-α line wings.

As photoevaporation and bolometrically-driven mass loss models predict outflow velocities $\ll$ 50 km s^{-1}, it is puzzling that such large escape signatures are observed. Closer inspection of the spectrum shows that this absorption is typically in the blue wing of the line, and may continue for hours after the optical transit (see Figure 1.6). For realistic mass loss rates, the density of the neutral hydrogen atoms is not large enough for Lorentzian line broadening to be the sole source of observed high-velocity absorption (Murray-Clay et al., 2009). To reproduce the observed signatures, there must be some additional physics that one dimensional escape models are missing, which can generate a population of high-velocity hydrogen atoms.

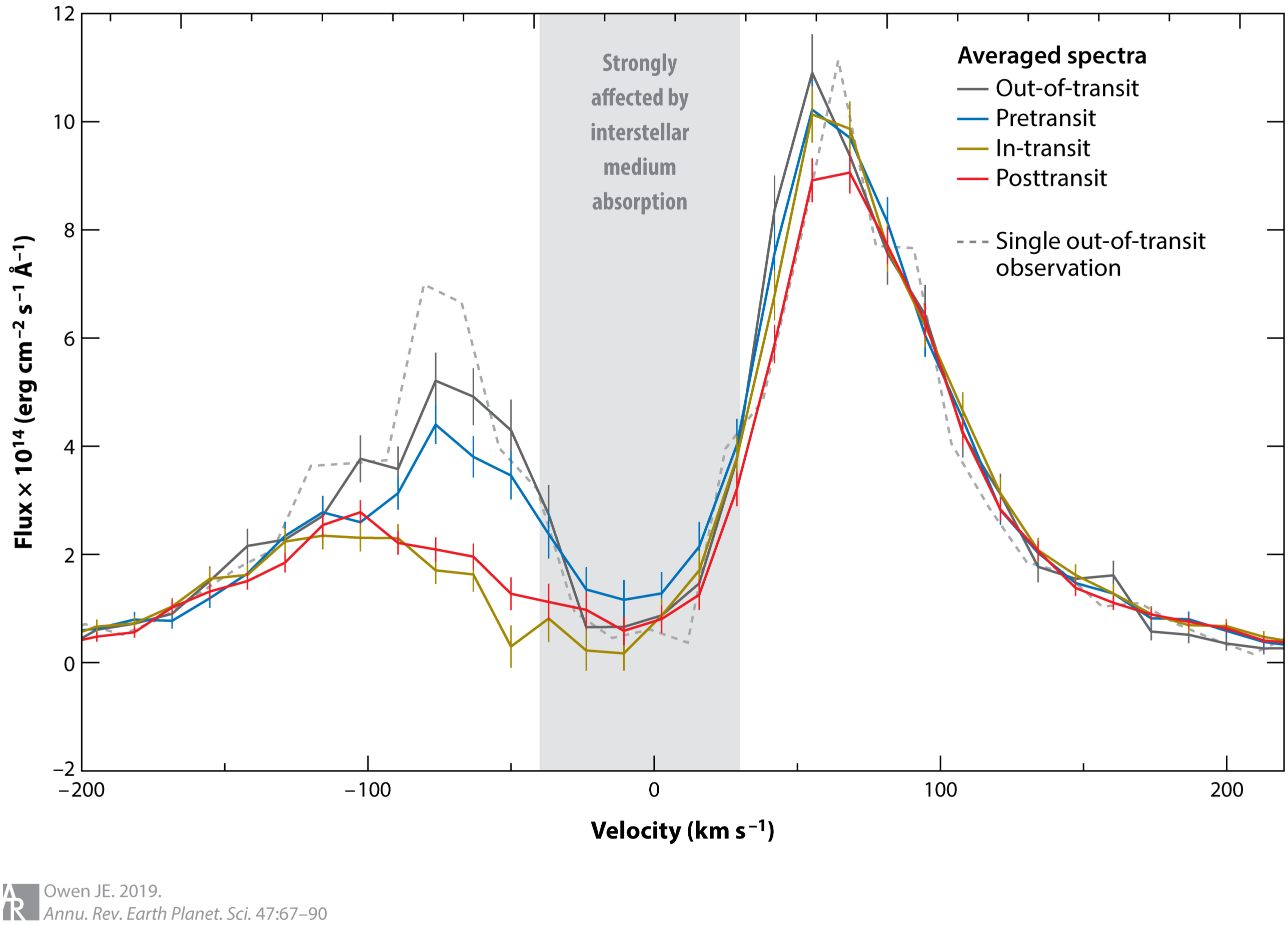

Figure 1.6: The observed Lyman-α spectrum of the star GJ436 at different times during the orbit of the close-in planet GJ436 b. The black, blue, yellow and red solid lines show the observed out-of-transit, pre-transit, in-transit, post-transit spectrum respectively, averaged over three transits. The shaded grey shows the region where Lyman-α is extinguished by absorption in interstellar medium. The large reduction in Lyman-α in the blue-wing during and post-transit indicates that GJ 436 b has an escaping hydrogen atmosphere that absorbs Lyman-α radiation emitted by the star. The reduction post-transit indicates that the planetary outflow is shaped into a cometary tail, that extends far beyond the planet. Figure taken from (Owen, 2019) with permission.

The solution to this problem is that high-velocity hydrogen atoms are generated via the interaction between the stellar wind and the escaping gas. This interpretation is supported by the extended duration and depth of the transit (for example, the transit of GJ436 b lasts for over 5 hours). At these distances, the planetary gas is far outside the Roche lobe of the planet where it is expected to be shaped by the space environment. The three primary mechanisms that have been proposed to generate high-velocity hydrogen atoms are: acceleration of the planetary outflow by the impact of the stellar wind (e.g., Carroll-Nellenback et al., 2016; McCann et al., 2019; Debrecht et al., 2020; Carolan et al., 2021a; Villarreal D'Angelo et al., 2021; Hazra et al., 2022), acceleration of the planetary outflow by radiation pressure (e.g., Bourrier et al., 2015; Khodachenko et al., 2019; Debrecht et al., 2020) or charge exchange between stellar wind protons and planetary neutral hydrogen (e.g., Holmström et al., 2008; Tremblin & Chiang, 2012; Bourrier et al., 2016; Khodachenko et al., 2019). In the former two, the majority of Lyman-α absorption is from the bulk planetary outflow, whilst in the latter, the absorption is from a minor population of high-velocity neutral hydrogen atoms, which are produced at the interface between the planetary and stellar wind.

To properly represent the dynamics of the planetary gas outside the Roche lobe of the planet, where it is shaped by stellar gravity, the stellar wind and radiation pressure, requires three-dimensional modelling. This modelling has been done either using a particle-based approach (e.g., Holmström et al., 2008; Kislyakova et al., 2014; Bourrier et al., 2015, 2016) or a hydrodynamic approach (e.g., Tremblin & Chiang, 2012; Carroll-Nellenback et al., 2016; McCann et al., 2019; Khodachenko et al., 2019; Villarreal D'Angelo et al., 2021; Hazra et al., 2022; Carolan et al., 2021a). The particle-based approach uses Monte-Carlo simulations of meta-particles (representing a large number of real particles with similar position and velocities) to calculate the trajectories of atoms/ions in the planetary wind. Although, a Monte-Carlo approach is in principle valid for flows of any Knudsen number (which specifies the collisionality of the flow), the computational cost is such that often other assumptions are needed to make simulation tractable. For example, in Bourrier et al. (2015, 2016) they ignore collisions between hydrogen atoms and other atoms/ions. These methods become more computationally expensive as the density of flow increases so they are typically used for fluids that are not collisional. In contrast, a hydrodynamic approach is valid for collisional fluids.

Figure 1.7 shows the density structure for a self-consistently launched hydrodynamic, escaping planetary outflow for different stellar wind strengths. In the weak stellar wind regime, the outflow forms a torus around the star. In contrast, under strong stellar winds, the outflow is funnelled into a comet-like tail, exhibiting key features consistent with Lyman-α transit observations—most notably, the pronounced blue-shifted absorption visible both during and after the optical transit (McCann et al., 2019; Villarreal D'Angelo et al., 2021; Carolan et al., 2021a; Hazra et al., 2022). Simulations, which investigate the role of radiation pressure (in Lyman-α), similarly find that the material is funnelled into a cometary tail. However, for realistic stellar Lyman-α fluxes, the velocities reached by the planetary material in these models are typically insufficient to explain observations (e.g., Bourrier et al., 2015; Debrecht et al., 2020).

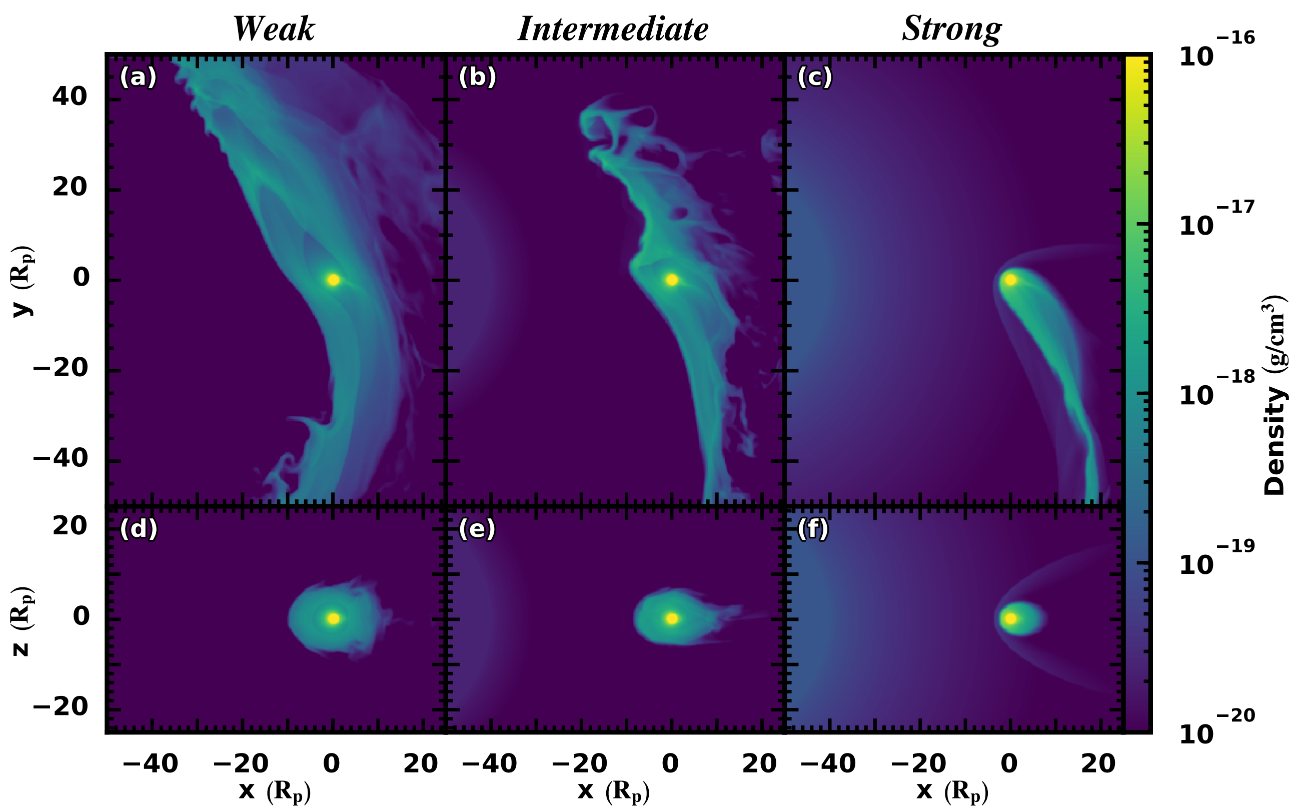

Figure 1.7: 3D radiation-hydrodynamics simulations of atmospheric escape performed by McCann et al. (2019). The three panels show the shape of outflow when impacted by different strength stellar winds. In each case, the star is directed in the negative x-direction. In the strong stellar wind case, the outflow is pushed outwards and shaped into a cometary tail, exhibiting key features consistent with Lyman-α transit observations-most notably, the pronounced blue-shifted absorption visible both during and post the optical transit. Figure taken from McCann et al. (2019).

Simulations that include the production of energetic neutral atoms (ENAs) by charge exchange between stellar wind protons and planetary hydrogen atoms also are able to reproduce the key features of Lyman-α transits (e.g., Khodachenko et al., 2019). Charge exchange, which occurs in a mixing layer at the interface between the planetary and stellar wind, is not dynamically important in shaping the planetary outflow, so the global structure of the outflow is reminiscent of simulations that do not include this process. In these simulations, Lyman-α absorption is from a combination of ENAs and planetary neutrals.

These simulations have been instrumental in identifying the dominant physical processes shaping planetary outflows and determining the characteristics of Lyman-α transits. However, multi-dimensional (radiation)-hydrodynamics simulations are computationally expensive, therefore large parameter studies are infeasible. This is particularly problematic as the observed transit depends on uncertain stellar/planetary parameters (e.g. stellar wind mass loss rate, stellar wind velocity, stellar XUV radiation). This means that there has yet to be a systematic study of the properties of Lyman-α transits over the large parameter space of possible systems, which makes it challenging to interpret observations.

A Toy Model For Lyman-α transits

To address the aforementioned problems, Owen et al. (2023) developed a simplified framework to understand Lyman-α transit observations. Their study specifically examined scenarios with strong stellar winds, where the outflowing gas is funneled into a comet-like tail trailing the planet (see Figure 1.7). This is a configuration necessary to produce the pronounced blue-shifted signals observed (> 50 km s^{-1}). They modelled the cometary tail as an elliptic cylinder, positioned on the semi-major axis of the planet with constant height and depth, shown in Figure 1.8.

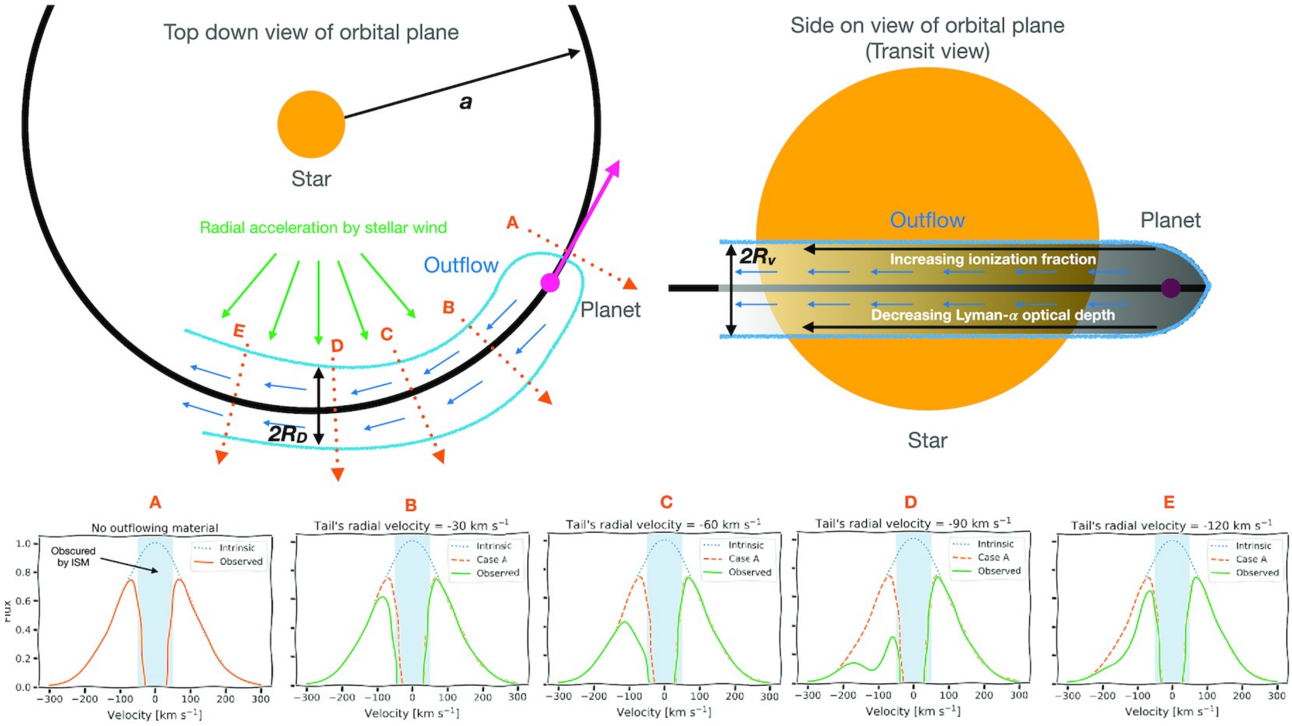

Figure 1.8: The top panel shows a schematic diagram of the outflowing gas shaped into a cometary tail, as modelled by Owen et al. (2023). The evolution of the Lyman-α spectrum for an observable transit is shown in the bottom panel. The tail is progressively accelerated outwards by the stellar wind such that the hydrogen gas is able to absorb in the blue-wing. Simultaneously, the gas gets more ionized, eventually becoming optically thin such that this absorption falls off. Figure taken from Owen et al. (2023).

The height and depth of this cylinder are estimated by calculating how far a gas particle travels vertically under the confining influence of stellar gravity and horizontally before being deflected by the coriolis force. They assume that the radial and aziumuthal velocity of the gas are decoupled such that the gas travels down the tail at the velocity that the wind is launched from the Hill sphere of the planet. Two processes affect the properties of the gas as it travels down the tail. Firstly, the gas is radially accelerated by the stellar wind. Simultaneously, the hydrogen is progressively ionized by stellar EUV radiation. The former process increases the bulk radial velocity of the gas, so that the Lyman-α absorption is more observable, whilst the latter reduces the density of neutral hydrogen, decreasing the Lyman-α optical depth. For a Lyman-α transit to be observable, the tail needs to remain optically thick to Lyman-α photons in the time it takes for the tail to be accelerated to observable velocities > 50 km s^{-1}.

To understand this concretely, following Owen et al. (2023), I will derive an expression for the Lyman-α optical depth of the gas as a function of position in the tail. In the optically thin limit, the evolution of ionized fraction of hydrogen is given by:

$$\frac{DX}{Dt} = (1 - X)\Gamma - nX^2\alpha_A \tag{1.14}$$

where $X = 1 - \mathcal{N}$ is the ionization fraction, n is the number density of hydrogen species, Γ is the optically thin photoionization rate and α_A is the Case A recombination coefficient. The gas injected into the tail will often be far from photoionzation-recombination equilibrium. In this case, it is a good approximation to drop the recombination term in Equation 1.14. Therefore, the steady-state neutral fraction of hydrogen is:

$$u\frac{\partial \mathcal{N}}{\partial \ell} = -\mathcal{N}\Gamma \tag{1.15}$$

where ℓ is the distance the gas has traveled down the tail and u is the azimuthal velocity of the gas. This can be solved to give the neutral fraction in the tail:

$$\mathcal{N} = \mathcal{N}_0 \exp\left(-\frac{\Gamma}{u}\ell\right) \tag{1.16}$$

where $\mathcal{N}_0$ is the neutral fraction of the gas injected into the tail. The Lyman-α optical depth is then:

$$\tau_\alpha = \frac{2\sigma_{Ly\alpha}\dot{M}_p\mathcal{N}_0}{\pi H \mu u}\exp\left(-\frac{\Gamma}{u}l\right) \tag{1.17}$$

where $\dot{M}_p$ is the mass loss rate of the planet, H is the height of the tail, and $\sigma_{Ly\alpha}$ is the Lyman-α cross section. The length along the tail at which the gas becomes optically thin (i.e. $\tau_\alpha \sim 1$) is:

$$\ell_{\tau_\alpha=1} = \frac{u}{\Gamma}\log\left(\frac{2\sigma_{Ly\alpha}\dot{M}\mathcal{N}_0}{\pi H \mu u}\right) = \ell_\Gamma \log \mathcal{T}_p \tag{1.18}$$

where ℓ_Γ is the mean free path of a neutral hydrogen atom before it is photoionized. This equation reveals the curious nature of Lyman-α transits. The Lyman-α optical depth is highly sensitive to the incident EUV flux due to its exponential dependence on the number of neutral hydrogen atoms. In contrast, the optical depth only has a linear dependence on the planet's mass loss rate, which itself is linearly dependent on EUV flux under the assumption of energy-limited mass loss. Consequently, weaker EUV irradiation, which drives lower mass-loss rates, actually leads to longer and deeper transits. Because of the exponential sensitivity to photoionization rate and velocity, they argued that Lyman-α observations are not ideal for precisely constraining mass loss rates.

Of course, ionization is not the only factor at play; the impact of stellar wind is important as it must accelerate the escaping material to observable velocities. Figure 1.9 illustrates how the interplay of these two effects controls the observability of the transit. Essentially, the stellar wind must accelerate the tail to observable velocities > 50 km s^{-1} before it is too highly ionized.

Although this model gives useful insight into how to interpret Lyman-α transits, it simplified the problem to the extent that it cannot be used to fit observations. One problem is that they assumed that the tail remains on the same orbital separation of the planet, which is not the case for very close-in planets such as GJ 436 b (e.g., Khodachenko et al., 2019). Furthermore, they assume that the density of the gas in the tail is constant; however, by conservation of mass, the density should decrease as the gas is accelerated. Finally, the geometry of the tail (i.e. the vertical and horizontal extent of the gas) was calculated by ignoring the stellar wind, which could compress the tail. In Chapter 2, I will develop a model of the tail that fixes these problems so that it can be used to match Lyman-α transit

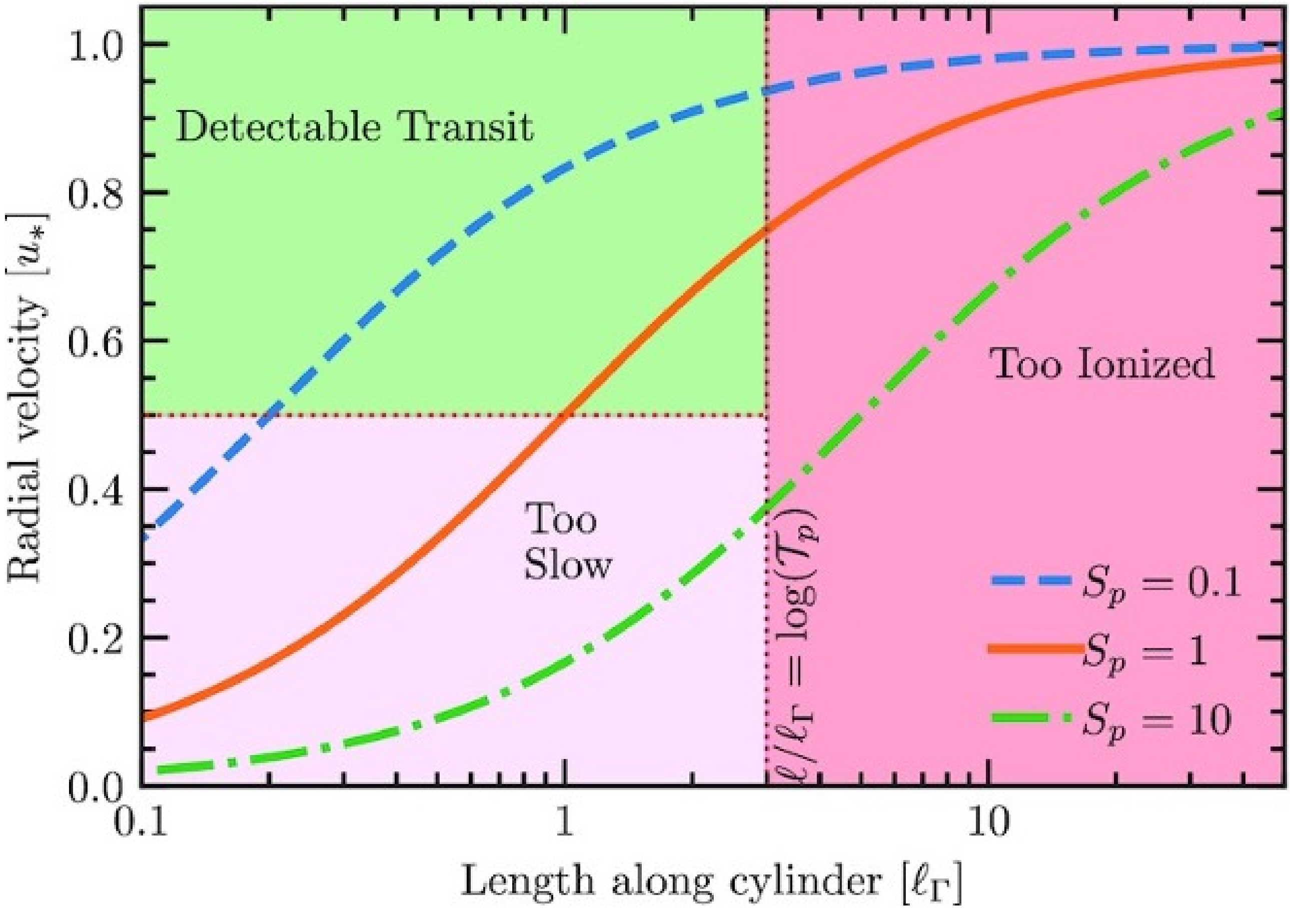

Figure 1.9: A graphical representation of the observability of the outflow in Lyman-α in different parts of the radial velocity-ionization fraction parameter space. The lines show example tracks of the tail's radial velocity, in units of stellar wind velocity, as a function of length along the tail, in units of "ionization length" (see Equation 1.18). The value of S_p encodes the inertia of the tail. The green box shows the region in which the tail is accelerated to detectable velocities before it is so ionized that it becomes transparent to Lyman-α. Figure taken from Owen et al. (2023).

observations.

1.4.2 Helium 10830 Å

Similarly to hydrogen, helium is expected to be abundant in planetary outflows, therefore, a potential tracer of atmospheric escape. The ground-state transitions of He I are in the EUV and therefore inaccessible. However, the structure of neutral helium is such that it possesses a low-energy metastable state (see Figure 1.10). The electrons in the helium atom can either be in triplet configuration (spin = 1) or a singlet configuration (spin = 0). Radiative transitions between the lowest triplet level (2^3S) and the singlet ground state (1^1S) are strongly suppressed and can only occur through a forbidden line photon at a rate of 0.45 hr^{-1} (Drake, 1971). At the low densities collisions with electrons depopulating the triplet state are rare so that there can be a significant population of helium atoms in the 2^3S state. Oklopčić & Hirata (2018) proposed that outflows can be probed by the absorption of photons at 10830 Å, pertaining to the $2^3\mathrm{S} \rightarrow 2^3\mathrm{P}$ transition.

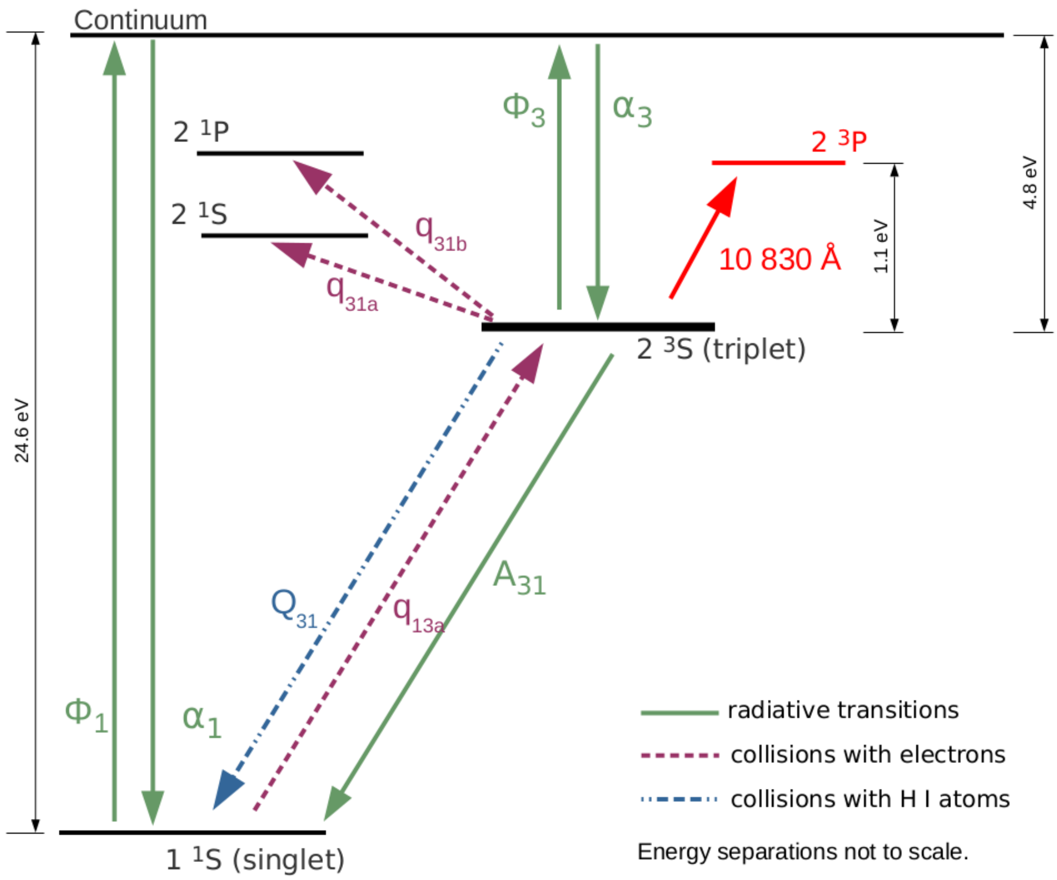

Figure 1.10: The atomic structure of a helium atom, indicating the important radiative and collisional transitions for setting the population of atoms in the metastable, triplet 2^3S state. The transition shown in red is the 10830 Å line used to observe escaping helium. Figure taken from Oklopčić & Hirata (2018).

The first detection of an escaping atmosphere using the 10830 Å line was made by Spake et al. (2018) for WASP-107 b using Wide Field Camera 3 (WFC3) on board the Hubble Space Telescope (HST). It was soon realized that one of the major benefits of the 10830 Å line is that it can be detected from the ground due to its location in the near infrared. Therefore spectroscopic observations can be done at high resolution (e.g., $R \sim 25,000$ for NIRSPEC on Keck II and $\sim$ 100,000 for ANDES on the upcoming Extremely Large Telescope). The first resolved spectroscopic detection of helium escape was made by Allart et al. (2018) for HAT-P-11 b, finding a maximum excess absorption of $\sim$ 1.2%

(see Figure 1.11). High-resolution observations provide a sensitive probe of the velocity structure of the outflow. Combined with the fact that the helium line often forms close to the planet (Linssen & Oklopčić, 2023), this means that observations are sensitive to the kinematics of the outflow right at its launch region.

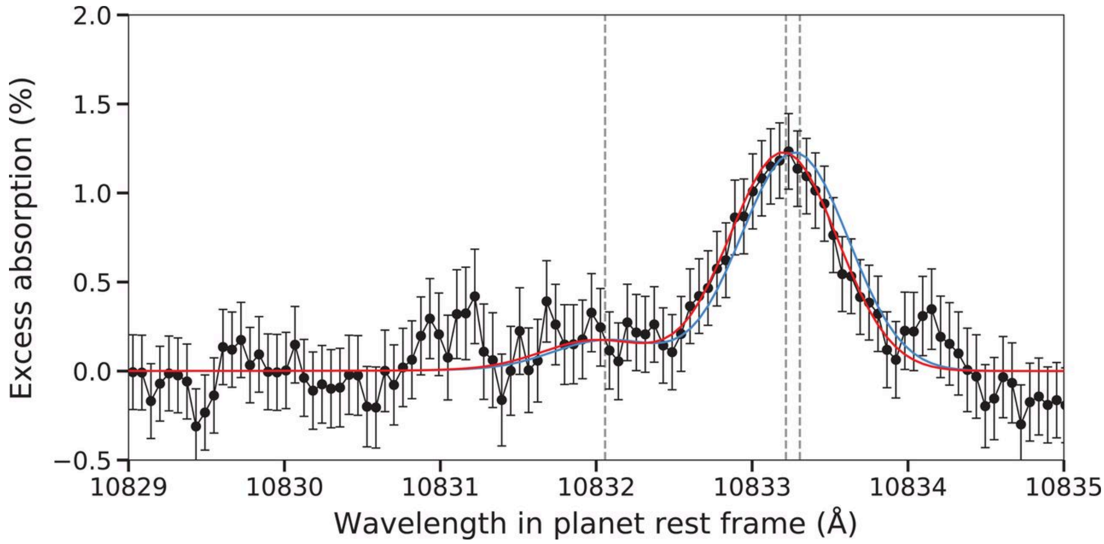

Figure 1.11: HAT-P-11 b's transmission spectra located around 10830 Å . The vertical dashed line show the wavelengths of the three transitions of the helium triplet. Figure from Allart et al. (2018).

An exception to this is for particularly strong outflows (e.g., Spake et al., 2022; Zhang et al., 2023a; Gully-Santiago et al., 2023), where the measured absorption extends far past the Roche lobe of the planet and therefore sculpting of the outflow by stellar gravity and the stellar wind is important. In these cases, three-dimensional simulations are required to model observations (e.g., MacLeod & Oklopčić, 2022).

The population of helium atoms in the metastable state is very sensitive to the UV spectrum of the star (Figure 1.12, Oklopčić 2019), which is generally poorly constrained. Only a subset of stars (primarily K-stars) produce a sufficient population of planetary metastable helium atoms to produce an observable transit (e.g., Orell-Miquel et al., 2024). Additionally, the overall H/He ratio of the escaping gas is uncertain. The H/He ratio in the atmospheres of close-in gas-rich planets is usually assumed to be solar; however, this is untested. Furthermore, mass fractionation can change the H/He ratio of the outflow (Malsky & Rogers, 2020; Xing et al., 2023). Consequently, translating helium escape rates to a total mass loss rate is uncertain.

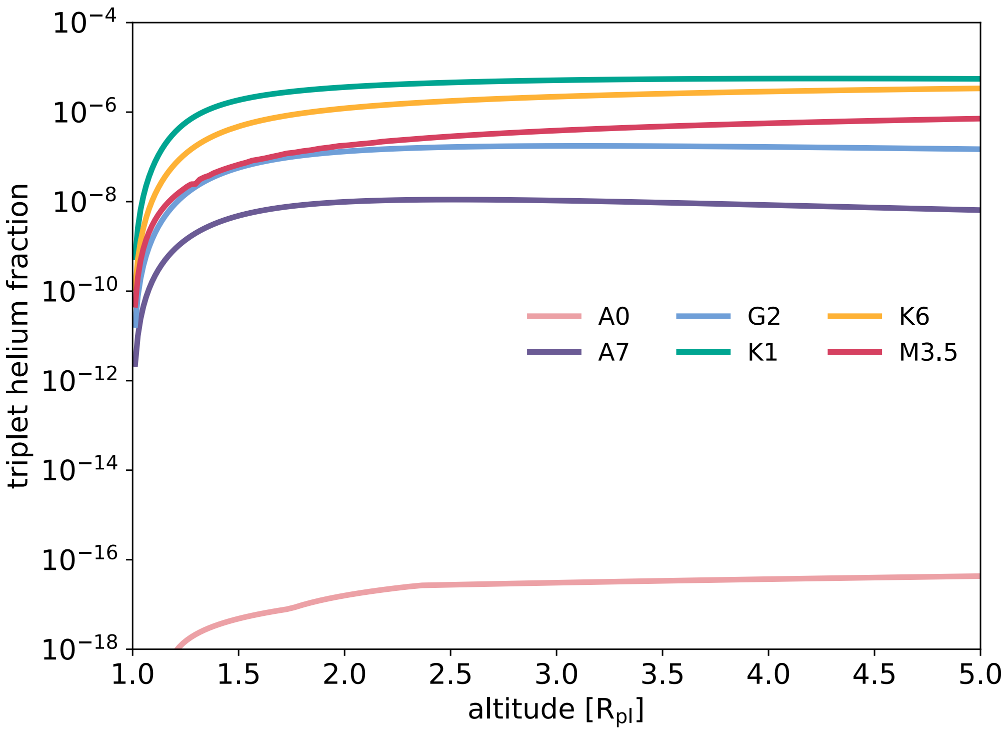

Figure 1.12: The fraction of helium atoms in the triplet state within a planetary wind is shown as a function of altitude. The different lines correspond to planets orbiting stars of various spectral types, demonstrating that K-type stars are the most favorable targets for observing helium escape. Figure taken from Oklopčić (2019).

1.4.3 Balmer and Metal Lines

Another window in which to view hydrogen escape is through the Balmer series (Hα, Hβ, etc.). These are at optical wavelengths, therefore can be observed from the ground at high resolution. Additionally, these lines are not affected by interstellar medium absorption. The disadvantage of Balmer line transits is that there is not expected to be many hydrogen atoms in the $n = 2$ state. Therefore, this has only been observed from highly irradiated hot Jupiters, with extremely high mass loss rates (e.g., Jensen et al., 2012; Yan & Henning, 2018). The ratio of hydrogen in the ground state to the $n = 2$ state is uncertain because the hydrogen level populations may not be in local thermodynamic equilibrium (e.g., Christie et al., 2013; Yan et al., 2021). As a result, accurately determining total mass loss rates from these observations is difficult.

The detection of metals escaping from a planet is another window in which to observe atmospheric escape. Most observable spectral lines from metals come from high-energy ground-state electronic transitions, and therefore typically occur in the UV. As a result, like Lyman-α, these observations must be done from space. However, the star is not as intrinsically bright at these wavelengths compared to Lyman-α, leading to lower signal-to-noise ratios (Dos Santos, 2023). Additionally, the low abundance of metals in H/He-dominated atmospheres makes transit detections more challenging. As a result, detections have mostly been limited to highly irradiated giant planets with high mass loss rates (e.g., Haswell et al., 2012; Sing et al., 2019). Despite these challenges, metals remain of great interest because their presence provides evidence of hydrodynamic escape-they are too heavy to escape by other means. Moreover, since different spectral lines form in different regions of the outflow, they offer a more comprehensive view of the outflow dynamics.

Chapter 2

Modelling Lyman-α Transits

2.1 Introduction

Lyman-α transits offer the means to test models of atmospheric escape. However, interpreting observations is challenging because of the complexity of these outflows, which are only able to be properly modelled in three dimensions. The large body of three dimensional simulation work have revealed the important physical processes sculpting the planetary outflow and determining the properties of Lyman-alpha transits (e.g Bisikalo et al., 2013; Matsakos et al., 2015; Carroll-Nellenback et al., 2016; Bourrier et al., 2016; Khodachenko et al., 2019; McCann et al., 2019; Debrecht et al., 2020; Carolan et al., 2021a; MacLeod & Oklopčić, 2022). However, multi-dimensional (radiative)-hydrodynamics simulations are computationally expensive, therefore large parameter studies are infeasible. This is particularly problematic as the observed transit depends on uncertain stellar/planetary parameters (e.g. stellar wind mass loss rate, stellar wind velocity, stellar XUV radiation). This means that there has yet to be a systematic study of the properties of Lyman-α transits over the large parameter space of possible systems, which makes it difficult to be certain what information we can extract from Lyman-α transits. For example, it is unclear whether the non-detections of a Lyman-α transit from HD63433 b (Zhang et al., 2022b) or π Men c (García Muñoz et al., 2020) is due to these planets having a hydrogen dominated outflow that is too ionized to be detectable or the planets hosting a metal rich, H poor atmosphere. Even when simulations are able to match observations fairly well (e.g. Khodachenko et al. (2019) for transit of GJ436 b), it is uncertain whether the chosen parameters are the only possible set that can fit observations.

In this chapter, I develop a semi-analytic model that determines the trajectory, ionization state and 3D geometry of the outflow as a function of planetary and stellar parameters, based off the results of three-dimensional hydrodynamics simulations. I couple this to a ray-tracing routine to produce synthetic Lyman-α transits. The aim of such a model is to allow for a statistical retrieval of the properties of the escaping gas from Lyman-α transit observations. I emphasize that this model is not designed to replace three dimensional radiative-hydrodynamics simulations, which are the most accurate way to model planetary outflows. Conversely, it is created to: 1) narrow the parameter space in which to run hydrodynamic simulations; 2) understand the degeneracies between parameters, which illuminates the extent to which parameters of interest can be constrained and 3) provide realistic predictions of Lyman-α transits, which is essential for the efficient use of observational facilities.

2.2 Outflow Model

In this section, I build a model of the outflowing planetary gas in a steady state. I split the outflow into two components: inside and outside the Hill sphere of the planet. Inside the Hill sphere, the outflow is approximately spherically symmetric (e.g. Murray-Clay et al., 2009); thus, I model the flow as a 1D Parker wind (Parker, 1958). Outside the Hill sphere, 3D hydrodynamic simulations show that planetary outflow is sculpted into a cometary tail by the stellar tidal field and stellar wind ram pressure (e.g., Matsakos et al., 2015; Carroll-Nellenback et al., 2016; Khodachenko et al., 2019; McCann et al., 2019; Debrecht et al., 2020; Carolan et al., 2021a; Hazra et al., 2022; MacLeod & Oklopčić, 2022). Inspired by methods used to study disc winds (semi-) analytically (Fukue & Okada, 1990; Clarke & Alexander, 2016), I model the cometary tail as a streambundle, a collection of adjacent streamlines that form a tubular region of flow, and solve for its dynamics (e.g., Clarke & Alexander, 2016). The transition from a spherically symmetric outflow to a cometary tail cannot be modelled semi-analytically. However, the primary goal of this work is to understand the flow far outside the Hill sphere of the planet where a cometary tail is a good approximation. This is because Lyman-α

transits primarily probe material outside the planet's Hill sphere. Therefore, I choose to construct the full planetary outflow by "glueing" these two outflow models to each other at the Hill sphere of the planet, which I describe in Section 2.2.4. While the transiting Hill sphere region often has a small contribution to the transit profile, this approach allows us to have the outflow into the tail come from a physically motivated (although parameterised) outflow model.

This model excludes parts of the outflow leading the planet (outside the Hill sphere); therefore, I am not able to model the transit before the ingress of the Hill sphere. I note if there is significant absorption in Lyman-α before the ingress of the Hill sphere, then the calculated transit depth will be underestimated at ingress and extending through mid-transit, whilst this part of the outflow transits the star.

For moderate stellar winds, the pre-transit absorption may be highly variable because the gas leading the planet is unstable (e.g., Figure 1.7, McCann et al., 2019), which is challenging to model in a semi-analytic framework. As the model is not accurate in this region, I do not compare this part of the transit to observations. I note that for strong incident stellar winds, the pre-transit absorption is not variable (e.g., McCann et al., 2019; Khodachenko et al., 2019; Villarreal D'Angelo et al., 2021). Instead, the time of ingress depends on the position of the bow shock, which constrains the ratio between the stellar wind ram pressure and planetary wind ram pressure.

2.2.1 Model of Cometary Tail

In a frame co-rotating with the planet, I model the cometary tail as a streamline bundle with an elliptical cross-section. This is composed of a curve representing the trajectory of the tail, with ellipses stacked along it of variable height and depth. The variable s denotes the distance along the curve. The depth of the ellipse is small compared to the radius of curvature of the tail, and therefore, the tail does not intersect itself. At each point along this curve, I define a left-handed, local Cartesian coordinate system (l, a, ζ) with the origin at the ellipse's centre. I orient this coordinate system such that $\hat{\boldsymbol{l}}, \hat{\boldsymbol{a}}, \hat{\boldsymbol{\zeta}}$ point tangent to the trajectory of the tail, normal to the trajectory of the tail, and parallel to the orbital angular momentum of the planet, respectively. As the tail does not intersect with itself, any point can be specified by a distance along the tail s, and coordinates (a, ζ) in the corresponding ellipse.

We also define a global right-handed Cartesian coordinate system (x, y, z) co-rotating with the planet, with its origin at the star. The radial distance from the star is denoted by r. I choose the (x, y) coordinates to lie in the planet's orbital plane so that the trajectory of the tail also lies in the orbital plane (i.e. $s = s(x, y)$). Given a point along the tail $s_0 = (x_0, y_0)$, a point in the corresponding cross-sectional plane is given by:

$$x = x_0 - a \sin\tau \tag{2.1}$$

$$y = y_0 - a \cos\tau \tag{2.2}$$

$$z = \zeta \tag{2.3}$$

where τ is the angle between $\hat{\boldsymbol{l}}$ and $\hat{\mathbf{x}}$ measured anticlockwise. Figure 2.1 shows a sketch of the model and coordinate systems. For simplicity, I consider both the velocity and the ionization fraction of the gas in the tail to be a function of the distance s along the tail only. These simplifications allow us to separately model the bulk motion (i.e. the trajectory), ionisation state, geometry and density structure of the outflow. The model, therefore, consists of three parts:

(i) Self-consistently solving for the trajectory of the tail in the planet's orbital plane by assuming a generalised geostrophic balance.

(ii) Solving for the neutral fraction of hydrogen atoms along the tail using the optically thin ionisation equation.

(iii) Solving for the height, depth and density structure of this streambundle, assuming the gas is in hydrostatic equilibrium in the cross-section of the streambundle.

Modelling the tail as a streambundle implicitly treats the planetary outflow as a fluid as opposed to the particle approach used in some simulations of the outflow (e.g., Bourrier & Lecavelier des Etangs, 2013; Ehrenreich et al., 2015; Bourrier et al., 2015). At 10^4 K, the proton-hydrogen cross section is $\sim 10^{-14}$ cm^2 (Schultz et al., 2008). Typically, proton number densities in the planetary outflow are $\gtrsim 10^5$ cm^{-3} (e.g. McCann et al., 2019), therefore the mean free path for a neutral hydrogen is

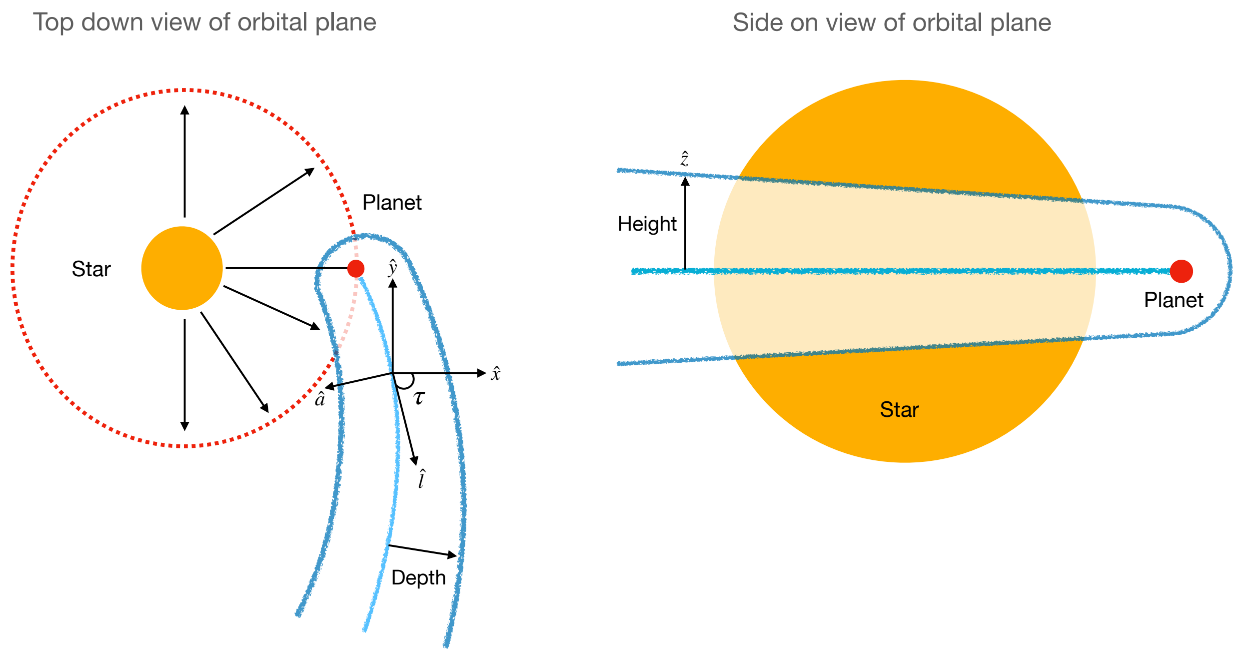

Figure 2.1: A schematic diagram of the planetary outflow that is sculpted into a cometary tail by the stellar tidal field and stellar wind ram pressure. The light blue curve represents the trajectory of the tail, which is parameterised by a coordinate (s), representing the distance along this curve. At each point along this curve, I define a local (left-handed) cartesian coordinate system (l, a, ζ) that can be related to a global cartesian coordinate system (x, y, z) centred on the star. I solve for i) the trajectory, ii) the ionization state, and iii) the geometry of the tail as a function of system parameters shown in Table 2.1.

$\lesssim 10^9$cm, which is generally small compared to the scale of the outflow; therefore, treating the gas as collisional is valid. I check this condition in the simulated outflows post-facto to ensure that it holds.

Trajectory of the Tail

In a reference frame co-rotating with the planet, in which I treat the flow as steady, I solve for the trajectory of the tail as a 1D streamline subject to momentum conservation.

$$(\mathbf{u} \cdot \nabla)\mathbf{u} = \mathbf{a}_{\rm sw} - \nabla\phi - 2\mathbf{\Omega} \times \mathbf{u} \tag{2.4}$$

where $\mathbf{a}_{\rm sw}$ is the acceleration due to ram pressure of the stellar wind, $\nabla\phi$ is effective potential, and $2\mathbf{\Omega} \times \mathbf{u}$ is the Coriolis force. I assume the planet has a circular orbit and ignore the Euler force (it is not possible to construct a steady-state model of an eccentric orbit). Although the stellar wind ram pressure force is a surface force, I approximate that this force is applied like a body force, as pressure gradients quickly distribute this force across the tail. Furthermore, geostrophic balance keeps the tail stable. I discuss the validity of this approximation later in this section. In this framework, the force per unit length that the stellar wind applies to the tail is:

$$\frac{d\mathbf{p}}{dt} = 2H\rho_*(\mathbf{u}_* - \mathbf{u}\cos\chi)^2\sin\chi\;\hat{\mathbf{u}}_* \tag{2.5}$$

where H is the height of the tail, ρ_* and $\mathbf{u}_*$ are the stellar wind density and velocity, respectively, and χ is the angle between the tangent of the tail and the direction stellar wind. In the case where the stellar wind is strong, simulations show that all the mass lost from the planet is directed down the cometary tail (e.g., McCann et al., 2019). Therefore, I can define the mass per unit length in the tail:

$$\lambda = \frac{\dot{M}_p}{u} \tag{2.6}$$

where $\dot{M}_p$ is the mass loss rate of the planet and $u = |\mathbf{u}|$. Therefore, the acceleration of the tail due to stellar wind ram pressure is given by:

$$\mathbf{a}_{\rm sw} = \frac{2Hu\rho_*(\mathbf{u}_* - \mathbf{u}\cos\chi)^2\sin\chi}{\dot{M}_p}\hat{\mathbf{u}}_* \tag{2.7}$$

For this framework to be valid, the timescale for pressure waves to distribute this force across the tail must be shorter than the timescale in which the forces acting on the tail significantly change. I estimate this by comparing the acceleration timescale to the sound crossing time as:

$$\frac{\tau_{sc}}{\tau_a} = \frac{\mathrm{dlog}u}{\mathrm{dt}}\frac{2D}{c_s} \tag{2.8}$$

where c_s is the isothermal sound speed of the gas in the outflow and D is the depth of the tail. Taking the conservative assumption that $u_* \gg u$ and $\sin\chi = 1$, so that $a_{\rm sw} \sim (2Hu_*^2\rho_*)/\dot{M}_p$, this equals

$$\frac{\tau_{sc}}{\tau_a} \lesssim \frac{1}{\pi}\left(\frac{\dot{M}_*}{\dot{M}_p}\right)\left(\frac{u_*}{c_s}\right)\left(\frac{HD}{r^2}\right) \tag{2.9}$$

For a typical sub-Neptune around a solar-like star at 0.03 AU, this is smaller than one.

$$\begin{aligned}\frac{\tau_{sc}}{\tau_a} \lesssim & \left(\frac{\dot{M}_*}{10^{12}\ \mathrm{g\ s^{-1}}}\right)\left(\frac{\dot{M}_p}{10^{10}\ \mathrm{g\ s^{-1}}}\right)^{-1}\left(\frac{u_*}{100\ \mathrm{km\ s^{-1}}}\right) \\ & \times\left(\frac{c_s}{10\ \mathrm{km\ s^{-1}}}\right)^{-1}\left(\frac{HD}{3\times10^{-3}r^2}\right)\end{aligned} \tag{2.10}$$

where H and D are conservatively estimated using the distance that a ballistic particle travels after being launched from the planet at 10 km s^{-1}.

As this estimate is an upper limit, it is reasonable to approximate the total effect of stellar wind ram pressure to apply a force equal to the momentum flux throughout the tail. Additionally, in this framework, the height and depth scales like the bow shock radius. Therefore, increasing the stellar wind mass loss rate or velocity should reduce the height and depth equivalently so that the argument still holds.

We also test the validity of this approach by comparing the tail trajectories that I have calculated with this model to multiple 3D hydrodynamic simulations (see Section 2.3 and Figure 2.2). Detailed inspection of publicly available simulation outputs demonstrates that this model is able to replicate the trajectories of these simulations using the same system parameters, indicating that my assumptions are reasonable.

Geometry of the Tail

A corollary of the previous argument is that the gas inside the tail should adjust to its local conditions. Therefore, in the elliptical cross-section of the tail, the gas is approximately in hydrostatic equilibrium. Perpendicular to $\hat{\boldsymbol{l}}$, the forces on a parcel of gas are:

$$-\frac{1}{\rho(a,z)}\nabla P(a,z) - \nabla\phi(a,z) - 2\boldsymbol{\Omega}\times\mathbf{u} + \frac{\mathbf{u}^2}{r_c(a)}\hat{\mathbf{a}} = 0 \tag{2.11}$$

where ρ and P are the density and pressure, respectively, and r_c is the radius of curvature corresponding to streamlines in the outflow. Note that this equation is also an implicit function of the distance along the tail $s = (x, y)$. The effective potential is:

$$\begin{aligned}\phi = &-\frac{GM_*}{\sqrt{(x - a\sin\tau)^2 + (y - a\cos\tau)^2 + z^2}} \\ &- \frac{1}{2}\Omega^2 \left((x - a\sin\tau)^2 + (y - a\cos\tau)^2\right)\end{aligned} \tag{2.12}$$

Since the height and depth of the tail are small compared to the distance from the star, I expand the effective potential and radius of curvature to second-order in terms of $\left(\frac{a}{r}, \frac{z}{r}\right)$. Up to this order, the horizontal (a) and vertical (z) coordinates decouple; therefore, the density is separable, and each direction can be solved independently. For simplicity, I solve for the density using an isothermal equation of state such that $P = c_s^2\rho$. In the vertical direction, the density distribution is given by

$$-\frac{c_s^2}{\rho(z)}\frac{\partial\rho(z)}{\partial z} - \frac{GM_* z}{r^3} = 0 \tag{2.13}$$

which can be analytically solved as

$$\rho(z) = \rho_{a,0}\exp\left[-\frac{GM_* z^2}{2c_s^2 r^3}\right] = \rho_{a,0}\exp\left[-\frac{\Omega_k^2 z^2}{2c_s^2}\right] \tag{2.14}$$

where $\rho_{a,0}$ is the density in the orbital plane at horizontal coordinate a and Ω_k is the Keplerian angular velocity. This is just the standard solution for vertical hydrostatic equilibrium of a rotating fluid (e.g. in a disc).

Following the same procedure to calculate the horizontal density distribution, assuming that the velocity of the gas is constant across the cross-sectional slice of the tail, can lead to an unphysical distribution of angular momentum throughout the tail. Fixing the velocity of gas to be constant forces the angular momentum of the gas to vary linearly across the tail. For large depths, this can lead to an unphysically high (or low) gas angular momentum at the edges of the tail.

Instead, I approximate the depth by assuming that the angular momentum difference between the edge of the tail and the centre stays constant, where the initial dispersion is approximated by launching particles at the sound speed with varying angular momenta from the planet. In the limit where the orbital velocity of the planet is greater than the velocity of the tail, the depth $\sim \frac{c_s}{\Omega_k}\sqrt{\frac{a_p}{r}} \sim \frac{c_s}{\Omega_k}$, where a_p is the semi-major axis of the planet. This agrees with the typical depths found in simulations for weak incident stellar winds. For stronger stellar winds, the depth is smaller as the stellar wind compresses the tail. Therefore, a sensible choice for a density distribution is:

$$\rho(a) \propto \exp\left[-\frac{\Omega_k^2 a^2}{c_s^2}\right] \tag{2.15}$$

To calculate the optical depth of the tail in transit, the density profile is integrated (almost) horizontally through the tail, and therefore, the transit depth will only be weakly dependent on this choice. Given this choice, the total density structure is given by:

$$\rho = \rho_0 \exp\left[-\frac{a^2}{\alpha^2} - \frac{z^2}{\beta^2}\right], \quad \alpha = \frac{c_s}{\Omega_k}, \quad \beta = \frac{\sqrt{2}c_s}{\Omega_k} \tag{2.16}$$

where ρ_0 is the density at the centre of the ellipse. In order to find the height, depth and ρ_0 of the tail, three constraints must be applied. The first of these comes from equating the mass-flux to the integral of the density over the elliptical cross-section. The latter two are given by specifying conditions at the boundary between the planetary and stellar wind. As the stellar wind is incident on the inner edge of the tail, conditions vary substantially on either side of the tail. I choose to evaluate this at the inner edge and top of the ellipse (we could equivalently define it a the bottom), where these boundaries are well-defined. These three constraints can be written as:

$$\text{i)} \iint_{\mathcal{A}} \rho(a,z)\, da dz = \frac{\dot{M}_p}{u} \quad \text{(Mass per unit length)} \tag{2.17}$$

$$\text{ii)}\ \rho(-D,0)c_s^2 = P_{\mathrm{sw},D} \quad \text{(Pressure at inner edge)} \tag{2.18}$$

$$\text{iii)}\ \rho(0,H)c_s^2 = P_{\mathrm{sw},H} \quad \text{(Pressure at upper edge)} \tag{2.19}$$

where $\mathcal{A}$ is the area of the ellipse and $P_{\mathrm{sw},D}$ and $P_{\mathrm{sw},H}$ is the stellar wind pressure at the inner edge and top of the tail respectively. The stellar wind incident on the planetary outflow is shocked. In the orbital plane, I approximate the shock front to be parallel to the trajectory of the tail, and in the vertical plane, it forms a bow shock. Since simulations indicate that the bow shock is not thin, there are no general analytic ways to calculate the shape of a bow shock or the downstream pressure. However, it is possible to solve for the pressure at the nose of the shock using the oblique shock equations. For simplicity, I assume that the pressure at the inner edge and top of the tail are equal and are a linear scaling of the pressure at the nose.

$$\kappa P_{\text{nose}} = P_{\text{sw},D} = P_{\text{sw},H} \tag{2.20}$$

As the pressure is expected to decrease as the gas moves away from the nose, $\kappa < 1$, I set $\kappa = 0.3$ using Schulreich & Breitschwerdt (2011) as a guide. With this simplification, using Equations 2.16, 2.18, 2.19, the depth and height are related as:

$$\frac{D}{\alpha} = \frac{H}{\beta} \tag{2.21}$$

The integral in Equation 2.17 cannot generally be solved analytically. However, it can be written in terms of special functions (e.g Waugh, 1961).

$$\frac{1}{2\pi}\iint_{\mathcal{A}} e^{-\frac{x^2+y^2}{2}} dxdy = p\left(\frac{A+B}{2}, \frac{A-B}{2}\right) - p\left(\frac{A-B}{2}, \frac{A+B}{2}\right) \tag{2.22}$$

$$p(R,r) = e^{-\frac{r^2}{2}} \int_0^R e^{-\frac{t^2}{2}} I_0(rt)tdt \tag{2.23}$$

where A, B are the semi-major and semi-minor axes of the ellipse, $\mathcal{A}$ is the area of the ellipse and I_0 is the modified Bessel function of the first kind. In the special case given by Equation 2.21, this can be solved exactly to give:

$$D = \alpha \ln\left(\frac{\dot{M}_p c_s^2}{u\pi\gamma P_{\text{nose}}\alpha\beta} + 1\right) \tag{2.24}$$

$$H = \frac{\beta}{\alpha} D \tag{2.25}$$

Ionization of Tail

As absorption of Lyman-α radiation is from neutral hydrogen, it is essential to calculate the ionization state of hydrogen in the tail. In the photoevaporation model, where the absorption of EUV photons launches the planetary outflow, the tail must be optically thin to EUV photons; otherwise, the EUV flux absorbed at the base of the flow would be too small to drive a large outflow (Owen et al., 2023). Owen et al. (2023) showed that this extends to core-powered mass loss outflows, which are not driven by EUV radiation. As a result, the photoionization rate of neutral hydrogen is approximately constant in each cross-sectional slice of the tail (also noting that $D, H \ll r$).

We also include hydrogen recombination in this model. For old small planets, whilst observable, the gas in the tail is far way from photoionization-recombination equilibrium, and therefore, the effect of recombination is minimal. However, for giant planets or young planets with high mass loss rates, the outflows may be dense enough for recombination to be important. As recombination is density-dependent, it varies down the tail. For simplicity, I approximate that the recombination rate of neutral hydrogen is constant in each cross-sectional slice of the tail and equivalent to the mean density in that slice. The number density, n, of protons and hydrogen atoms in a cross-sectional slice of the tail is:

$$n = \frac{\dot{M}_p}{\pi u H D m_H} \tag{2.26}$$

As such, calculating the ionization fraction can be simplified to a 1D problem, which depends on distance (s) down the tail. In this limit, the ionization equation as a parcel of gas moves down the tail is:

$$\frac{DX}{Dt} = (1 - X)\Gamma - nX^2\alpha_A \tag{2.27}$$

where X is the ionisation fraction, Γ is the photoionisation rate and α_A is the Case A recombination coefficient. I can use the Case A recombination coefficient because the tail is optically thin to recombination photons. This is because photons with energies > 13.6 eV, that are produced by a hydrogen atom recombining directly to the ground state generally escape the tail rather than ionizing another hydrogen atom.

The optically thin photoionization rate is given by:

$$\Gamma = \int_{13.6\text{ eV}}^{\infty} \frac{L_\nu}{4\pi r^2 h\nu}\sigma_\nu d\nu \tag{2.28}$$

where ν is the frequency of a photon, σ_ν is the photoionization cross section of hydrogen as a function of frequency, and L_ν is the luminosity of the star as a function of frequency. To map the optically thin photoionization rate to an EUV luminosity requires a stellar spectrum. Assuming a "perfect" stellar spectrum, f_ν, that has been normalised to unity in the EUV range, the integrated EUV luminosity can be mapped to the optically thin ionization rate as follows:

$$\Gamma = L_{\text{EUV}} \int_{13.6\text{ eV}}^{100\text{ eV}} \frac{f_\nu}{4\pi r^2 h\nu} \sigma_\nu d\nu \tag{2.29}$$

where L_{EUV} is the luminosity integrated over the EUV range. As σ_ν peaks at 13.6 eV and decreases strongly as a function of frequency, $\propto \left(\frac{\bar{\nu}}{\nu}\right)^3$ (e.g., Spitzer, 1978), harder spectra lead to a smaller photoionization rate for the same integrated EUV luminosity. As the optically thin photoionization rate is the physical quantity that determines the ionization structure in the tail, this quantity is specified in the model rather than a stellar EUV luminosity.

Thus, in steady state, the governing equation for the ionization fraction becomes:

$$\frac{d\mathcal{N}}{ds} = -\frac{\Gamma\mathcal{N}}{u} + \frac{n(1-\mathcal{N})^2\alpha_A}{u} \tag{2.30}$$

where $\mathcal{N} = 1 - X$ is the neutral fraction of hydrogen.

Stellar Wind

In order to calculate the acceleration of the tail due to the stellar wind, one must specify the velocity and density of the stellar wind. For simplicity, I treat the stellar wind as spherically symmetric, such that the density, velocity, and mass loss rate of the star can be linked through mass conservation as:

$$\dot{M}_* = 4\pi r^2 \rho_* u_* \tag{2.31}$$

where $\dot{M}_*$ is the mass loss rate of the star. In this exploratory work, I also choose the stellar wind to impact the tail radially. I note that the outflow model, along with the simulations it is based on, is only valid for planets located outside the Alfvén surface of the star where the ram pressure of wind dominates over the magnetic pressure of the star. The velocity structure of the stellar wind can be specified as an input parameter, which can be taken from stellar wind simulations. For simplicity, here, I take the stellar wind velocity to be constant as the tail gets radially pushed outward. This is valid if the planet lies outside the acceleration zone of the stellar wind. I note that many evaporating planets are very close to their stars, such that the stellar wind is still accelerating.

With this approximation, the ram pressure of the stellar wind is:

$$\rho_* u_*^2 = \frac{\dot{M}_* u_*}{4\pi r^2} \tag{2.32}$$

Although I have ignored many of the intricacies of the stellar wind, I highlight that Lyman-α transits are probing the stellar wind conditions near the planet. A possible complication with this arises when stellar wind conditions can vary considerably along the orbit of the planet. However, more complicated stellar wind conditions could be added to the model relatively simply.

Method of Solution

It appears that I have to solve a system of coupled partial differential equations for the trajectory, ionization fraction, and geometry of the tail. However, as the domain of all the functions in these equations is the 1D trajectory curve, they can be written as a function of distance along the tail (s). This system can equivalently be written as a set of coupled ordinary differential equations:

$$u\frac{du_x}{ds} = (\mathbf{a}_{\rm sw})_x - (\nabla\phi)_x + 2\Omega u_y \tag{2.33}$$
$$u\frac{du_y}{ds} = (\mathbf{a}_{\rm sw})_y - (\nabla\phi)_y - 2\Omega u_x \tag{2.34}$$
$$\frac{dx}{ds} = \frac{u_x}{u} \tag{2.35}$$
$$\frac{dy}{ds} = \frac{u_y}{u} \tag{2.36}$$
$$\frac{d\mathcal{N}}{ds} = -\frac{\Gamma\mathcal{N}}{u} + \frac{n(1-\mathcal{N})^2\alpha_A}{u} \tag{2.37}$$
$$D = \alpha \ln\left(\frac{\dot{M}_p c_s^2}{u\pi P_{{\rm sw},D}\alpha\beta} + 1\right) \tag{2.38}$$
$$H = \frac{\beta}{\alpha}D \tag{2.39}$$

where the notation $(\mathbf{A})_i$ represents the component of the vector $\mathbf{A}$ in the i direction. I solve these implicitly using an implementation of a backward differentiation formula method (BDF) (Byrne & Hindmarsh, 1975) provided in the *scipy* library (Virtanen et al., 2020). The relative and absolute tolerance used were 1×10^{-13} and 1×10^{-14}, respectively.

2.2.2 Spherical Wind

Inside the Hill sphere, the outflow is approximately spherically symmetric, allowing it to be modelled using a 1D spherically symmetric coordinate system. To remain agnostic about the driving mechanism, the outflow is modelled as a constant sound speed Parker wind, parametrised by a constant mass-loss rate and sound speed. The force of stellar gravity is included so that the sonic point of the flow cannot be outside the Hill sphere of the planet (Vissapragada et al., 2022). This breaks the spherical symmetry of the setup. For planets, where the acceleration of the outflow is dominated by gas pressure rather than stellar gravity, the effect of stellar gravity on the flow structure is minimal. Therefore, I calculate the flow along a ray originating from the sub-stellar point on the planet and use that to calculate the full 3D flow structure of the outflow inside the Hill sphere. For a given mass loss rate and sound speed, the velocity of the outflowing gas is analytically given by:

$$u = \begin{cases} -W_0[-\mathcal{D}(r')] & r' \leq r_{cr} \\ -W_{-1}[-\mathcal{D}(r')] & r' > r_{cr} \end{cases} \tag{2.40}$$

$$\mathcal{D}(r') = \left(\frac{r'}{r_{cr}}\right)^{-4} \exp\left[4r_\alpha\left(\frac{1}{r_{cr}} - \frac{1}{r'}\right) + \frac{2r_\alpha}{R_H^3}(r_{cr}^2 - r'^2) - 1\right] \tag{2.41}$$

where r' is the radial distance from the planet, W_k is the Lambert W function on branch k (Cranmer, 2004), r_{cr} is the sonic point of the flow, r_α is the sonic point for the flow without tidal gravity and R_H is the Hill radius of the planet. I calculate the fraction of ionized hydrogen by analogy with the method for the calculating the ionized fraction in the tail. Thus I use:

$$\frac{\partial \mathcal{N}}{\partial r'} = -\frac{\Gamma e^{-\tau_{\bar{\nu}}(r')}\mathcal{N}}{u} + \frac{\dot{M}_p(1-\mathcal{N})^2\alpha_A}{4\pi r'^2 u^2 m_p} \tag{2.42}$$

We include the optical depth of the outflow to 20 eV photons, $\tau_{\bar{\nu}}$, in the photoionization part of the equation to account for the fact that the outflow can be optically thick near the planet. Using a single photon energy, rather than a stellar spectrum, to calculate the optical depth does not give an accurate ionization fraction deep in the atmosphere of the planet where the wind is launched (e.g., Trammell et al., 2011). The overall transit depth is dominated by the flow at larger radius, where the outflow is optically thin to EUV radiation. This is because the outflow is still generally optically thick to Lyman-α photons (even in the observable wings) at these larger radii due to large difference between the EUV and Lyman-α cross sections ($\sim$ 4 orders of magnitude), despite the decreasing density of neutral hydrogen. As the optically thin region (to EUV radiation) covers a significantly larger area of the star than the optically thick region, it dominates the contribution to the transit depth. Therefore, I am primarily concerned with approximating the ionization fraction in the optically thin region well. As I specify the optically thin ionization rate in the model, the ionization fraction in this region is approximated well.

Equation 2.42 has to be solved iteratively as $\tau_{\bar{\nu}}(r')$ depends on the ionization fraction of the outflow. However, one can approximate $\tau_{\bar{\nu}}(r')$ by assuming the atmosphere is neutral and solving the differential equation directly (e.g., Dos Santos et al., 2022). I solve this using an implementation of the LSODA method (Petzold, 1983) provided in the *scipy* library (Virtanen et al., 2020). The absolute and relative tolerances used are 1×10^{-13} and 1×10^{-13} respectively.

Although modelling the outflow inside the Hill sphere as a Parker wind is not as accurate as a self-consistent EUV heated (e.g., Murray-Clay et al., 2009) or bolometrically heated (e.g., Schulik & Booth, 2023) model, I emphasize that the primary motivation of modelling the Hill sphere is to find the initial conditions of the gas entering the tail. As mentioned previously, this also allows us to remain agnostic to the exact physics that is driving the outflow. This agnostic nature then allows us to test the prediction of various classes of escape models (e.g., photoevaporation vs core-powered mass-loss).

2.2.3 Energetic Neutral Atoms

The interaction between the stellar wind and the planetary outflow also results in charge exchange between the stellar wind protons and neutral hydrogen in the outflow. There is little momentum transfer between the atoms in this process (e.g., Pinto & Galli, 2008), and therefore it generates a high-velocity neutral atom. The production of these high-velocity neutral atoms, known as energetic neutral atoms (ENAs), has been proposed as the source of the large Lyman-α transits in some systems (e.g., Holmström et al., 2008; Kislyakova et al., 2014; Bourrier et al., 2016; Khodachenko et al., 2019).

There are a range of approaches used to model the generation of ENAs in the literature: particle-based (e.g., Holmström et al., 2008; Bourrier et al., 2016), single-fluid (e.g., Tremblin & Chiang, 2012; Debrecht et al., 2022) or multi-fluid (e.g., Khodachenko et al., 2019). In this work, I adopt a single-fluid description of the production of ENAs. This assumes that stellar wind protons cannot penetrate into the planetary outflow and are forced around the flow. The resulting velocity shear at the boundary between the stellar and planetary wind creates Kelvin-Helmholtz instabilities turbulently mixing the stellar wind and planetary gas. Charge exchange between stellar wind protons and planetary neutral hydrogen atoms in this turbulent mixing layer generates ENAs.

The single fluid framework is valid when the mean free path of stellar wind protons in the planetary outflow is small compared to the scale of the planetary outflow. To ensure that it is justified to use framework, I post-facto check that these conditions hold for the simulated outflows, shown in Section 2.6.2

I estimate the number density of ENAs in the turbulent mixing layer using analytic arguments from Tremblin & Chiang (2012); Owen et al. (2023). The rate of production of ENAs is given by:

$$\beta(n_{+,*}n_{0,p} - n_{0,*}n_{+,p}) \tag{2.43}$$

where $n_{+,*}$ and $n_{+,p}$ are protons of stellar wind and planetary wind origin respectively, $n_{0,*}$ and $n_{0,p}$ are neutral hydrogen atoms of stellar and planetary origin respectively and β is the charge exchange rate coefficient. In the mixing layer where the stellar and planetary wind are interacting, the collisional timescale is much shorter than the timescale for ENAs to get advected off the limb of the star, it can be assumed that the stellar wind protons and planetary atoms are in chemical equilibrium. Therefore, the number density of ENAs in the mixing layer can be approximated as:

$$n_{\mathrm{ENA}} = \mathcal{N} n_{*} \tag{2.44}$$

where n_{*} is the density of the post-shocked stellar wind and $\mathcal{N}$ is the neutral fraction of hydrogen in the tail.

The contribution of ENAs to the Lyman-α optical depth also depends on the velocity and temperature of these atoms and the size of the mixing layer. The collision and subsequent diversion of the stellar wind around the tail may cause the bulk velocity of ENAs in the mixing layer to be different to the initial stellar wind velocity. As there is not any a priori way of calculating the bulk velocity of ENAs (without resorting to advanced simulations), I treat it as a constant that is allowed to be a free parameter of the model. Elastic collisions between atoms of stellar and planetary origin in the mixing layer cool the atoms of the stellar origin. For simplicity, I ignore this process and set the temperature of ENAs to be the same as the stellar wind temperature.

Raga et al. (1995) analytically studied the size of the mixing layer for the interaction between a spherical outflow with a planet parallel flow. To do this calculation, they had to assume that the stand-off distance between the two shocks was small compared to the radius of curvature of the shock front. This is not the case for the interaction between the stellar wind and the planetary outflow, where the shocked regions can be thick. However, using this as a guide and inspecting the simulations performed by Tremblin & Chiang (2012); Debrecht et al. (2022) allows us to estimate the width of the mixing layer to range from a few to tens of per cent of the depth of the tail. As this range is fairly large, I choose to treat the size of the mixing layer as a free parameter, specified by L_{mix}, which represents the fractional size of the mixing layer compared to the radius of curvature of the planetary outflow that the stellar wind impinges on.

For ENAs generated due to the interaction of the stellar wind with the Hill sphere of the planet, the mixing layer is given by the area between spheres with Hill sphere radius r_H and $r_H(1 + L_{\mathrm{mix}})$. For ENAs generated in the tail, the mixing layer is given by the area between an ellipse with a height and depth given by H, D and an ellipse with a height and depth given by $H(1 + L_{\rm mix}), D(1 + L_{\rm mix})$ respectively.

2.2.4 Constructing the Full Outflow Model

In order to construct the full outflow model, there needs to be a transition from the spherically symmetric outflow inside the Hill sphere into the cometary tail-like outflow. I do this by "glueing" the tail onto a point on the Hill sphere of the planet. The initial speed and ionization fraction of the gas in the tail are specified by the values given by the spherical wind model evaluated at the Hill sphere. With this formulation, there is still freedom to choose exactly at what position to glue the tail onto the Hill sphere and the initial direction of the outflow. To simplify this, I assume that the initial position and velocity vector of the tail, in a frame centred on the planet, are parallel. This information can be encoded in a free parameter h, which I interpret as the relative specific angular momentum between the outflow and the planet. I shall refer to this quantity as the angular momentum deficit of the outflow, and it can be written as:

$$h = \Omega(a_p^2 + 2a_p R_H \sin\theta + R_H^2) + u\cos\theta\sqrt{a_p^2 + 2a_p R_H \sin\theta + R_H^2} \tag{2.45}$$

where θ is the angle at which the tail is glued onto the Hill sphere of the planet, and a_p is the semi-major axis of the planet. The projected area of this transition region that blocks the star relative to the rest of the tail is $\sim \frac{R_H^2}{R_* H}$, which is generally small, and therefore this uncertainty should not have a large effect on the results. Furthermore, the primary aim of this work is to model the transit on scales much larger than the Hill sphere of the planet where the geometry of the model matches 3D simulations.

The full outflow model requires 14 input parameters, shown in Table 2.1. These can be roughly divided into "tightly constrained" and "weakly constrained" parameters. The "tightly constrained" are ones, like the planet's or the star's radius, that are generally well constrained by independent observations. In general, when comparing the simulations to observations, the "weakly constrained" parameters will be free, and the "tightly constrained" parameters will be fixed (or given tight priors).

Table 2.1: The input parameters for the outflow model. The parameters can be roughly divided into those that are tightly constrained by independant observations and those that are weakly constrained.

Tightly Constrained	Weakly Constrained
Planet radius, R_p	Sound speed, c_s
Planet mass, M_p	Planet mass loss rate, $\dot{M}_p$
Stellar mass, M_*	Stellar wind velocity (at planet), u_*
Semi-major axis of orbit, a_p	Star mass loss rate, $\dot{M}_*$
Orbital inclination, i	Optically thin photoionization rate (at planet), Γ_p
	Stellar wind temperature, T_{sw}
	Angular momentum deficit of outflow, h
	Bulk velocity of ENAs, u_{ENA}
	Width of turbulent mixing layer, L_{mix}

2.3 Comparison to 3D Hydrodynamics Simulations

To demonstrate that this model is accurate in predicting the geometry of the outflowing gas, I compare the trajectory that the model predicts with those obtained from 3D hydrodynamics simulations. I do this for four simulation setups described in McCann et al. (2019); Khodachenko et al. (2019); MacLeod & Oklopčić (2022); and Hazra et al. (2022). These simulations examine the outflow for a range of planetary and stellar properties to highlight the model's applicability over a wide range of parameters, shown in Table 2.3. For the comparison to be meaningful, the free parameters in my model are fixed to be the same as those used in the respective simulation. In each case, the planetary mass loss rate, stellar wind mass loss rate, and stellar wind temperature are provided in the simulation paper. They also provide a temperature plot of the outflow, which is used to estimate the sound speed of the gas. These values are also provided in Table 2.3. Finally, the angular momentum deficit, h, is not fixed from the initial simulation parameters, so I can approximate it by looking at the direction of the gas flow at the beginning of the tail. The values of the angular momentum deficit, normalized to the angular momentum of the planet, are also provided in Table 2.3.

Figure 2.2 shows the trajectory of the tail calculated using my model superimposed on the outflow produced from 3D hydrodynamics simulations. The model is successful in reproducing the trajectory of the simulated tails in all the simulations, and this gives us confidence that it can be used to test atmospheric escape models quantitatively.

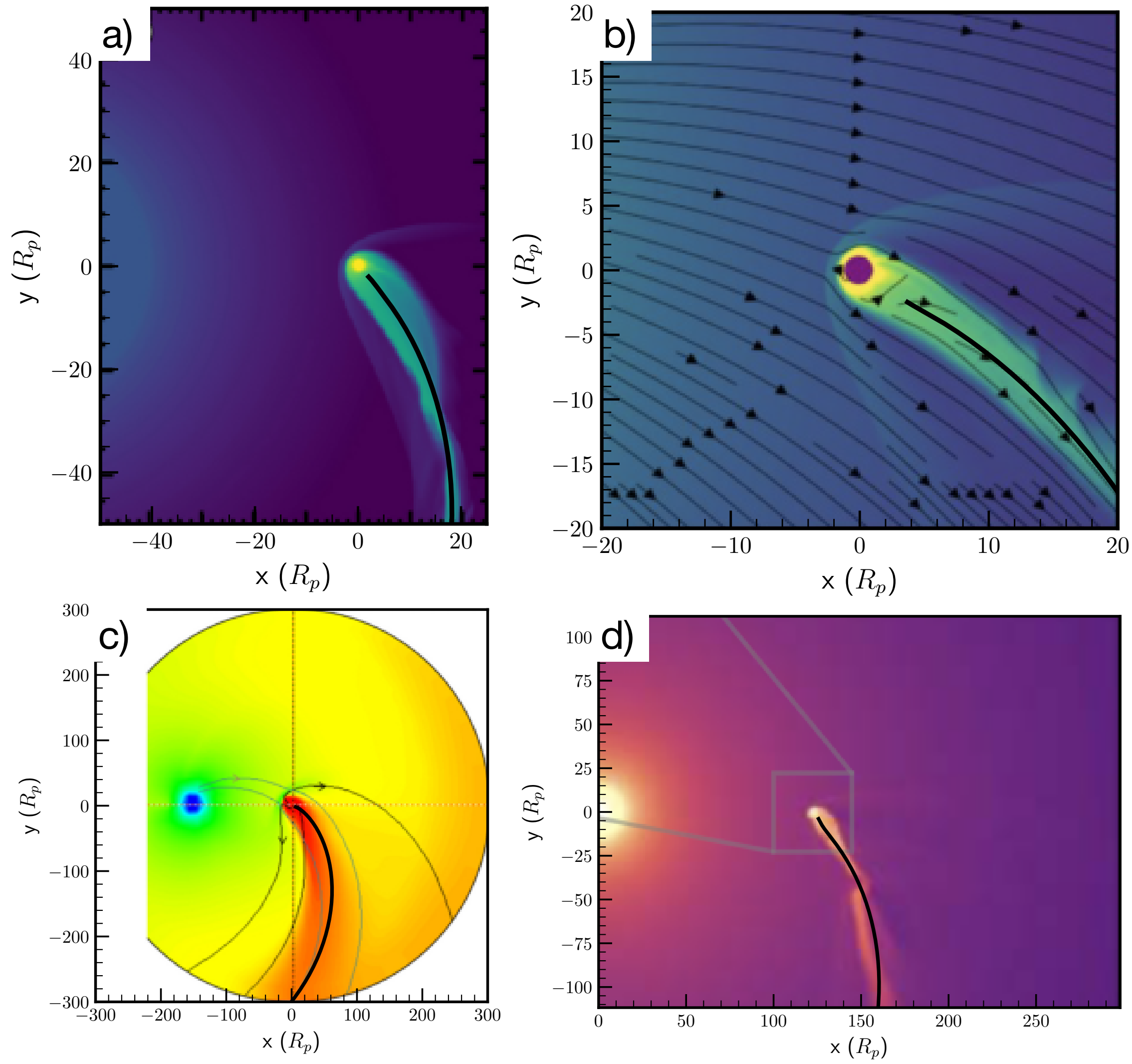

Figure 2.2: Each panel shows the geometry of the planetary outflow produced from 3D hydrodynamics simulations, with planet and system parameters listed in Table 2.3. The trajectory of the tail, calculated by my model using the same parameters, is shown by the thick black line.

Table 2.2: The input parameters used to calculate the trajectory of the tail of gas trailing the planet. These parameters (with the exception of angular momentum deficit) match those in the 3D hydrodynamic simulations so that a meaningful comparison can be made between the semi-analytic model and simulations.

Label	Stellar Mass ($M_\odot$)	Planet Mass (M_J)	Planet Radius (R_J)	Planet Mass Loss Rate (g s^{-1})	Outflow Sound Speed (km s^{-1})	Stellar Mass Loss Rate (g s^{-1})	Stellar Wind Velocity (km s^{-1})	Angular Momentum Deficit	Reference
a	1.00	0.26	2.1	3.4×10^{10}	11.0	3.7×10^{12}	180	-0.05	McCann et al. (2019)
b	0.82	1.10	1.1	1.0×10^{11}	11.0	1.9×10^{14}	240	0.07	Hazra et al. (2022)
c	0.45	0.07	0.4	2.0×10^{9}	9.0	2.5×10^{11}	170	0.02	Khodachenko et al. (2019)
d	0.68	0.10	0.1	7.2×10^{9}	6.0	1.8×10^{11}	150	-0.06	MacLeod & Oklopčić (2022)

2.4 Computing Synthetic Transit Profiles

The main goal of this model is to generate synthetic transmission spectra for comparison with observational data. A ray-tracing approach is employed to calculate the attenuation of Lyman-α caused by the transit of the outflow across the stellar disc. Observations at various orbital phases are simulated by rotating the outflow around the system's barycenter, which is approximated as the center of the star. To determine the Lyman-α attenuation at a specific orbital phase, a 3D cylindrical grid is constructed as the tensor product of a 2D grid on the stellar disc with a 1D grid along the line connecting the stellar disc's center to the observer. A new Cartesian coordinate system is then defined, centered on the stellar disc. The x_t and y_t axes are parallel to the stellar disc, and the z_t axis is given by the line connecting the centre of the stellar disc to the observer. A schematic of the approach is shown in Figure 2.3. The 2D grid consists of 705 cells. For ray tracing through the tail, the 1D grid consists of a minimum of 10 cells across the width of the tail. For ray tracing through the Hill sphere, the 1D grid consists of 15 cells. I did resolution tests in order to check that this number of cells was sufficient.

The optical depth through the outflow for a corresponding point on the stellar disc is given by

$$\tau_\nu(x_t, y_t) = \int_0^\infty n_{\mathrm{HI}}(x_t, y_t, z_t)\sigma_\nu(u_{z_t}, T)dz_t \tag{2.46}$$

where n_{HI} is the number density of hydrogen atoms, σ_ν is the absorption cross-section of hydrogen to photons of frequency ν, which is a function of the line of sight velocity of the gas and the temperature. This accounts for Lyman-α optical depth due to both neutral hydrogen of planetary origin and ENAs of stellar origin.

The absorption cross-section is given by

$$\sigma_\nu = \frac{\pi e^2}{m_e c} f\Phi(u_{z_t}, T) \tag{2.47}$$

where e and m_e is the charge and mass of the electron, c is the speed of light, $f = 4.1641 \times 10^{-1}$ is the oscillator strength of the transition and Φ is the Voigt line profile (Kramida et al., 2022). The Gaussian part of the Voigt profile has a standard deviation of σ_N, the Lorentzian part has a half-width

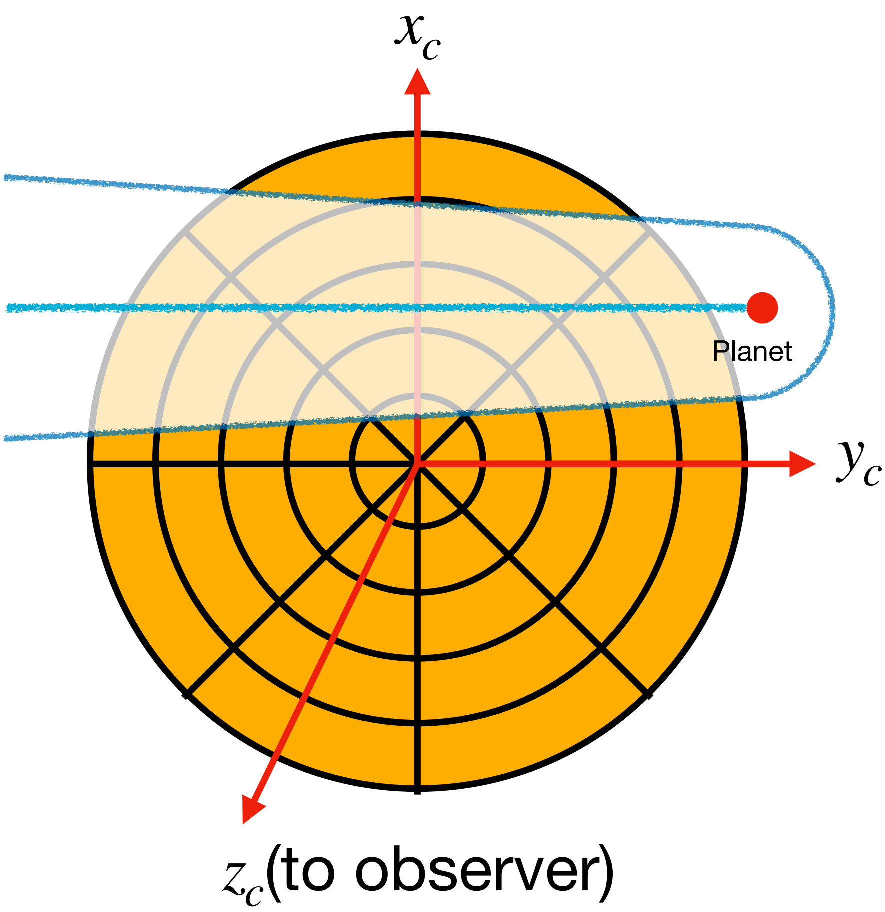

Figure 2.3: A sketch showing the transit of the tail across the discretized stellar surface. The transit depth is calculated by performing ray-tracing through tail on this grid.

at half-maximum of γ, and the line centre has been Doppler shifted to ν. These are given below:

$$\sigma_N = \sqrt{\frac{k_b T}{m_H c^2}}\nu_0, \quad \gamma = \frac{A}{4\pi}, \quad \nu = \nu_0\left(1 - \frac{u_{z_t}}{c}\right) \tag{2.48}$$

where k_b is the Boltzmann constant. Here ν_0 is the rest frequency of Lyman-α and $A = 6.2649\times10^8$ s^{-1} is the Einstein A coefficient of the transition (Kramida et al., 2022).

The obscuration fraction averaged over the stellar disc is:

$$O_\nu = \frac{\iint_D e^{-\tau_\nu(x_t,y_t)} dx_t dy_t}{\pi R_*^2} \tag{2.49}$$

This does not account for spatial variations in the Lyman-α profile across the stellar surface, as seen on the Sun (Gordino et al., 2022). To numerically solve for the obscuration fraction, the integral in Equation 2.46 is calculated by performing a middle Riemann sum using the 1D grid in the z_t-direction.

The integral in Equation 2.49 is calculated by performing a double Riemann sum using the 2D grid over the stellar disc.

2.5 Fitting the transit of GJ 436 b

I use the outflow model to perform a retrieval of the warm Neptune GJ 436 b in a Bayesian framework. I choose this planet because the Lyman-α transit of this planet has been extensively observed with the Hubble Space Telescope (Kulow et al., 2014; Ehrenreich et al., 2015; Lavie et al., 2017; dos Santos et al., 2019). The fixed and free parameters of the model are listed in Table 2.3. Here, I list the values used for the fixed parameters and the prior bounds for the free parameters. In order to reduce the number of free parameters, the temperature of the stellar wind is set to 0.5 MK. I checked that this choice does not affect my conclusions by running models with $T_{\rm sw} = 1$ MK, and found similar results. In the fitting procedure, I convert the angular momentum deficit, h, into the "launch angle" of the outflow, given by θ in Equation 2.45. I do this so that a uniform prior can be put on the launch angle. For all other free parameters, apart from the inclination, I use log uniform priors, as the scale of these parameters is not constrained. The prior bounds enclose realistic parameter bounds as determined from theory or other observations. I use the energy-limited mass loss rate:

$$\dot{M}_{\rm EL} = \eta \frac{\pi F_{\rm XUV} R_P^3}{G M_p} \tag{2.50}$$

with the efficiency $\eta = 1$ to set an upper bound on the planetary mass loss rate. Here, the EUV flux is approximated from the optically thin photoionization rate by assuming all ionizing photons deliver 20 eV (see Murray-Clay et al. (2009)). I note that the appropriate radius over which the planet absorbs EUV flux may be larger than the optical radius, which can enhance this mass loss rate limit. However, this is often balanced out by the real efficiency for escaping planets being significantly less than one. Therefore, it is reasonable to simply use the optical radius.

The posterior is sampled using the Markov chain Monte Carlo (MCMC) ensemble sampler *emcee* (Foreman-Mackey et al., 2013). This is a Python implementation of Goodman & Weare's affine invariant MCMC ensemble sampler (Goodman & Weare, 2010). I calculate the log-likelihood for a

Table 2.3: The values of fixed parameters and the priors for the free parameters used whilst fitting the Lyman-α transit of GJ 436b. U(a, b) denotes a uniform distribution bounded by the parameters a and b. N(a, b) denotes a normal distribution with mean a and standard deviation b.

Parameter	Value/Prior
Fixed	
Planet Mass, M_p (M_J)	0.07
Planet Radius, R_p (R_J)	0.35
Semi-major axis, a_p (AU)	0.029
Stellar Mass, M_* ($M_\odot$)	0.45
Stellar Radius, R_* ($R_\odot$)	0.425
Stellar Wind Temperature, $T_{\rm sw}$ (MK)	0.5
Free	
Log Sound speed (cm s^{-1})	U(5.2, 6.5)
Log Planet mass loss rate (g s^{-1})	U(8, $\dot{M}_{\rm EL}$)
Log Stellar wind velocity (at planet) (cm s^{-1})	U(6.5, 8)
Log Star mass loss rate (g s^{-1})	U(10.3, 13)
Log Optically thin photoionization rate (at planet) (s^{-1})	U(-5.6, -2.6)
Launch Angle (radians)	U($\frac{\pi}{2}$, π)
Inclination (radians)	N(1.51, 0.02)
Log Bulk velocity of ENAs (cm s^{-1})	U(6.4, u_*)
Log Width of turbulent mixing layer	U(-2, -0.4)

parameter set $\mathbf{\Theta}$ by comparing the observed flux $\mathcal{F}_o$ to the modelled flux $\mathcal{F}$ as functions of both time and wavelength within a collection of observed time series spectra as:

$$\ln\mathcal{L}(\mathbf{\Theta}) = -\frac{1}{2}\sum_n \left[\frac{(\mathcal{F}_o - \mathcal{F})^2}{\sigma_n^2} + \ln(2\pi\sigma_n^2)\right] \tag{2.51}$$

The time-series spectra consist of all Lyman-α observations of GJ 436 to date taken with the Hubble Space Telescope's (HST's) Space Telescope Imaging Spectrograph (STIS) configured with the G140M grating. This consists of 26 individual observations obtained between 2010 and 2016 (program PIs Ehrenreich, Green, and France). The spectra are uniformly re-extracted using the calSTIS pipeline, manually identifying the position of the spectral trace on the detector. An extraction ribbon of 11 pixels and background ribbons of 20 pixels at ±20 pixels from the trace location are used to minimize effects from a spatially-variable background systematic known as FUV glow. The observations are divided into subexposures of roughly 500 s each, with minor adjustments to ensure the full use of each exposure.

For comparison to the data, I forward-model the observed Lyman-α spectrum during each subexposure.

I do this by applying the absorption predicted by the model ray tracing to a de-broadened version of the stellar Lyman-α profile as observed at earth reconstructed using the technique described in Wilson et al. (2022). The profile is then broadened by the instrument line spread function and binned to match the wavelength grid of the data. The observed and modelled spectra are then normalized to an identical flux in the range of 90 and 250 km s^{-1}. This accounts for known variability in instrument throughput and stellar variability in which the full spectrum is scaled by a constant. I note that this method cannot take into account variability in which the ratio of flux in the red wing to the blue wing changes. After normalization, I use the predicted spectrum and flux scale of the instrument to estimate the expected number of counts in each wavelength bin, then use this to compute the expected variance due to Poisson statistics. This mitigates problems due to zero-flux, zero-error points in the calSTIS-reduced data and the disproportional influence of low-flux, low-error points on fits and is more appropriate for a Bayesian framework. I use the resulting normalized spectra and estimated errors to compute the data likelihood with Equation 2.51. I comment that there are minor differences in the transit depth in the reduced data and that of previous authors (Lavie et al., 2017) as a result of the different normalization strategy, and possibly different transit baseline.

The MCMC is run for a minimum of 15000 steps with 100 walkers. In order to monitor convergence, I ran two independent chains for each model so that I could calculate the split chains potential scale reduction factor, split-$\hat{R}$ (Gelman et al., 2014). The maximum value across all parameters was 1.02. I also calculated the effective sample size for each of the parameters, which was a minimum of 15. Based on these results, I conclude that the posterior I have calculated from the MCMC is representative of the true posterior.

2.6 Results and Discussion

To explore how including different parts of the outflow affects inferences, I run four models of increasing complexity. In the first, I only include the tail outflow; in the second, I include both the tail and the Hill sphere outflow; in the third, I include the tail outflow and ENAs; and in the fourth, I include all model components (i.e. the tail, Hill sphere outflows, and ENAs). In the models where I do not include the outflow inside the Hill sphere, I only compare to data after the egress of the Hill sphere (> 1.3 hours). In the cases where the outflow inside the Hill sphere is included, I only compare to data after the egress of the planet (> 0.7 hours). The observed transit shows absorption before the ingress of the Hill sphere, and therefore I avoid comparing to data affected by the outflow in front of the Hill sphere of the planet, where the transit depth is underestimated. The retrieved parameters from all four models are consistent, indicating the tail part of the outflow drives my inferences. This is expected for GJ 436 b as the tail dominates the transit duration. I find that ENAs contribute very little to the Lyman-α optical depth. For the retrieved parameters, the mixing region is $\lesssim 3$ percent of the depth of the tail $\sim R_p$, which leads to very small optical depths (< 0.01) at typical ENA densities on the order of the stellar wind density. I verify this by calculating the spectrum for the best-fit model without the contribution of ENAs and find it virtually indistinguishable from the spectrum including ENAs.

We do find a slight inconsistency in retrieved inclinations between the models with and without the inclusion of the Hill sphere. In the cases with the Hill sphere, the inclination has a median of 1.55 radians, whilst in the cases without the Hill sphere, it has a median of 1.52 radians, more in line with observational constraints. I think this discrepancy comes from the fact that cutting the gas off at the Hill sphere underpredicts the extent of the gas in this region, and therefore, the inclination has to change to compensate. However, the fact the rest of the retrieved parameters are the same gives us confidence that most of the information is coming from the tail. As a result, I focus on the fourth model, including the tail, Hill sphere and ENAs from now on.

In Figure 2.4, I present the marginalised posterior distributions for the sound speed, planetary mass loss rate, optically thin photoionization rate, mass loss rate of the star and ram pressure of the stellar wind. The 2D joint posteriors show correlations between the parameters, which help elucidate the key physics governing observations. These correlations are easier to extract in this framework than from only running 3D simulations because this model is significantly less computationally expensive than 3D simulations so is able to more widely sample the possible parameter space. Later in this section, I examine how the retrieved sound speed of the escaping gas, planetary mass loss rate and photoionization rate in the tail, which control the density of neutral hydrogen, are correlated. I also examine how the retrieved planetary mass loss rate and stellar wind ram pressure, which control the

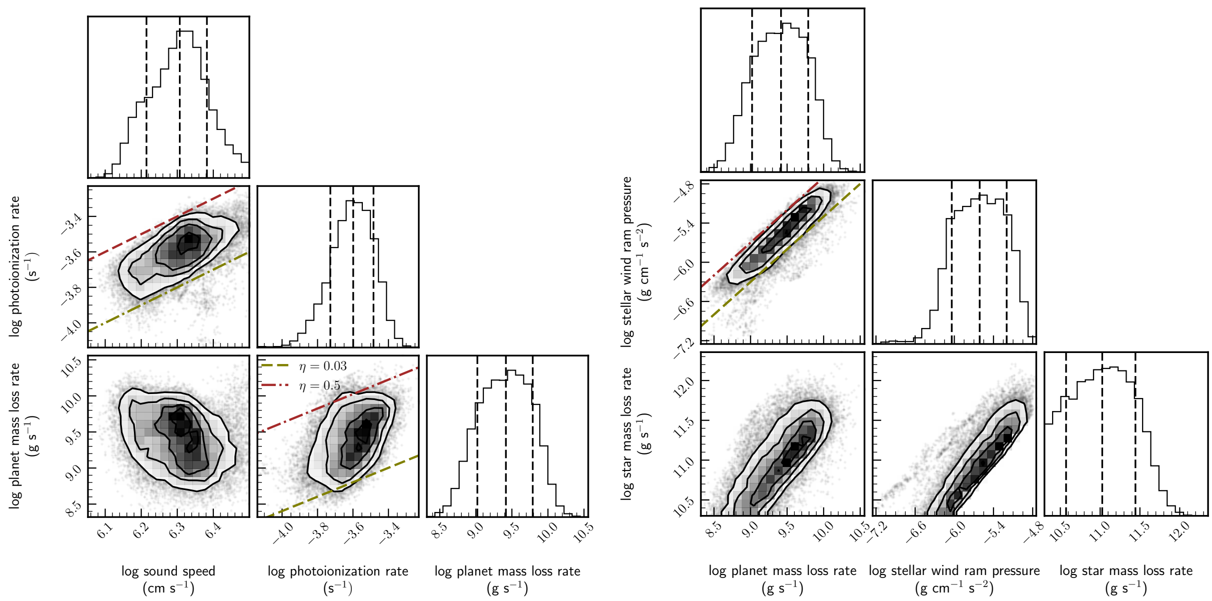

Figure 2.4: Left: Posterior distribution of the sound speed, planet mass loss rate, and photoionization rate for GJ 436 b. On the joint sound speed and photoionization rate posterior, I have plotted lines of constant ratio corresponding to $\frac{c_s}{\Gamma_p} = 10^{9.7-10.1}$ cm. On the joint mass loss rate and photoionization rate posterior, I have plotted lines of constant efficiency from the energy-limited mass loss formula (Equation 3.2). Right: Posterior distribution of the planet mass loss rate, stellar wind ram pressure, stellar mass loss rate. On the joint planet mass loss rate and stellar wind ram pressure posterior, I plot lines of constant ratio corresponding to $\frac{\dot{M}_* u_*}{\dot{M}_p} = 10^{9.1-9.7}$ cm s^{-1}. Although planetary mass loss rate and stellar wind ram pressure cannot be tightly constrained individually, the tight correlation between these parameters means that this ratio is tightly constrained, illustrated by the small spacing of constant-ratio lines bounding the posterior.

radial velocity of the outflow, are correlated. In Figure 2.5, I plot the model transmission spectra at different times in the transit for the maximum a posteriori parameter estimates (i.e. posterior mode). It is clear that the model is a good match for the spectrum, providing evidence that the model accurately represents the planetary outflow. This is further illustrated by Figure 2.6, where I show the transit integrated between -50 and -150 km s^{-1}.

2.6.1 Mass Loss Rate

We find a total hydrogen mass loss rate of $2.6^{+3.5}_{-1.6} \times 10^9$ g s^{-1}. This is similar to the mass loss rate of 2×10^9 g s^{-1} found in the 1D simulations by Schulik & Booth (2023), and 5.5×10^9 g s^{-1} found in 3D hydrodynamics simulations by Villarreal D'Angelo et al. (2021), which were able to reproduce the depth and duration of the transit. Considering the joint mass loss rate and photoionization, it is

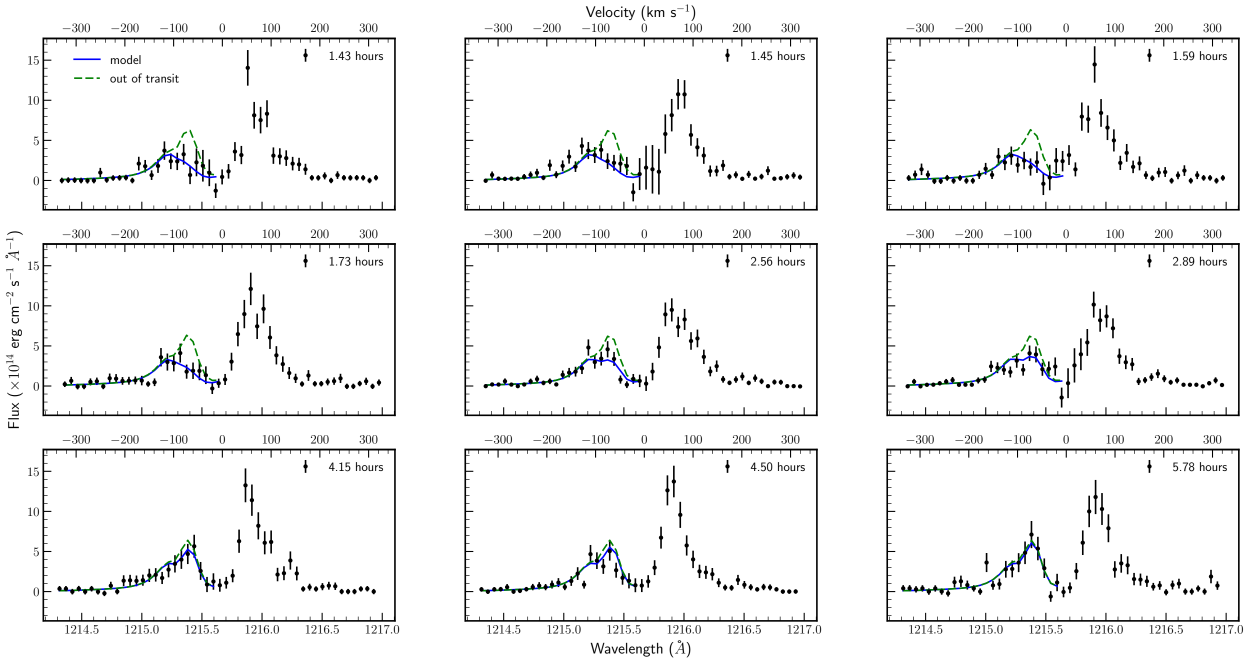

Figure 2.5: Lyman-α transit spectrum of GJ 436 b at different times (relative to optical mid-transit) measured using Hubble Space Telescope (black points) and the model (solid blue) using the MAP estimates from the MCMC sampler. The dashed green line is the out-of-transit model that is used to calculate the transmission spectrum.

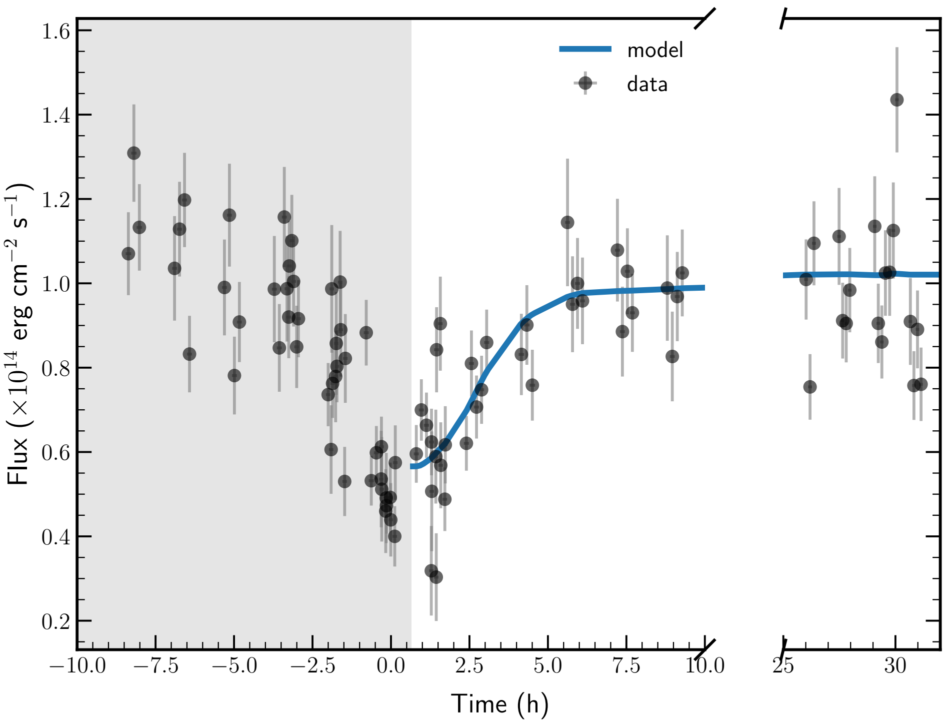

Figure 2.6: Lyman-α transit of GJ 436 b integrated over the blue wing interval of [-150, 50] km s^{-1}. The shaded region is before the egress of the planet, where gas leading the Hill sphere of the planet is transiting the star, which I do not fit with my model.

possible to put constraints on the efficiency of the outflow, η, given in the energy-limited formula (Equation 3.2). On the posterior, I plot lines of constant mass loss efficiency and am able to constrain this to range from 0.03-0.5. This is consistent with simulations of atmospheric escape from GJ 436 b that include both EUV and bolometric heating, finding an efficiency of ~ 0.05 (Schulik & Booth, 2023). More generally, it is consistent with the theoretical estimates for a photoevaporative flow (e.g. Owen & Jackson, 2012; Owen & Alvarez, 2016). I highlight that as a real stellar spectrum has significant flux above 20 eV, these efficiencies are likely underestimated by a factor of a few.

The posterior distribution reveals a positive correlation between the retrieved planetary mass loss rate and the photoionization rate. This indicates that higher EUV fluxes lead to a more ionized outflow, which in turn requires an increased planetary mass loss rate to produce the same transit depth. Notably, this relationship is steeper than the linear energy-limited scaling between high-energy flux and mass loss rate, suggesting that planets receiving higher EUV fluxes actually exhibit lower transit depths. This occurs because the increased ionization in the outflow reduces the neutral hydrogen fraction, outweighing the effect of a higher mass loss rate.

Interestingly, there is a tight constraint on the ratio of the ram pressure of the stellar wind at the planet and the mass loss rate of the planet of $\frac{\dot{M}_* u_*}{\dot{M}_p} = 10^{9.4\pm0.3}$ cm s^{-1}. The reason for this is that this ratio determines the radial acceleration of the tail and, hence the radial velocity and the position of the tail as a function of time. In Figure 2.7, I plot a sample of tail trajectories drawn from the posterior distribution from the retrieval of GJ 436b, coloured by the ratio of the stellar wind ram pressure to the mass loss rate of the planet. This demonstrates the dominant role that this ratio plays in setting the trajectory of the outflow and the sensitivity of the observed transit to stellar wind conditions.

To see the effect that the acceleration of the tail has on the observed spectrum, consider the ratio of observed flux in the (-150,-100) km s^{-1} band and (-100,-50) km s^{-1} band, shown in Figure 2.8. As the tail is accelerated, more flux is absorbed at higher velocities, so the ratio decreases. We note that this ratio also changes as the column density of neutral hydrogen changes, and therefore, to extract the effect of the acceleration of the tail, I have also shown how this ratio evolves if the gas in the tail were fully neutral.

The acceleration of the tail (Equation 2.7) is not exactly proportional to the ram pressure of the stellar

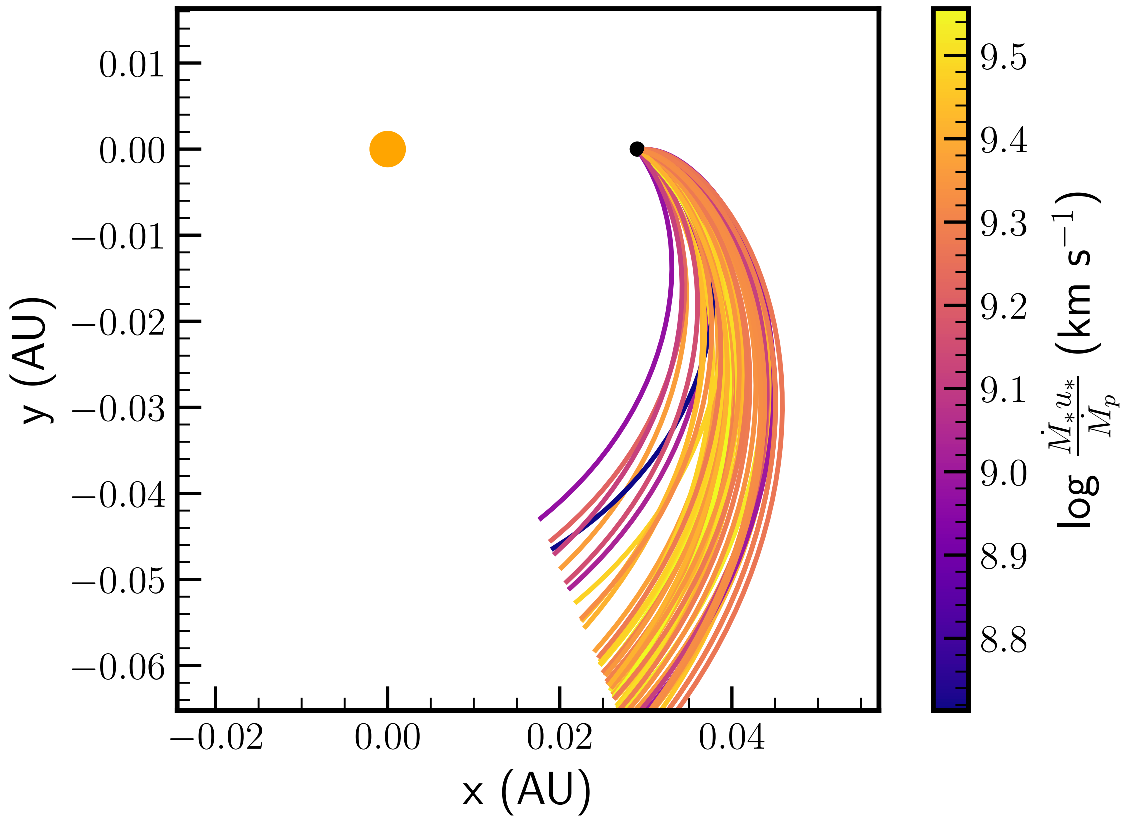

Figure 2.7: A sample of tail trajectories drawn from the posterior distribution from the retrieval of GJ 436 b coloured by the ratio of stellar wind ram pressure to planetary mass loss rate. Whilst I note that the trajectory of the tail weakly depends factors such as the launch angle and outflow sound speed, the ratio of the stellar wind pressure to planetary mass loss rate controls the acceleration of the tail, and therefore is primarily responsible for setting the trajectory of the tail.

wind but depends on the difference between the radial velocity of the tail and the stellar wind. The maximum velocity to which the tail can be accelerated is the stellar wind velocity. If the tail reaches this terminal velocity whilst still attenuating Lyman-α photons, then very strong constraints can be placed on the stellar wind velocity. In the case of GJ 436 b, the tail is still accelerating, and therefore, it is possible only to put a lower limit of 300 km s^{-1} on the stellar wind velocity at the planet.

I emphasize that I do not dismiss the case where the stellar wind velocity is very high (> 800 km s^{-1}), and the mass loss rate is low as GJ 436 b has a polar orbit (Bourrier et al., 2022). For the Sun, the polar wind is significantly faster and less dense than the equatorial wind, and therefore, it is possible that this is the case for GJ 436 as well.

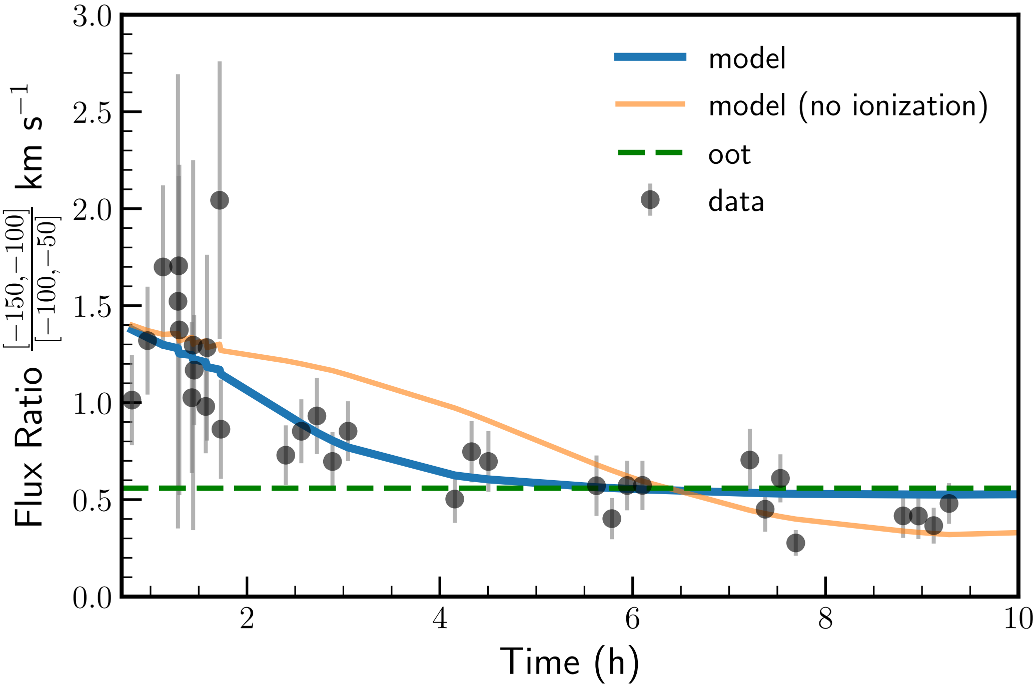

Figure 2.8: The observed flux ratio between (-150, -100) and (-100, -50) km s^{-1} as a function of time after the transit (black dots). The blue line is the best-fit model, the orange line is the best-fit model, setting the photoionization rate to zero, and the dashed green line is the out-of-transit ratio. There is a smooth decrease in this ratio from $\sim$ 1 hour to 5 hours as the tail is accelerated to higher velocities and becomes more ionized, absorbing more photons in the (-150, -100) km s^{-1} band compared to the (-100, -50) km s^{-1} band. The model with the ionization rate set to zero indicates the length of the transit required in order to unambiguously detect the acceleration of the tail (as ionization also changes the flux ratio).

2.6.2 Sound Speed of the Outflow

The 2σ lower bound for the retrieved sound speed is 13 km s^{-1}, corresponding to a temperature of $\sim$ 10, 000 K for a fully ionized purely hydrogen gas, which is consistent with a photoevaporative outflow. The bulk of the posterior encompasses higher sound speeds, with a maximum a posteriori (MAP) estimate of 20.5 km s^{-1}, which corresponds to outflow temperature $\sim$ 40,000 K. This is higher than expected for photoevaporative outflows which usually thermostat at temperatures $\sim$ 10,000 K, due to the strong radiative cooling of hydrogen above those temperatures.

It is possible that another physical mechanism is accelerating the outflow to high velocities by the time it reaches the Hill sphere, raising the apparent sound speed. This interpretation is compatible with the results of Bourrier et al. (2016), which used a collisionless outflow model of the exosphere and required outflow velocities of $\sim 50-60$ km s^{-1} to fit the data. A possible mechanism to produce these high velocities is via the dissipation of MHD waves in the upper atmosphere (e.g Tanaka et al., 2014); however, consistent multi-dimensional models are needed to prove that this is a viable mechanism to drive high-velocity outflows.

Another possible reason for the high retrieved sound speed is if the model is underestimating the production of ENAs, which provide a source of high-velocity hydrogen atoms. Less ENAs can be compensated for by increasing the number of high-velocity hydrogen atoms of planetary origin, which can be achieved by increasing the sound speed of the outflow. The single-fluid model for charge exchange production that I use predicts a significantly lower contribution to ENAs compared to particle-based (e.g. Bourrier et al., 2016) or multi-fluid hydrodynamic simulations (e.g. Khodachenko et al., 2019), which are capable of reproducing large mid-transit depths with Lyman-α absorption from ENAs.

To evaluate the validity of the single-fluid model used for producing ENAs, I verify that the conditions required for a single-fluid framework are satisfied. In the best-fit model, the density of protons and hydrogen atoms at the ionopause (located at $\sim 7.5R_p - 1.8\times10^{10}$ cm), is $\sim 10^5$ cm^{-3}. At 10^6 K, the cross section for proton-hydrogen collisions is $\sim 6\times10^{-15}$ cm^2 (Schultz et al., 2008) and the cross section for proton-proton collisions is $\sim 10^{-16}$ cm^2 (Schunk & Nagy, 1980). Therefore, the mean free path for stellar wind protons in the planetary outflow is $\sim 10^9$ cm. This is 18 times smaller than the ionopause radius, therefore it is valid to use the single-fluid framework. I comment that in different parts of the parameter space (for example, at lower planetary wind densities), this condition may not hold, therefore particle-based or multi-fluid methods are required to properly model the production of ENAs.

One potential way to break the degeneracy between the contribution of the planetary outflow and ENAs is to consider the distinction between the velocity-resolved transit from each of these factors. If the planetary wind is responsible for the majority of Lyman-α optical depth, then the velocity of peak absorption should increase over the duration of the transit as the tail is accelerated away from the star. ENAs, which are of stellar origin, will have a different velocity distribution and therefore the observed velocity evolution of the transit may differ from that produced by hydrogen atoms of planetary origin.

To determine if this is the case, more work is needed investigating the velocity structure of generated ENAs and how they imprint upon velocity-resolved transits as a function of planetary and stellar parameters.

We note that in the case of GJ 436 b, one cannot definitively tell that the absorbing material is being accelerated as a function of time (model independently) because the gas becomes ionized too quickly for the velocity of peak absorption to change dramatically (see Figure 2.8). However, for planets with lower ionization rates and, therefore, longer tails (e.g. K2-18b, dos Santos et al. 2020) or when the gas in the tail is in ionization-recombination equilibrium, it may be possible to observe the acceleration of the gas in the lightcurve.

Limitations and Future Improvements

Since the model does not take into account gas in front of the Hill sphere of the planet, it is not able to account for the information about the outflow in the pre-transit data. The challenge with modelling the outflow leading the planet is that it is unstable, resulting in the variable occultation of the star (e.g., McCann et al., 2019) as seen in the case of AU Mic b (Rockcliffe et al., 2023). The reason for this instability is that the Coriolis force and the stellar wind pressure both act in the same direction; therefore, the outflow cannot be in generalised geostrophic balance and reach a stable density structure. This problem is only pertinent when the planetary wind and the stellar wind have similar strengths. However, Lyman-α observations, which show an extended outflow leading the planet (e.g., Rockcliffe et al., 2023) make understanding this case important. I leave modelling of the outflow leading the planet to future work. In the case of GJ 436 b, where there is minimal pre-transit absorption, the stellar wind is most likely strong enough to stop a leading outflow. In this case, the time of ingress provides an approximate location for the boundary between the stellar and planetary wind, which can be used to infer their relative pressures at this location.

Our model does not include the effect of magnetic fields, as I use purely hydrodynamic simulations as the basis for my work. Both the planetary magnetic field and the stellar wind magnetic field can affect the geometry of the outflow (e.g., Carolan et al., 2021b). However, it is not yet clear whether close-in exoplanets host strong magnetic fields as I will discuss in Chapter 3 or whether the stellar wind magnetic field plays an important role in the interaction with the planetary outflow as the ram pressure of the stellar wind dominates over the magnetic pressure outside the Alfvén surface.

Similarly, I do not include the effects of radiation pressure. Like the stellar wind, this can impart momentum to the planetary outflow, accelerating it radially. For GJ 436 b, radiation pressure is unlikely to be important (e.g., Khodachenko et al., 2019). However, this may not be the case for all systems. In the future, I will extend the model to include a term accounting for this force. Another possible improvement to this model would be to include a more realistic stellar wind accounting for the orbital velocity of the planet and variations along the orbit.

We also imposed a circular orbit on the planet. Since highly irradiated planets are close to their host star, they are generally assumed to have undergone orbital circularization. However, deviations from a circular orbit can cause a line of sight velocity shift of $v_k e \cos\omega$, where e is the eccentricity of the planet and ω is the argument of periastron. In the case of GJ 436 b, the eccentricity and argument of periastron are 0.156 and 325.8 degrees, respectively (Bourrier et al., 2022), which equates to a line of sight velocity shift of ~ -15 km s^{-1} at mid-transit. This is small compared to the velocities probed by Lyman-α transits and, therefore, cannot be fully responsible for the high radial velocities observed. However, it may partially be responsible for the higher-than-expected sound speed retrieved. In the future, it may be worthwhile folding constraints on the planetary orbital dynamics into the model.

2.7 Summary

I have created a model of the interaction of a planetary outflow with the circumstellar environment, which can be used to perform synthetic Lyman-α transits. I demonstrate that this model is able to reproduce the geometry of outflows produced by 3D hydrodynamics simulations. Furthermore, I illustrate the usage of this model to perform the first retrieval of atmospheric escape properties using velocity-resolved Lyman-α observations.

For GJ 436 b, I am able to constrain the sound speed of the escaping gas to be $\gtrsim$ 10 km s^{-1}, indicating that core-powered mass loss can be ruled out as the mechanism of escape for this planet.

This is consistent with the predictions from the combined photoevaporation and core-powered mass-loss model of Owen & Schlichting (2024). Although the retrieved planetary mass loss rate has wide bounds, I find that the ratio of planetary mass loss rate to stellar wind ram pressure is tightly constrained. Independent constraints on the space environment around this planet (e.g Bellotti et al., 2023) would allow stronger constraints on the planetary mass loss rate. Equally, Lyman-α transits are an effective way to measure the stellar winds of stars.

The usefulness of the simple model is that it can efficiently explore the large parameter space to find solutions that match the data well. In doing so, it is possible to put constraints on parameters and find correlations between parameters, which can both inform whether current models can fit the observations and guide future 3D simulations. I do caution that making a simplified model requires sacrificing some accuracy as compared to 3D simulations, and therefore, further simulations are needed to confirm the conclusions drawn from this study. At the same time, although much progress has been made with large-scale simulations, I also note the physics included, and hence, the validity to describe Lyman-α transits is still debated. Therefore, simple models that can provide tests of the physics of Lyman-α transits on both individual systems and on a population-wide basis are essential to progress in this field.

Chapter 3

Constraining the Magnetic Fields of Close-in Exoplanets

In this chapter, I present a method to constrain the magnetic fields of exoplanets from direct observations of atmospheric escape using the helium 10830 Å line. Strong planetary magnetic fields will influence both the geometry and mass loss rate of photoevaporative outflows. Consequently, the presence/absence of planetary magnetic fields will be imprinted on direct observations of atmospheric escape and the evolutionary history of planet.

Currently, there are no confirmed measurements of the magnetic field strength of an exoplanet (Brain et al., 2024). Furthermore, there is no accepted *a priori* theoretical framework for predicting exoplanetary magnetic fields other than scaling relationships (e.g., Grießmeier et al., 2004; Christensen et al., 2009). It is highly uncertain how valid these are in the exoplanet regime. Therefore, it is difficult to assess whether exoplanetary magnetic fields are the required strength to control their outflows.

Owen & Adams (2019) studied the effects of magnetic fields on the location of the radius valley. They noted that there is an degeneracy between core density and mass loss rates in setting the location of the radius valley. As magnetic fields suppress mass loss rates, if close-in small planets host strong magnetic fields, then they have lower density cores than implied by evolutionary models that do not account the effect of magnetic fields on mass loss (e.g., Owen & Wu, 2017; Rogers & Owen, 2021).

The global structure of an exoplanet's escaping atmosphere depends on various planetary and stellar parameters, such as the mass loss rate and temperature of the planetary wind, the mass loss rate and temperature of the stellar wind, stellar ionizing flux, and the stellar and planetary magnetic fields, which are generally unknown/poorly constrained (e.g. Vid, 2023). Given that Lyman-α transits are dominated by absorption far from the planet ($\gtrsim 10\times$ the planet's radius), the effects of these parameters are often degenerate, so they cannot be strongly constrained (e.g Owen et al., 2023; Schreyer et al., 2024). This makes it difficult to extract the impact of a planetary magnetic field, which dominates close to the planet ($\lesssim 3\times$ the planet's radius).

In contrast, the helium 10830 Å line provides a unique opportunity to measure the magnetic field strengths of exoplanets. The low number density of metastable helium means that the 10830 Å line forms near the planet (as opposed to Lyman-α, Oklopčić & Hirata 2018). Furthermore, the 10830 Å line is in the near-infrared and can, therefore, be observed from the ground at high spectral resolution. These unique factors of precise kinematic measurements close to the planet mean that helium primarily traces the structure and kinematics of the outflowing gas exactly where planetary magnetic fields are their most controlling.

3.1 The Effect of Magnetic Fields on Photoevaporation

As discussed, the planetary outflow is sensitive to both planet properties and the stellar environment. Following Owen & Adams (2014), one can coarsely partition the outflow into regimes based on the relative strength of the stellar magnetic field, stellar wind ram pressure, planetary magnetic field, and planetary wind ram pressure. In this work, I consider regimes where either the ram pressure of the planetary wind or the planetary magnetic field pressure dominates the stellar components close to the planetary surface, where most of the helium absorption occurs. I can estimate whether the outflow is magnetically controlled by considering the dimensionless quantity Λ, which is the ratio of the ram pressure of the wind to the magnetic pressure of the planet. For a planet with a dipolar magnetic field, this ratio is equal to:

$$\Lambda_{\mathrm{p}} = \frac{2\dot{M}_p u r^4}{B_0^2 R_P^6} \tag{3.1}$$

where $\dot{M}_p$ is the outflow rate, u is the velocity of the outflow, B_0 is the surface magnetic field strength of the planet, R_P is the radius of the body and r is the distance to the centre of the body. When $\Lambda_{\mathrm{p}} \ll 1$, the flow is magnetically controlled, and the outflowing gas is forced to follow magnetic field lines. When $\Lambda_{\mathrm{p}} \gg 1$, the outflow will drag magnetic field lines and should follow a flow structure similar to a pure hydrodynamic outflow. Using an "energy-limited" outflow (e.g. Baraffe et al., 2004) where:

$$\dot{M}_p = \eta \frac{\pi F_{\mathrm{XUV}} R_P^3}{4GM} \tag{3.2}$$

the threshold magnetic field is estimated by the condition that the magnetic pressure and ram pressure are equal (i.e $\Lambda_p = 1$). For fiducial parameters appropriate for a typical hot Jupiters, this is:

$$\begin{aligned} B \approx 0.015 &\left(\frac{\eta}{0.1}\right)^{\frac{1}{2}} \left(\frac{F_{\mathrm{XUV}}}{10^4 \text{ erg s}^{-1}}\right)^{\frac{1}{2}} \left(\frac{u}{10 \text{ km s}^{-1}}\right)^{\frac{1}{2}} \left(\frac{M_p}{M_J}\right)^{-\frac{1}{2}} \\ &\times \left(\frac{R_p}{R_J}\right)^{\frac{1}{2}} \left(\frac{r}{R_p}\right)^2 \text{ Gauss} \end{aligned} \tag{3.3}$$

3.1.1 Post-processing existing simulations

To assess whether "hydrodynamic" and "magnetically controlled" outflows produce blue- and red-shifted transit spectra, respectively, it is necessary to compare the synthetic transit spectra produced from simulations. There are no 3D radiation-hydrodynamics photoevaporation simulations that include helium and magnetic fields. Given the complexity of post-processing simulations (as detailed in Section 3.1.2), which would be difficult in 3D, as a first step, I choose to use existing 2D photoevaporation simulations of a hot Jupiter presented in Owen & Adams (2014). These radiation-hydrodynamic simulations did and did not include magnetic fields for the same setup and are ideal for our experiment.

The original simulations were performed on a spherical polar grid (r, θ), which can be converted to Cartesian coordinates (x, z), where the x axis points along the line joining the star and the planet and the z axis is parallel to the planet's orbital angular momentum axis. A sketch of the simulation grid is shown in Figure 3.1. Atmospheric escape is a 3D process and, therefore, several assumptions need to be made in order to be able to perform sensible 2D simulations. Firstly, the planet needs to be tidally locked to have a constant day and night side. At the same time, rotational effects are ignored. Inside the Hill sphere, these effects are small (Murray-Clay et al., 2009) and can be ignored; however, they are important in shaping the flow on the largest scales (e.g, McCann et al., 2019). Since absorption by helium generally comes from close to the planet, this approximation is reasonable.

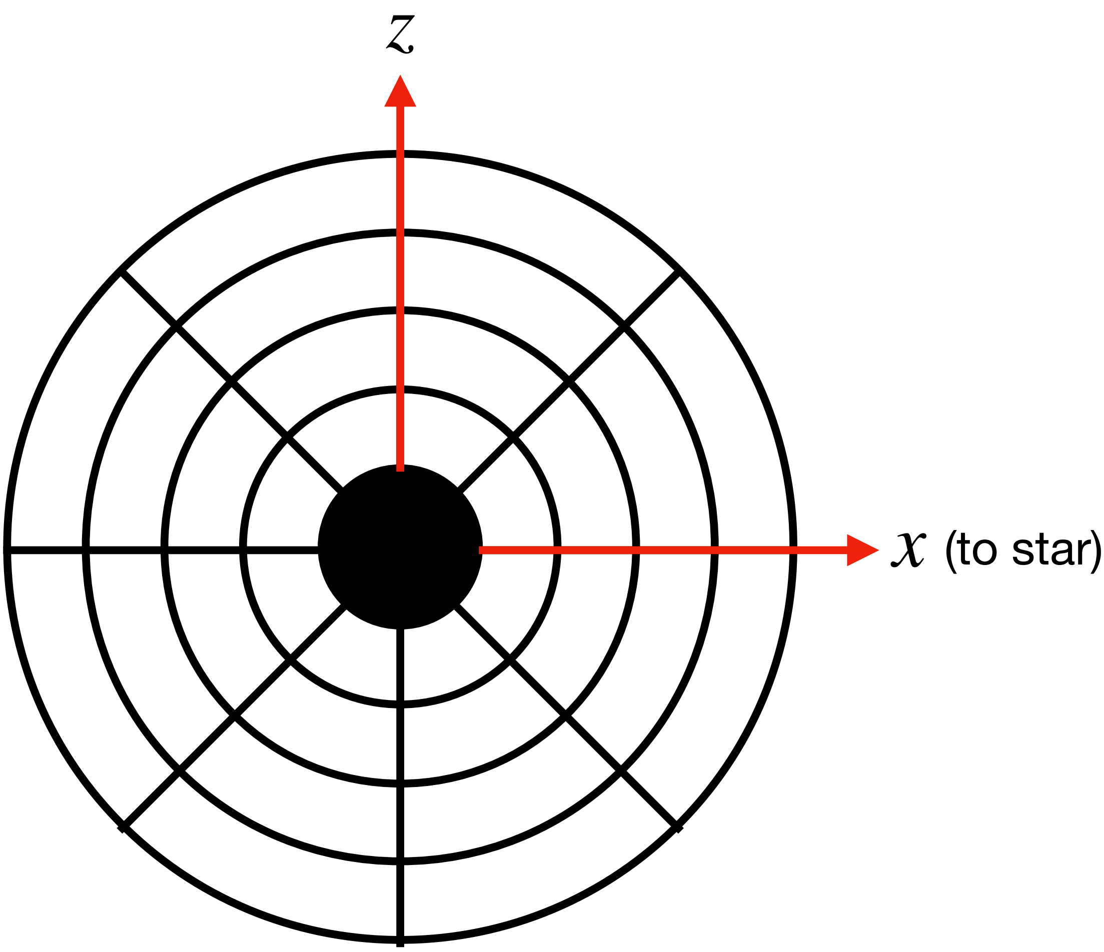

Figure 3.1: The grid Owen & Adams (2014) used to perform the hydrodynamic photoevaporation simulations. The planet is tidally locked therefore, inside the Hill sphere, where the effects of the coriolis forces is small approximation that the coriolis force is small (Murray-Clay et al., 2009), the outflow is rotationally symmetric about the x-axis. Therefore these simulations can approximately represent the full 3D outflow. For the MHD simulations, in which the planet has a dipolar magnetic field with magnetic moment in the z-direction, the symmetry breaks down. Therefore, the simulation considered a thin slice in the $x - z$ plane of the full 3D domain.

To analyse the case where the ram pressure of the planetary outflow dominates over the magnetic field of the planet ($\Lambda_\mathrm{p} > 1$), I use a purely hydrodynamic simulation of the outflow. In the opposite case, where the magnetic pressure dominates over the ram pressure of the planetary outflow ($\Lambda_\mathrm{p} < 1$), I use MHD simulations of the outflow. In these simulations, the planet has a dipolar magnetic field. The planetary dipole was chosen to be parallel to the orbital angular momentum vector of the planet. There are currently no constraints on the geometry of the magnetic field of exoplanets. However, since these planets are very close to their host stars, they are often assumed to be tidally locked. Thus, as a starting point, it is sensible to guess that any dynamo-generated magnetic field may be similar to Jupiter's or Saturn's and (almost) points along the rotation axis.

In the hydrodynamic case, the outflow of the planet is rotationally symmetric around the x-axis; therefore, the full 3D outflow structure is obtained by rotating the 2D structure obtained in the simulations around the x-axis. However, when the planet has a dipolar magnetic field, with a magnetic moment in the $\hat{z}$ direction, the outflow is no longer rotationally invariant around the x-axis (because this rotation changes the direction of the dipole moment). Therefore, the simulation considered a thin slice of the domain in the $x - z$ plane. This required each cell to locally have the property that $\partial_\phi = 0$. Since the magnetic field suppresses the azimuthal flow, this approximation is realistic. Since the magnetic field predominately governs the outflow geometry, the flow structure on the day side is expected to be similar as the planet is rotated around the dipole axis. On the night side, the outflow is suppressed because heat is not efficiently transported across magnetic field lines. As a result, only the day side of the atmosphere was simulated (see Section 5.1 of Owen & Adams 2014 or Trammell et al. 2014).

In some of the simulations, an additional component corresponding to the stellar magnetic field was added. This contribution is modelled as a constant field that points along the pole of the planet:

$$B_* = \beta_* B_p \hat{z} \tag{3.4}$$

where β_* controls the relative strength of the stellar and planetary magnetic fields.

3.1.2 Addition of Helium

The lifetime of the helium metastable triplet level in the outflow is determined by the rates of collisional, radiative, and photoionization processes that depopulate it. As radiative transitions into the ground state are highly suppressed (Drake, 1971), depopulation of this state is dominated by transitions due to collisions and photoionization (e.g., Oklopčić & Hirata, 2018; Oklopčić, 2019). In the outflow, the lifetime of the metastable state may be comparable to the flow timescale (see Figure 4 of Oklopčić 2019). Thus, the helium metastable level is often *not* in local statistical equilibrium. This means traditional post-processing techniques of simply using the local gas properties to compute absorption cross-sections are inappropriate. Therefore, I must compute the level populations by solving the time-dependent radiative transfer equations for gas parcels moving in the outflow.

I assume that the gas is composed of solar abundances of hydrogen and helium; however, I note that the mass fraction of helium in the outflow can be adjusted depending on how efficiently helium is expected to be dragged in the predominantly hydrogen flow (e.g. Malsky & Rogers, 2020). Helium is not expected to contribute to the cooling of the gas, and therefore the predominant way that it affects the outflow is by raising its mean molecular weight. For a solar abundance of helium, the sound speed of the gas can be modified by about $\sim 25\%$. Ultimately, though, adding helium should not have a large effect on the geometry of the outflow. Therefore, it is reasonable to consider the pure flow structure of the pure hydrogen outflow simulated by Owen & Adams (2014) as representative of a hydrogen-helium outflow. Similarly, the distribution of helium ions and atoms in each electronic state has little impact on the outflow structure.

3.2 Methods

3.2.1 Helium Distribution in the Outflow

The first task is to calculate the distribution of helium atoms in the outflow. I track the fraction of helium in the neutral singlet and triplet states along streamlines in the outflow. I only track the number of neutral helium atoms in the ground state 1^1S and metastable 2^3S state since excited states quickly radiatively decay to one of these two states with a matching singlet/triplet configuration. The problem has two parts: (i) determining streamlines in the flow and (ii) calculating the fraction of helium in the triplet state along these streamlines.

In the case of the pure hydrodynamic flow, I solve for the 2D position of a streamline as a function of length, l, down the streamline using equations:

$$\frac{dr}{dl} = \frac{u_r}{u} \tag{3.5}$$

$$\frac{d\theta}{dl} = \frac{u_\theta}{ru} \tag{3.6}$$

I then derive the steady state distribution of helium atoms along streamlines using Equations 3.7 and 3.8, which account for the major transitions in and out of the singlet and triplet states of helium (Oklopčić & Hirata, 2018).

$$\begin{aligned} u\frac{df_1}{dl} = & (1 - f_1 - f_3)n_e\alpha_1 + f_3A_{31} + f_3q_{31a}n_e \\ & + f_3q_{31b}n_e + f_3Q_{31}n_{HI} - f_1\phi_1e^{-\tau_1} - f_1q_{13}n_e \end{aligned} \tag{3.7}$$

$$\begin{aligned} u\frac{df_3}{dl} = & (1 - f_1 - f_3)n_e\alpha_3 - f_3A_{31} - f_3q_{31a}n_e \\ & - f_3q_{31b}n_e - f_3Q_{31}n_{HI} - f_3\phi_3e^{-\tau_3} + f_1q_{13}n_e \end{aligned} \tag{3.8}$$

f_1 and f_3 are the singlet and triplet fractions of neutral helium, respectively. n_e and n_{HI} are the number density of electrons and hydrogen atoms. ϕ_1 and ϕ_3 are the photoionization rate for the singlet and triplet states, respectively. The photoionisation rate for the singlet and triplet states is approximated by the photoionisation rate when all the photo-ionizing flux is concentrated at a single photon energy. This is taken to be 24.6 eV for the singlet state and 4.8 eV for the triplet state.

$$\phi_1 = \int_{24.6\mathrm{eV}}^{\infty} \frac{F_\nu}{h\nu}\sigma_1(\nu)d\nu \approx \frac{F_{\overline{\nu}}}{h\overline{\nu}}\sigma_1(\overline{\nu}) \tag{3.9}$$

$$\phi_3 = \int_{4.8\mathrm{eV}}^{13.6\mathrm{eV}} \frac{F_\nu}{h\nu}\sigma_3(\nu)d\nu \approx \frac{F_{\overline{\nu}}}{h\overline{\nu}}\sigma_3(\overline{\nu}) \tag{3.10}$$

F_ν is the received flux at frequency ν and $\sigma_1(\nu), \sigma_3(\nu)$ are the photoionisation cross sections of the singlet and triplet states respectively. All barred quantities are evaluated at the specific photon frequency detailed above.

Based on the spectral energy distribution for late K stars from the MUSCLES survey (France et al., 2016; Loyd et al., 2016; Youngblood et al., 2016), I estimate the total singlet ionising flux to be 0.2 of the hydrogen ionizing flux and the total triplet ionising flux to be about the same as the hydrogen ionizing flux. As the simulations were run at high UV fluxes $\sim 10^6$ erg cm^{-2} s^{-1}, I set $F_{\overline{\nu}} = 2 \times 10^5$ and 10^6 erg cm^{-2} s^{-1} for the singlet and triplet states respectively. I vary these fluxes by an order of magnitude in both directions and found that it did not qualitatively affect the results. σ_i is the photoionization cross-section of the state. The photoionisation cross section for these photons are 5.48×10^{-18} cm^2 (Hummer & Storey, 1998) and 7.82×10^{-18} cm^2 (Brown, 1971) respectively. In this work, I set both $\tau_1 = 0$ and $\tau_3 = 0$. Since hydrogen also absorbs 24.4 eV radiation, I expect the $\tau = 1$ surface to 24.4eV photons to be above the $\tau = 1$ surface to 4.8eV photons (and close to the hydrogen ionization front in the simulation). Since the main pathway to populate the triplet state is by photoionization of the singlet state and then recombination into the triplet state, I expect that this will underestimate the triplet fraction below the $\tau = 1$ surface to 24.4eV. However, since the hydrogen ionization front is deep in the atmosphere of the planet (in these simulations, it is $\sim 1.03R_{\mathrm{p}}$), the gas below this surface contributes minimally to the overall transit signal.

The recombination and collisional excitation/de-excitation coefficients depend on the temperature of the gas. As the simulations were run for high UV fluxes ($\gtrsim 10^6$ erg cm^{-2} s^{-1}), the gas is in the radiative-recombination regime (Murray-Clay et al., 2009) and therefore thermostats to $\sim 10^4$ K above the ionization front. As a result, I take all coefficients at 10^4 K. $\alpha_1 = 2.16 \times 10^{-13}$ cm^3 s^{-1} &

$\alpha_3 = 2.25 \times 10^{-13}$ cm^3 s^{-1} are the Case A recombination coefficients for the singlet and triplet state respectively (Osterbrock & Ferland, 2006). The electron density (n_e) is calculated in the Owen & Adams (2014) simulations, which only accounted for electrons produced by the ionisation of hydrogen atoms since this is the dominant source. $A_{31} = 1.272 \times 10^{-4}$ s^{-1} is the radiative transition rate between the metastable triplet state and the ground singlet state (Drake, 1971). The transitions between the triplet and singlet states due to collisions with electrons are denoted by the temperature dependent coefficients:

$$q_{ij} = 2.1 \times 10^{-8} \sqrt{\frac{13.6 \text{ eV}}{kT}} \exp\left(-\frac{E_{ij}}{kT}\right) \frac{\Upsilon_{ij}}{w_i} \text{ cm}^3 \text{s}^{-1} \tag{3.11}$$

where E_{ij} is the energy difference between the states from Martin (1973), w_i is the statistical weight of the state and Υ_{ij} is the effective collision strength from Bray et al. (2000). At 10^4 K, the two transitions from the metastable state to singlet levels are given by $q_{31a} = 2.7 \times 10^{-8}$ cm^3 s^{-1} and $q_{31b} = 5.2 \times 10^{-9}$ cm^3 s^{-1}. The transition from the ground singlet state to the metastable state is given by $q_{13} = 5.7 \times 10^{-19}$ cm^3 s^{-1}. Finally, transitions out of the metastable state due to collisions with hydrogen atoms via associative ionisation and Penning ionisation have a combined rate of $Q_{31} \sim 5 \times 10^{-10}$ cm^3 s^{-1} (Roberge & Dalgarno, 1982).

Equations 3.5-3.8 form a set of coupled first-order differential equations. The streamlines are initialised at a constant radius 1.02 R$_p$ with an initial singlet and triplet fraction that is in equilibrium at 500 K with $\phi_1 = \phi_3 = 0$. I solve these differential equations numerically using the implementation of the LSODA method (Petzold, 1983) provided in the *scipy* library (Virtanen et al., 2020). For numerical stability, I solve Equations 3.7 and 3.8 as function of $\log(l)$. The absolute and relative tolerances used are 1×10^{-13} and 1×10^{-10}, respectively and the maximum step size chosen is 1×10^{-3}. All gas properties required to solve these equations (e.g., density, velocity etc.) were interpolated from the original simulations using bivariate spline interpolation over the polar grid. To calculate the metastable helium fraction at any point in the outflow, I interpolate the values for fifty streamlines, linearly spaced in angle, originating on the planet's day side. Testing indicates this is sufficient to calculate the transmission spectrum accurately. Figure 3.2 shows how streamlines originating on the planet's day side wrap around to the night side.

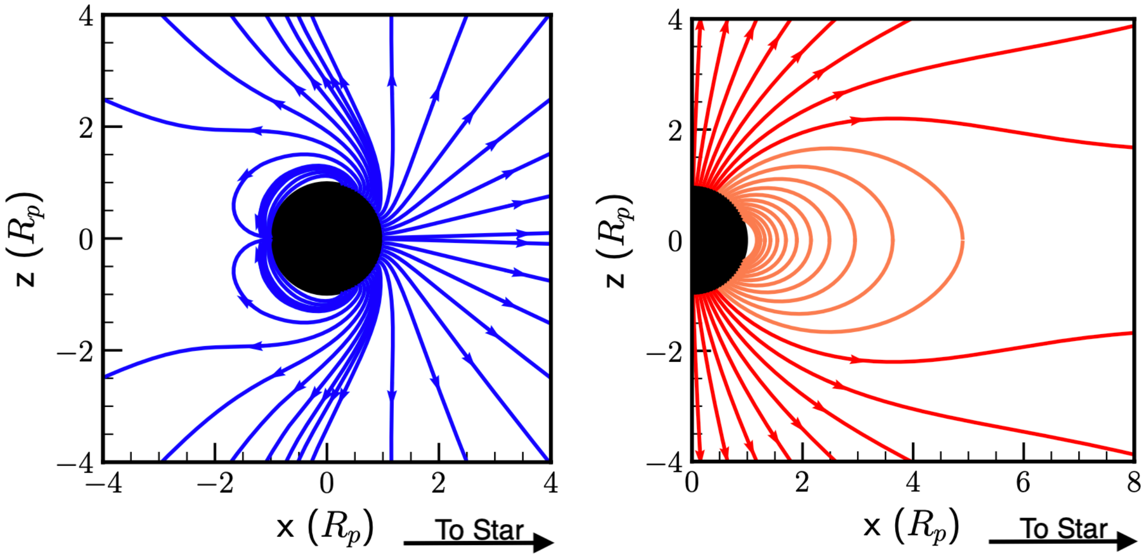

Figure 3.2: Left: Streamlines of the outflow for the case of a planet without a magnetic field. The star is located to the right of the planet along the line $z = 0$. The planet is shown by a black circle centred on the origin. The orientation is the same for all subsequent 2D plots. Due to anisotropic heating, the day side is much hotter than the night side. The resulting pressure gradients cause the outflow to wrap around the planet, creating gas travelling towards an observer in transit in the transmission region. Right: Magnetic field lines for a planet with a surface magnetic field strength of 3 Gauss. Orange lines are closed field lines where the magnetic field is strong enough to confine the flow. The red lines are open magnetic field lines, which also are gas streamlines. The direction of the arrows shows the direction of the outflow. In this case, the magnetic field prevents the day-to-night side outflow and causes the gas to move away from the observer in transit in the transmission region.

In the MHD case, it is necessary to consider both the field near the poles where the magnetic field lines are opened by the outflow and a region centred on the equator where magnetic pressure dominates over thermal pressure so that the field lines are closed. Since the fluid is required to follow magnetic field lines (and magnetic field lines are dragged along by the fluid), the streamlines of the gas in the open region can be determined by tracing magnetic field lines. These are calculated analogously to Equations 3.5 and 3.6 replacing velocity with magnetic field:

$$\frac{dr}{dl} = \frac{B_r}{B} \tag{3.12}$$

$$\frac{d\theta}{dl} = \frac{B_\theta}{rB} \tag{3.13}$$

where B_r and B_θ are the radial and angular components of the magnetic field, respectively. Figure 3.2 shows the magnetic field lines for a fiducial planetary magnetic field strength of 3 Gauss. I use this value of the planetary magnetic field to illustrate the magnetically controlled case throughout the rest of the chapter.

In the regions where the streamlines are open, I solve the steady state distribution of helium atoms using Equations 3.7 and 3.8 as in the hydrodynamic case. In the regions in which they are closed, the gas is approximately in magneto-hydrostatic equilibrium, and as a result, the helium-level populations are in statistical equilibrium. Therefore I solve for the distribution of helium atoms using Equations 3.7 and 3.8 by setting the advection term (the left-hand side) to zero. The method used to solve these equations numerically is the same as the hydrodynamic one, with the addition of a step to check whether the field line is open or closed to decide to solve the non-equilibrium or equilibrium equation for the distribution of helium atoms.

In Figure 3.3, I show the number density profiles of helium in the triplet state for the hydrodynamic and magnetically controlled outflow.

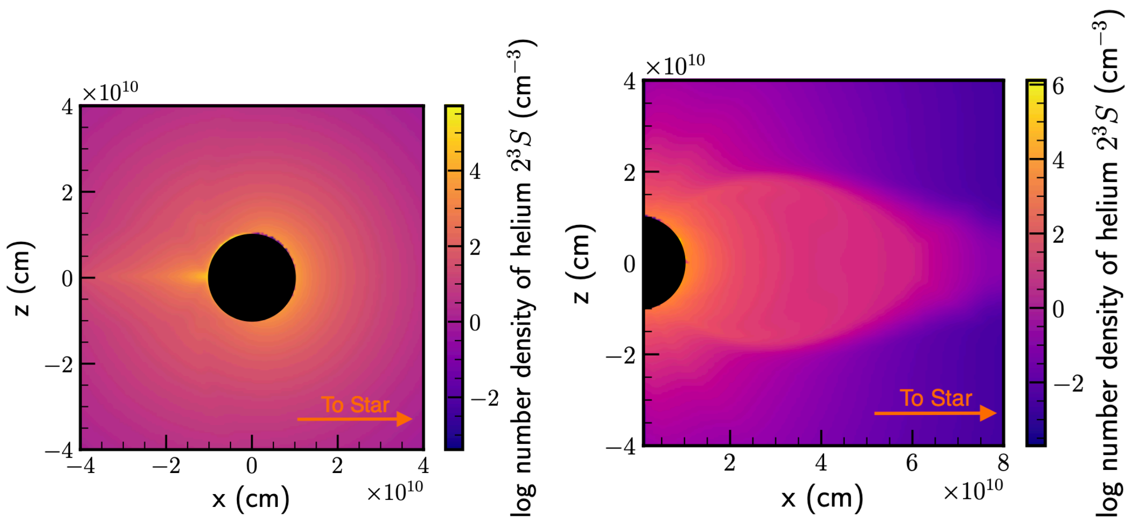

Figure 3.3: The number density of helium in the 2^3S state in the outflow for the hydrodynamic case (left) and the magnetically controlled case (right). In the hydrodynamic case, the density appears to be fairly spherically symmetric. In the magnetically controlled case, the region with closed magnetic field lines has a higher number density of metastable helium atoms than the outflowing regions. This is primarily because the total number density of gas in this region is higher, as it is in hydrostatic equilibrium.

3.2.2 Computing Synthetic Transit Profiles

The goal is to calculate the absorption of stellar radiation at 10830 Å due to the presence of the escaping helium. To elucidate the basic principles, I produce synthetic transmission spectra at mid-transit for the planet transiting with an impact parameter of zero. Since the simulations used to generate the densities and velocities of the outflow are 2D, it is only at mid-transit and with an impact parameter of zero that this approximate symmetry is applicable.

With the assumptions described in 3.1.1, the outflow in the purely hydrodynamic case is rotationally invariant around the line connecting the star and planet (x-axis). This symmetry means that the z coordinate of the grid can be identified with the radial coordinate on the stellar disc. Therefore, the optical depth of the outflow for a ray emanating from any point on the stellar disc is only a function of z and is given by Equation 3.14. This can be integrated over the stellar disc to give the excess absorption caused by the escaping gas.

$$\tau_\nu(z) = \int_{-\infty}^{\infty} n_3(x,z)\sigma_\nu(u_x,T)dx \tag{3.14}$$

$$\text{Excess Depth}(\nu) = \frac{2\int_{R_p}^{R_s} e^{-\tau_\nu(z)} z dz}{R_s^2 - R_p^2} \tag{3.15}$$

where n_3 is the number density of helium atoms in the metastable state, R_p, R_s are the radius of the planet and star, respectively and σ_ν is the absorption cross-section of the helium to photons at a frequency ν, which is a function of the line of sight velocity of the gas, u_x, and the temperature. The absorption cross-section is given by Equations 2.47 and 2.48. The Einstein A coefficient used is $A = 1.022 \times 10^7\ \text{s}^{-1}$ (Kramida et al., 2022). The $2^3S \rightarrow 2^3P$ transition in Helium consists of three distinct lines at 10830.34 Å, 10830.25 Å and 10829.09 Å due to fine structure splitting. The first two of these transitions are blended; however, the third can be distinguished at the spectral resolution of current instruments. The oscillator strengths for these transitions, taken from the NIST atomic database (Kramida et al., 2022), are 0.300, 0.180, and 0.060, respectively. The total absorption cross-section at any wavelength is calculated by summing up the contribution from these three transitions.

Similar to Oklopčić & Hirata (2018), when computing the optical depth, I only took into account gas within the Hill sphere of the planet, which I choose to have a radius of $4R_p$. This approximately corresponds to the Hill sphere radius of a Jupiter-mass planet around a solar-mass star at 0.04 AU. Beyond the Hill sphere, the outflow is significantly affected by the Coriolis force, the stellar tidal field and the stellar wind. Here, the model is no longer applicable. However, unless the stellar wind is very strong, these regions do not contribute greatly at mid-transit (e.g., MacLeod & Oklopčić, 2022). If the planet is further away from the star or the magnetic field is strong, the planetary outflow may not be affected by the circumstellar environment at larger distances from the planet. To do this calculation, I construct a linearly spaced 300×600 cell grid in the (x, z) plane, with x ranging from $[-4R_p, 4R_p]$ and x ranging from $[R_p, 4R_p]$. The integrals in Equations 3.14 and 3.15 are computed with this grid using a middle Riemann sum.

The method used to perform synthetic transits for planets with a magnetic field is different. As discussed in Section, the rotational symmetry around the line connecting the star and planet (x-axis) present in the purely hydrodynamic case is broken by the dipolar structure of the magnetic field (see Figure 3.2. Therefore, one cannot simply compute the 3D density structure by rotating the 2D density distribution around the x-axis. The planetary magnetic field shuts off the outflow on the night-side planet since heat cannot be transported effectively across magnetic field lines. Therefore, the density of helium on the night side of the planet is set to zero. On the day side, I build the 3D density distribution by rotating the 2D helium density distribution around the z-axis (symmetry axis of the dipole). To account for the reduction of EUV flux incident on the atmosphere away from the substellar line due to geometrical effects, I scale the number density of helium in the triplet state in each 2D slice by the square root of the reduction of incident EUV flux at the base the slice. I do this because the simulations are done at high EUV fluxes such that the outflow is in ionization-recombination equilibrium. In this regime, the temperature of the outflow thermostats to 10^4 K and the density at the base of the outflow is proportional to the square root of the incident EUV flux (e.g Murray-Clay et al., 2009; Owen & Alvarez, 2016). Once the 3D density distribution of metastable helium is generated, a synthetic transit is performed using the ray-tracing method outlined in Section 2.4.

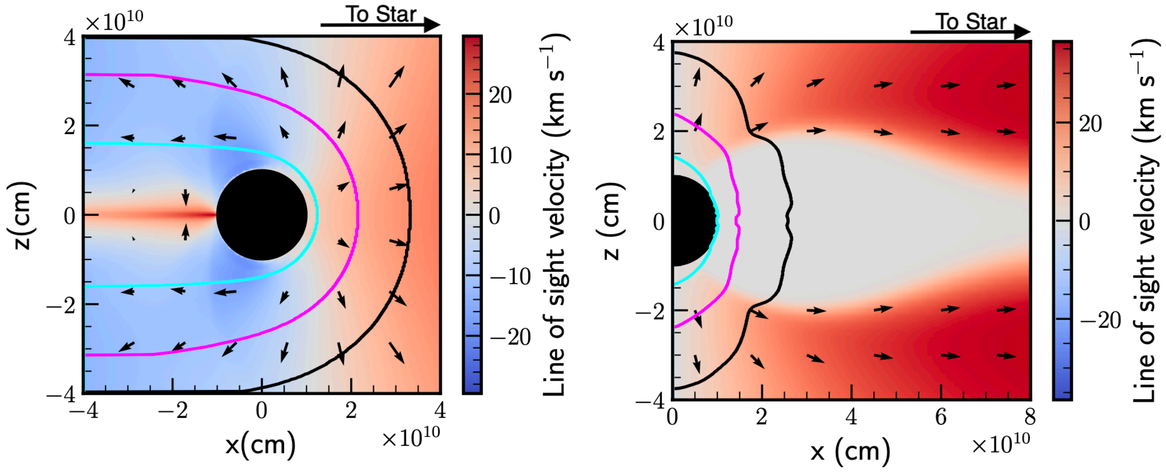

Figure 3.4: Colour map of the line of sight velocity of the outflowing gas in the hydrodynamic case (left) and the magnetically controlled case (right). Contours mark the line of sight optical depth integrated into a two-angstrom bin around the peak absorption wavelength. The black, magenta and cyan mark the $\tau = 0.01, 0.1$ and 1 contours, respectively. The arrows show the velocity field.

3.3 Results

Figure 3.5 shows the excess transit depth for the hydrodynamic and magnetically controlled outflows. As expected, I find the hydrodynamic outflow leads to a blue-shifted spectrum. Figure 3.4 shows that most of the absorption comes from the terminator, where gas is moving towards the observer in transit. The peak absorption is at -8.3 km s^{-1}, which is of order the sound speed of the outflowing gas. It is worth noting that I still see significant absorption in the red wing due to absorption from gas moving towards the star (away from the observer in transit), which has originated from low latitudes on the planet. As a result, the spectrum is asymmetric and broader than expected from thermal broadening.

In contrast, a planet with a 3 Gauss magnetic field shows a symmetric transit spectrum, with a peak absorption centred at 0.5 km s^{-1}. Most of the absorption comes from the dead zone, where the velocity of the gas is stationary, and an area near the poles, where the line of the sight velocity is small (see Figure 3.4). As a result, the spectrum only shows a small velocity shift. Furthermore, since almost all the absorption comes from gas at low velocities, the width of the spectrum is primarily set by the thermal velocity of the gas.

In Figure 3.6, I show how the transit spectrum varies with planetary magnetic field strength. Interestingly, the transit depth does not decrease monotonically with magnetic field strength, even though

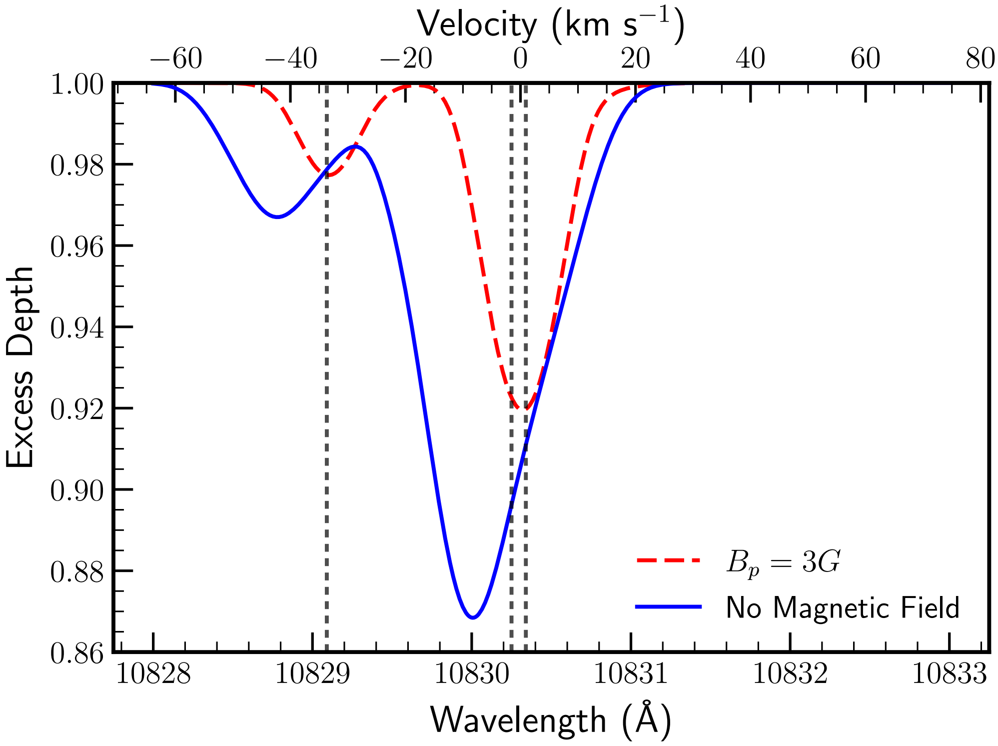

Figure 3.5: Calculated excess absorption for a planet with i) no magnetic field (solid blue) and ii) a surface magnetic field of 3 Gauss (dashed red) at mid-transit with an impact parameter of 0. The black dashed vertical lines are the wavelengths of the helium triplet transitions at 10829.09, 10830.25 and 10830.34 Å. The velocity scale is centred on the blended latter two transitions.

the fraction of open field lines (and the mass loss rate) decreases smoothly as a function of magnetic field strength. As the magnetic field strength is increased, the size of the region where the magnetic field lines are closed increases. This region then blocks more of the stellar disc, contributing more to the transit depth. At the same time, since the mass loss decreases, the column density of gas in the outflowing regions near the poles decreases, contributing less to the transit depth. The weight of these contributions has an opposite dependence on the strength of the magnetic field and results in the transit depth not being a monotonic function of the magnetic field strength.

The overall velocity shift of the transmission spectrum also varies as the magnetic field strength changes. At lower magnetic field strengths, gas pressure is able to open up field lines at lower latitudes. The gas coupled to these field lines has a higher line of sight velocity, resulting in a red-shifted spectrum. In the 0.3 Gauss case, shown in Figure 3.6, this velocity shift is 3.8 km s^{-1}.

For the 3 Gauss case, I also include a situation where the stellar magnetic field is non-zero, and the ratio of stellar to planetary magnetic field strength is given by $\beta_* = 0.001$. For a planet at 0.04

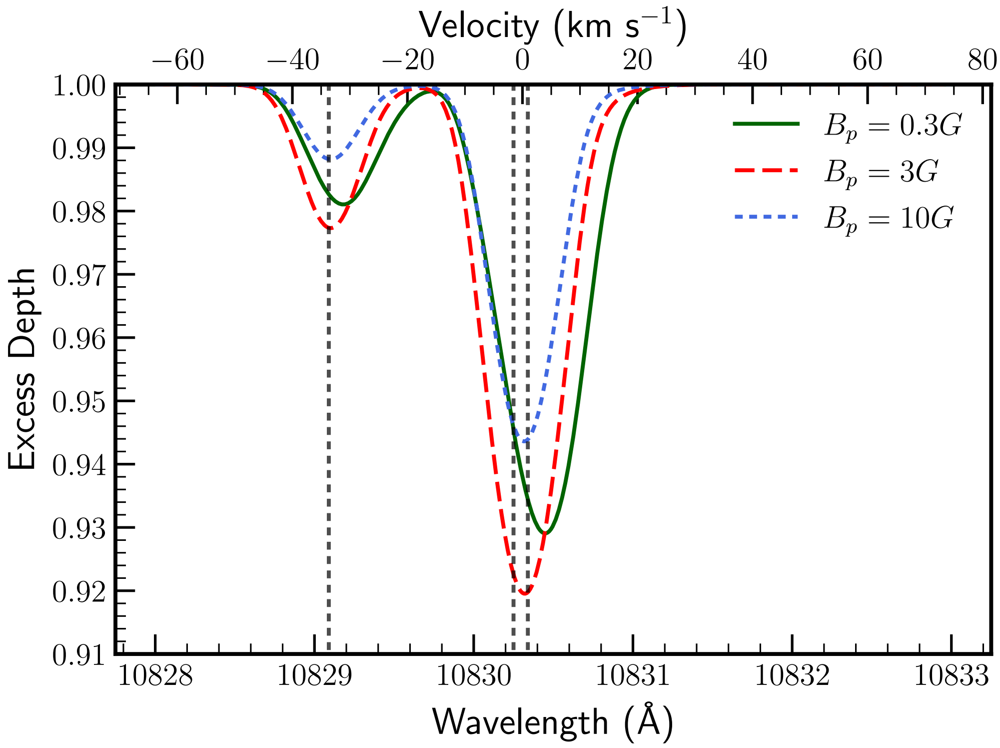

Figure 3.6: Calculated excess absorption as a function of wavelength for different planetary magnetic field strengths. For a planetary magnetic field of 3 Gauss, I also include a case in which the stellar magnetic field is non-zero. The black dashed vertical lines are the wavelengths of the helium triplet transitions at 10829.09, 10830.25 and 10830.34 Å. The velocity scale is the same as in Figure 3.5.

AU around a solar-radius star, this corresponds to a stellar surface magnetic field of 1 Gauss. In general, the stellar magnetic field is able to open more planetary magnetic field lines. This can either increase or decrease the transit depth depending on how the contributions from the closed region and outflowing regions change. However, for this value of the stellar magnetic field, there is little change in the transit spectrum, as the opening of field lines is dominated by the gas pressure rather than by the stellar magnetic field.

3.4 Discussion and Conclusions

I have post-processed 2D HD and MHD simulations of a hot Jupiter undergoing photoevaporation and calculated in-transit absorption signal due to the 10830 Å line of helium. If the planet has no magnetic field, the transit signal is blue-shifted $\Delta v = -8.3$ km s^{-1} due to the absorption from gas that flows from the hot day side to a cold night side. When a planetary magnetic field (between 0.3-10

Gauss) is included, the transit signal has either no apparent velocity shift or a very slight red-shift, as escaping gas from the day side is tied to magnetic field lines and moves away from the observer in transit.

At the current resolution of ground-based instruments, this difference in line-centre velocity is observable and may be used to test whether outflows are magnetically controlled or not and consequently put constraints on the magnetic field strengths of planets. As the observed velocity difference is due to large-scale changes in the geometry of the flow, this method should be fairly robust to the specifics of the photoevaporative flow (e.g. mass loss rate and temperature). However, further work is required to ensure that the results are still true in full 3D simulations over a more extensive region of parameter space and for various magnetic field configurations. I will discuss this in Section 3.4.1.

For magnetically controlled flows, observationally distinguishing between different planetary magnetic field strengths is a more difficult task. The clearest difference is that lower field strengths with more open field lines lead to a more red-shifted transit. More open field lines can also increase high-velocity gas absorption far from the planet, leading to asymmetric transits with an extended red wing. Observations of the escaping atmosphere of WASP-52b show that the transit spectrum is unshifted with respect to the planet's rest frame and has a slight asymmetry in the red wing. I speculate that this might indicate that the outflow is magnetically controlled. Overall, I caution that since the differences in these spectra are relatively minor, model and observational uncertainties most likely make different magnetic field cases indistinguishable at the resolution of current instruments.

3.4.1 Limitations

Use of Owen & Adams (2014) simulations and 3D effects

In reality, atmospheric escape is a 3D dimensional process, and 3D radiation magneto-hydrodynamics simulations that include rotational effects are necessary to confirm the validity of this work. The Owen & Adams (2014) simulations are simplistic when compared to current state-of-the-art simulations; however, as discussed above, they are the only simulation set that included radiative transfer, models with and without magnetic fields and a reasonable parameter study within the same framework. This allowed us to make meaningful comparisons between simulations that did and did not include magnetic fields. However, it is important to discuss some of the limitations of these simulations. The Owen & Adams (2014) simulations were the first multi-dimensional simulations of photoevaporation that included on-the-fly radiative transfer. As such, they used a simplified algorithm which assumed an ionization-recombination balance for the hydrogen and took the ionized gas to be at 10^4 K, where the temperature was computed based on the local ionization fraction (e.g. Gritschneder et al., 2009). This ionization-recombination balance is well known to be applicable to planets around young stars (e.g Murray-Clay et al., 2009; Owen & Alvarez, 2016), yet most observations of helium outflows are for old planets where this approximation does not hold. The approximations of the Owen & Adams (2014) simulations are likely driving two quantitative results of the simulations: firstly, the high fluxes produce a high rate of recombinations, and thus, the helium transit depths are likely overestimated compared to older systems; secondly, the outflow velocity (and hence the magnitude of the velocity shift) depends directly on the gas' temperature, with higher temperatures giving higher outflow velocities. Outflows around lower-mass, older planets are more likely to be in the "energy-limited" regime (Owen & Alvarez, 2016), where the outflow temperatures are necessarily lower, and hence the simulated $\sim$ 8 km s^{-1} blue-shifts are likely overestimates. However, as discussed above, based on the results of more recent 3D simulations, I am confident the qualitative conclusions about blue-shifts arising in the hydrodynamic cases are robust. Hence, the detection or lack of blue shift can be used to make inferences about the strength of any planetary magnetic field.

We also re-emphasize that I focus on a particular area of parameter space where the ram pressure of the planetary wind or the magnetic pressure of the planet dominates over the stellar magnetic pressure or stellar wind ram pressure close to the planet. Whether the stellar wind or stellar magnetic field has a larger influence on the orbit of the planet depends on the mass loss rate of the star, the magnetic field of the star, stellar wind velocity and the semi-major axis of the planet. For hot Jupiters,the stellar magnetic field or the stellar wind can dominate their interaction with the planet, depending on the specific stellar and planetary parameters. The magnetic pressure of a stellar dipolar field decreases with distance as r^6, while the stellar wind ram pressure decreases more gradually as r^2. Because the magnetic pressure decreases more rapidly with distance than stellar wind ram pressure, the stellar wind is more likely to dominate over the stellar magnetic field in the interaction with sub-Neptunes, which typically orbit farther from their host stars than hot Jupiters.

The primary effect of increasing the strength of the stellar magnetic field is to open more planetary field lines Owen & Adams (2014). At low stellar magnetic field strengths, this can increase the mass loss rate. At high stellar magnetic field strengths, the flow cannot smoothly transition through the sonic point along these open field lines, and the mass loss rate can actually decrease (Owen & Adams, 2014). These changes can vary the transit depth. However, it is not expected to significantly change the velocity of the absorbing gas and, therefore, the velocity shift of the transit.

On the other hand, the stellar wind may have a significant effect on the velocity shift of the transmission spectrum. If the planet is outside the Alfvén radius of the star, the ram pressure of the stellar wind dominates over the magnetic pressure of the stellar wind and the magnetic field lines in the stellar wind follow the stellar wind plasma. The effect of the stellar wind on the geometry of the planetary outflow has been studied in both hydrodynamic and MHD simulations. As the strength of the stellar wind is increased compared to the planetary outflow or planetary magnetic field, the stellar wind is able to confine the planetary outflow closer to the surface of the planet. On scales larger than the Hill sphere of the planet, the stellar wind will shape the outflow into a cometary tail that is being radially accelerated away from the star (e.g., Matsakos et al., 2015; Khodachenko et al., 2019; McCann et al., 2019). In essentially isothermal 3D hydrodynamic simulations including helium, MacLeod & Oklopčić (2022) showed that this could result in both blue-shifted absorption during the optical transit and significant blue-shifted post-optical transit absorption. This is also apparent in 3D radiation-hydrodynamic simulations performed by Wang & Dai (2021).

MHD simulations, including the radial magnetic field of the stellar wind, have also shown that the stellar wind causes planetary magnetic field lines to bend towards the night side (e.g., Kislyakova et al., 2014; Carolan et al., 2021b; Khodachenko et al., 2021; Ben-Jaffel et al., 2022). It is possible that this could result in a blue-shifted absorption signature during the transit of the planet, even if the planet had a reasonably strong magnetic field. However, it is likely that this would also cause a significant blue-shifted post-optical transit absorption like that seen in the hydrodynamic case. More 3D simulations are necessary to understand how degenerate observations are over the full parameter space.

Eccentricity Uncertainty

To definitively assert that the velocity shift is due to the outflow, one must know the planet's eccentricity. Since highly irradiated planets are close to their host stars, they are generally assumed to have undergone orbital circularization. Small deviations away from a circular orbit can cause an apparent velocity shift, $\Delta v_{\rm los}$, of:

$$\Delta v_{\rm los} \sim v_k e \cos\omega \tag{3.16}$$

where v_k is Keplerian velocity, e is the eccentricity and ω is the argument of periastron of the planet (e.g Murray & Correia, 2010). For a planet with an orbital velocity of $\sim$ 100 km s^{-1}, an eccentricity uncertainty of ~0.1 leads a velocity uncertainty of $\sim$ 10 km s^{-1}, which is on the order of the velocity shift of due to the outflow geometry. Therefore, the eccentricity of the planet must known precisely to confidently say that the observed velocity shift of the helium 10830 Å is due to outflow dynamics. The quantity $e\cos\omega$ can be precisely measured from radial velocity observations (e.g., Haswell, 2010), or secondary eclipse observations (e.g., Winn, 2010). However, for planets that have only been observed through the transit method, eccentricities uncertainties are rarely < 0.1 (Van Eylen et al., 2019). This is also true when TTVs are used to determine eccentricities in multi-planetary systems (Van Eylen & Albrecht, 2015).

3.4.2 Implications for Real Systems

Ideally, it would be possible to use helium observations to constrain these planets' magnetic fields. As highlighted in the previous section, eccentricity uncertainties generally mean that it is not possible to make claims about the magnetic field strengths of individual planets based on these observations. However, I speculate about trends in the population.

Table 3.1 lists spectroscopic detections of helium escape. For each planet, I quote the observed velocity shift of the absorption relative to the planet's rest frame, which is often determined by assuming a circular orbit if the planet is not known to be eccentric. These are not directly comparable to my models, as the observed transit depth is generally computed by integrating over all in-transit phases. I also estimate a critical surface magnetic field strength B_c at which the flow transitions from "hydrodynamic" to "magnetically controlled" and no longer expect to see a blue-shifted transit spectrum. I approximate this value as the maximum surface magnetic field so that the outflow opens all field lines. Although, I caution that this is likely to be an overestimate. Since the outflow may be able to wrap around to the night side in the terminator region before all field lines are opened, 3D MHD simulations will be required to investigate this quantitatively.

This critical magnetic field strength is found by requiring that the thermal pressure exceeds the magnetic pressure for $r > R_p$. I estimate the thermal pressure by i) assuming the outflow is an isothermal Parker wind with a fixed sound speed and mass loss rate or ii) assuming the outflow is in photoionization equilibrium. In both cases, the detailed procedure used to calculate the critical magnetic field is explained in Section 3.5. In Table 3.1, I give three critical magnetic field strength values. The first two are calculated assuming the isothermal Parker wind case, where the sound speed is 0.3×10^4K$/10^4$K, and the mass loss rate is given by the energy-limited mass loss rate (Equation 3.2) with efficiency $\eta = 0.1$. The final estimate is given by the photoionization equilibrium case, where the gas temperature 10^4 K. In general, this last method gives a slightly larger value for the critical magnetic field but is the least applicable to old planets.

To calculate the critical magnetic field strength, I needed to estimate the F_{uv} received by each planet. For this, I used values given in each of the cited detection papers (see Table 3.1). If no estimate was present, I used estimates from Kirk et al. (2022), in which they scaled the UV flux of a star of similar spectral type, taken from the MUSCLES survey (France et al., 2016; Loyd et al., 2016; Youngblood et al., 2016), to the semi-major axis of the planet. I note that the reconstructed XUV flux has significant uncertainties, and my method for calculating the thermal pressure of the outflow are only approximate. Therefore I expect that my estimate for B_c may vary by an order of magnitude.

We also estimate the extent to which the stellar wind can confine the outflow. To effectively radially accelerate the planetary gas to produce a blue-shifted transit, the stellar wind must be able to penetrate close to the planetary surface. I approximately calculate the position of the bow shock produced when the stellar wind and planetary outflow collide. The bow shock is defined by the condition that the momentum fluxes of the stellar wind and planetary outflow balance. In the simple case, where outflows are spherical, I can approximate the radial distance of the bow shock from the planet r_b:

$$r_b = a_{\rm p}\sqrt{\frac{\dot{M}c_s}{\dot{M}_* u_*}} \tag{3.17}$$

where $\dot{M}_*$ is the mass loss rate of the star, $\dot{M}$ is the mass loss rate of the planet, u_* is the stellar wind velocity and $a_{\rm p}$ is the semi-major axis of the planet. To calculate r_b, I estimate the mass loss rate of the planet using the energy-limited mass loss rate (Equation 3.2) with efficiency $\eta = 0.1$ and use solar-like wind values of $\dot{M}_* = 10^{-14} M_\odot$ yr^{-1} and $u_* = 150$ km s^{-1}. If significant absorption occurs outside this radius, then the stellar wind is likely to play an important role in determining the shape of the transit. I also note that a strong planetary magnetic field can considerably increase the bow shock distance. In this case, the bow shock distance is approximated by the point at which the stellar wind ram pressure and magnetic pressure of the planetary field balance. Therefore, I also calculate the position of the bow shock considering the effects of a 1 Gauss surface magnetic field. Here the expression for r_b is given by:

$$r_b = \left(\frac{B_0^2 a_{\rm p}^2}{2\dot{M}_* u_*}\right)^{\frac{1}{4}} \tag{3.18}$$

Interestingly, ten out of the twelve systems show blue-shifted absorption. Thus, it is highly unlikely that uncertainties in planetary motion can account for all of these. Therefore, it is likely that some of these blue-shifts can be attributed to the geometry of the outflow. There are two explanations for this. The first possibility is that these planets have relatively weak surface magnetic fields (B $\lesssim$ 0.1 Gauss), and day-to-night winds are responsible for the blue-shifted transit. For sub-Neptunes, this would agree with the findings of Owen (2019), which demonstrated that the suppression of atmospheric mass loss by the presence of surface magnetic fields $\gtrsim$ 0.3 Gauss is not consistent with both the position of the radius valley and the rocky composition of planets below the valley. This is not inconsistent with dynamo-generated magnetic fields in the cores of sub-Neptunes being on the order of a few Gauss, like solar system planets, as a few percent by mass hydrogen/helium envelope can greatly increase the radius of the planet and particularly raise the upper atmosphere where atmospheric mass loss is taking place. Since the magnetic field strength for a dipole field scales like r^{-3}, the magnetic field can be much weaker in these regions. For hot Jupiters, this conclusion would favour the argument of Grießmeier et al. (2004) that slow rotation of hot Jupiters due to tidal locking leads to magnetic fields that are orders of magnitude smaller than Jupiter's. This is in opposition to the argument of Christensen et al. (2009) which predicts magnetic field strengths an order of magnitude greater than Jupiter's, based on a scaling relation between magnetic field strength and energy flux.

The other possibility is that stellar winds are able to penetrate close to the planetary surface and radially accelerate the gas to produce the observed blue-shifts. A comet-like tail of escaping helium extending out to ~ 7 planetary radii has been detected in the case WASP-107b (Spake et al., 2021) and to a lesser extent for WASP-69b (Nortmann et al., 2018), HAT-P-18b (Fu et al., 2022) and HD189733b (Guilluy et al., 2020). This may be evidence that the stellar wind plays an role in shaping the outflow of some these planets. A lower limit can be set on the extent of the outflow by assuming that the gas is optically thick to 10830 Å radiation, which can compared to the bow shock radius to assess the importance of stellar wind. I call this the "minimum absorption area", and calculate its value at mid-transit (see Table 3.1). I stress the gas is optically thin (e.g MacLeod & Oklopčić, 2022) and therefore the actual extent can be significantly larger than this estimate. A good example of this is the transit of WASP-107b, which is found to a have a much smaller minimum absorption area $\sim 2R_p$, than is temporally observed $\sim 7R_p$ (e.g, Spake et al., 2022).

In general, if the planets have weak magnetic fields, solar or moderately supersolar winds are required to set the bow shock radius close enough to the planet to disrupt the planetary outflow significantly. This is certainly feasible based on estimates of stellar wind mass rates from detections of astrospheric absorption (e.g., Wood et al., 2005, 2021). However, if these planets are able to host significant surface magnetic fields ($B \gtrsim 1$ Gauss), then stellar winds with mass loss rates orders of magnitudes greater than the Sun would be required. Thus, I speculate that regarding the population of close-in planets for which helium observations have been taken, there is no evidence that these planets possess magnetic field strengths strong enough to control the topology of any photoevaporative outflow.

Table 3.1: Detections of helium atmospheric escape using high-resolution spectroscopy and the observed velocity shift of the outflow in the rest frame of the planet. I have provided uncertainties on the observed velocity shift, where given in the detection paper. These are generally of the order of a few km s^{-1}. I estimate the maximum surface magnetic field B_c such that all field lines are opened by the planetary outflow. The three numbers correspond to estimating strengths when the outflow is approximated to be i) an isothermal Parker wind at 10^4 K, ii) an isothermal Parker wind at 0.3×10^4 K and iii) in photoionization-recombination equilibrium. For the former two calculations, I estimate the mass loss rate of the planet using the energy-limited formula with an efficiency of 0.1. I also estimate the bow shock radii at which the stellar wind collides with the planetary outflow (Equation 3.17) and the magnetosphere corresponding to a planet with a surface magnetic field of 1 Gauss (Equation 3.18). The minimum absorption area is a lower limit on the extent of the outflow assuming it is optically thick.

Planet Name	Radius (R_J)	B_c (Gauss)	Bow Shock Radius Hydrodynamic (R_p)	Bow Shock Radius Magnetic (R_p)	Observed Velocity Shift (km s^{-1})	Minimum Absorber Area (R_p)	Reference
GJ 1214b	0.24	0.003 0.005 0.15	0.2	7.1	-5^{+4}_{-7}	1.6	Orell-Miquel et al. (2022)[(1)]
GJ 3470b	0.36	0.01 0.02 0.24	1.2	10.5	-3.2 ± 1.3	1.9	Palle et al. (2020)
Hat-P-11b	0.39	0.01 0.05 0.30	1.7	13.5	-3	2.2	Allart et al. (2018)
HD 189733b	1.13	0.19 1.56 0.54	1.1	10.3	-3.5 ± 0.4	1.2	Salz et al. (2018)
HD 209458b	1.39	0.02 0.15 0.23	0.7	12.9	-1.8 ± 1.3	1.3	Alonso-Floriano et al. (2019)
TOI-1430.01	0.18	0.02 0.05 0.45	5.4	15.7	-4.0 ± 1.3	3.6	Zhang et al. (2023b)
TOI-1683.01	0.18	0.03 0.08 0.53	3.4	11.3	-6.7 ± 2.8	3.4	Zhang et al. (2023b)
TOI-2076b	0.22	0.03 0.06 0.46	5.7	14.9	-6.7 ± 1.4	3.5	Zhang et al. (2023b)[(2)]
TOI-560b	0.25	0.02 0.04 0.38	3.8	14.6	4.3 ± 1.4	2.4	Zhang et al. (2022a)
Wasp-107b	0.92	0.01 0.03 0.23	2.5	13.9	-2.4 ± 0.4	2.2	Kirk et al. (2020)
Wasp-52b	1.2	0.06 0.43 0.49	2.2	9.6	0.0 ± 1.2	1.6	Kirk et al. (2022)
Wasp-69b	1.0	0.02 0.13 0.32	2.0	12.6	-3.6 ± 0.2	1.8	Nortmann et al. (2018)

3.5 Solving for the critical magnetic field strength

In this section, I describe the procedure used to obtain the value of the critical magnetic field strength given in Table 3.1 when the outflow is i) modelled as an isothermal Parker wind or ii) in photoionization-recombination equilibrium.

3.5.1 Assuming the outflow is an isothermal Parker Wind

Here, I outline the procedure to obtain the critical magnetic strength when the outflow is approximated to be an isothermal Parker wind. For a given mass loss rate and sound speed, the density and gas pressure can be written analytically in terms of the Lambert W function (Cranmer, 2004). The magnetic pressure along this streamline is given by:

$$P_B = \frac{B_0^2}{8\pi}\left(\frac{R_{\rm p}}{r}\right)^6 \tag{3.19}$$

The critical magnetic field is given by the value of the surface magnetic field such that gas pressure exceeds the magnetic pressure over for $r > R_p$ except one point where they are equal, which I denote r_B. This point is either R_p or at this point the magnetic pressure and thermal pressure are tangent. If they are tangent at this point, the thermal and magnetic pressure should satisfy:

$$P_{\rm th}(r_B) = P_B(r_B) \tag{3.20}$$

$$\frac{dP_{\rm th}}{dr}(r_B) = \frac{dP_B}{dr}(r_B) \tag{3.21}$$

We can combine these two equations by inserting the form of the magnetic pressure (Equation 3.19) in order to get an equation just in terms of the thermal pressure.

$$\frac{dP_{\rm th}}{dr}(r) + \frac{6P_{\rm th}(r)}{r} = 0 \tag{3.22}$$

Using the Lambert W function (Cranmer, 2004), the thermal pressure is given by:

$$P_{\rm th}(r) = \frac{\dot{M} c_s^2}{4\pi r^2 u(r)} \tag{3.23}$$

$$u = \begin{cases} -c_s^2 W_0[-D(r)] & r \le r_c \\ -c_s^2 W_{-1}[-D(r)] & r > r_c \end{cases} \tag{3.24}$$

$$D(r) = \left(\frac{r}{r_c}\right)^{-4} \exp\left[4\left(1 - \frac{r_c}{r}\right) - 1\right] \tag{3.25}$$

and the derivative of the thermal pressure is given by:

$$\frac{dP_{\rm th}}{dr} = -\frac{\dot{M}_{\rm p} c_s^2 (2ru(r) + r^2 \frac{du}{dr})}{4\pi r^4 u(r)^2} \tag{3.26}$$

$$\frac{du}{dr} = \begin{cases} c_s \frac{\sqrt{-W_0[-D(r)]}}{2D(r)(W_0[-D(r)]+1)} & r \le r_c \\ c_s \frac{\sqrt{-W_{-1}[-D(r)]}}{2D(r)(W_{-1}[-D(r)]+1)} & r \ge r_c \end{cases} \tag{3.27}$$

Equation 3.22 can be numerically solved for r_B. If $r_B > R_p$, the conditions of Equation 3.20 are satisfied and the critical magnetic field strength is given by:

$$B_c = \sqrt{\frac{2\dot{M} c_s^2}{r_B^2 u(r_B)} \left(\frac{r_B}{R_p}\right)^6} \tag{3.28}$$

An example of this case is shown in the left hand panel of Figure 3.7 (corresponding to HD 189733b). If $r_B < R_p$, there does not exist a magnetic field strength in which the conditions of Equation 3.20 are satisfied. Therefore, I set the critical magnetic field strength to be such that the magnetic pressure equals the gas pressure at R_p, which is equivalent to setting $P_{\rm th}(R_p) = P_B(R_p)$. Therefore B_c is given by:

$$B_c = \sqrt{\frac{2\dot{M}_{\rm p} c_s^2}{R_p^2 u(R_p)}} \tag{3.29}$$

An example of this case is shown in the right hand panel of Figure 3.7 (corresponding to Wasp-107b).

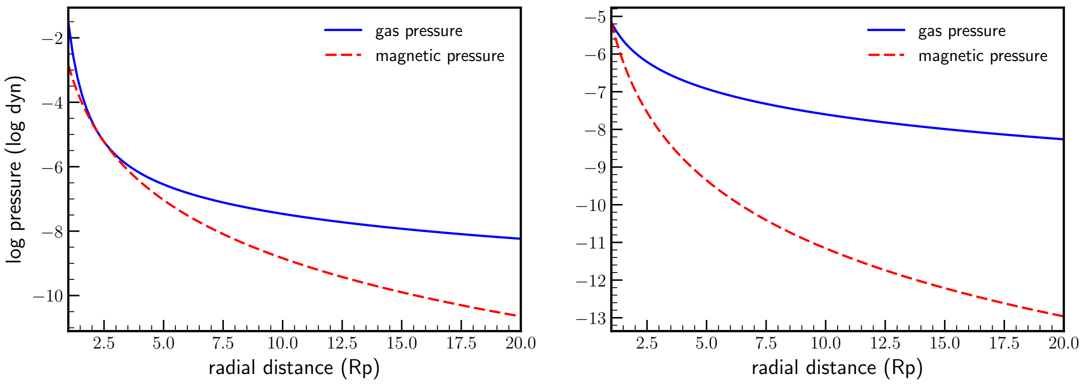

Figure 3.7: A comparison between the magnetic pressure and gas pressure at the critical magnetic field strength for HD189733b (left) and WASP-107b (right) assuming the outflow is an isothermal Parker wind at 10^4 K.

3.5.2 Assuming the outflow is photoionization equilibrium

For completeness, I also estimate this critical transition assuming that the flow is in photoionization equilibrium (e.g Owen & Adams, 2014; Owen & Alvarez, 2016). I note that this is not the case for old low-mass planets. In this case, I approximate that all field lines are opened if the pressure at the base of the flow is greater than the magnetic pressure. I denote this ratio as κ:

$$\kappa = \frac{B_0^2}{8\pi P_0} \tag{3.30}$$

where P_0 is the surface gas pressure. The surface pressure is calculated by balancing the number of incoming photons with the number of recombinations at the ionization front, assuming the ionization front is located deep in the planet's atmosphere. Using Equation (50) from Owen & Adams (2014) as the starting point, the surface pressure can be cast in terms of the planetary properties and the incident flux.

$$P_0 \approx 5 \times 10^{-13} \sqrt{\frac{GM_p c_s^2 F_{\rm uv}}{R_p^2}} \text{ dyn} \tag{3.31}$$

Where $F_{\rm uv}$ is the incident EUV flux. Therefore, the critical magnetic field strength becomes

$$B_c \approx 0.25 \left(\frac{M_p}{M_J}\right)^{\frac{1}{4}} \left(\frac{F_{\rm uv}}{10^4 \text{ erg s}^{-1}}\right)^{\frac{1}{4}} \left(\frac{c_s}{10 \text{ km s}^{-1}}\right)^{\frac{1}{2}} \left(\frac{R_p}{R_J}\right)^{-\frac{1}{2}} \tag{3.32}$$

3.6 Summary and Conclusion

In Summary, I have presented a method to detect the magnetic fields of close-in exoplanets undergoing atmospheric escape using transit spectroscopy of the helium 10830 Å line. I propose that planets with weak magnetic fields, which are unable to control the outflow's topology, produce blue-shifted transits due to day-to-night flows. In contrast, planets with strong magnetic fields suppress this flow, forcing the gas to follow a dipolar magnetic topology, resulting in unshifted or slightly red-shifted transit profiles. To test this concept, I have post-processed 2D HD and MHD simulations of a hot Jupiter undergoing photoevaporation and calculated the in-transit absorption signal at 10830 Å. As expected, I found that hydrodynamically dominated outflows generate blue-shifted transits of order the sound speed. Meanwhile, strong surface magnetic fields lead to unshifted or sub-sound speed red-shifted profiles. Ground-based, high-resolution observations can distinguish between these different profiles, although uncertainties in orbital eccentricity often make it difficult to conclusively attribute velocity shifts to the outflow in individual planets. Interestingly, most observed helium profiles are blue-shifted, which I suggest is a tentative indication that many close-in planets have surface dipole magnetic field strengths $\lesssim 0.3$ G. Further 3D global MHD simulations, which include the interaction between the magnetic field and the stellar wind are necessary to confirm this.

Chapter 4

Detecting Circumstellar Disks Generated by Photoevaporating Planets

In this chapter, I discuss the generation of long-lived circumstellar gas fed by extreme mass loss from highly irradiated planets. Typically studies of atmospheric escape focus on the gas close to the planet. Here, the gas is densest and therefore most strongly absorbs stellar light. However, if the escaping gas is not quickly dispersed by the stellar wind, radiation pressure or rapidly accreted onto the star, the gas will build up in a dense circumstellar cloud around the star. Three dimensional hydrodynamics simulations indicate that this happens when the strength of the planetary wind out-competes the stellar wind (e.g., Debrecht et al., 2018; MacLeod & Oklopčić, 2022).

Observationally, the presence of large quantities of circumstellar gas may imprint itself on the spectrum of the star through absorption or emission features. As only a fraction of stars host highly irradiated transiting exoplanets, the hope is to identify stars hosting circumstellar gas by their unusual features compared to typical field stars (e.g., Haswell et al., 2020). A curious feature that has been identified as a possible marker of circumstellar gas is an anomalous reduction of flux in the line cores of the stellar chromospheric Mg II h & k and Ca II H & K lines. This is inspired by observations WASP-12, which hosts an ultra-hot Jupiter, WASP-12 b, on 1.09 day orbit. Near-ultraviolet observations (NUV) of WASP-12 exhibited a complete lack of usually bright Mg II h & k emission cores (Haswell et al., 2012), compared to others stars of similar age and rotational velocity (see Figure 4.1). As stars with

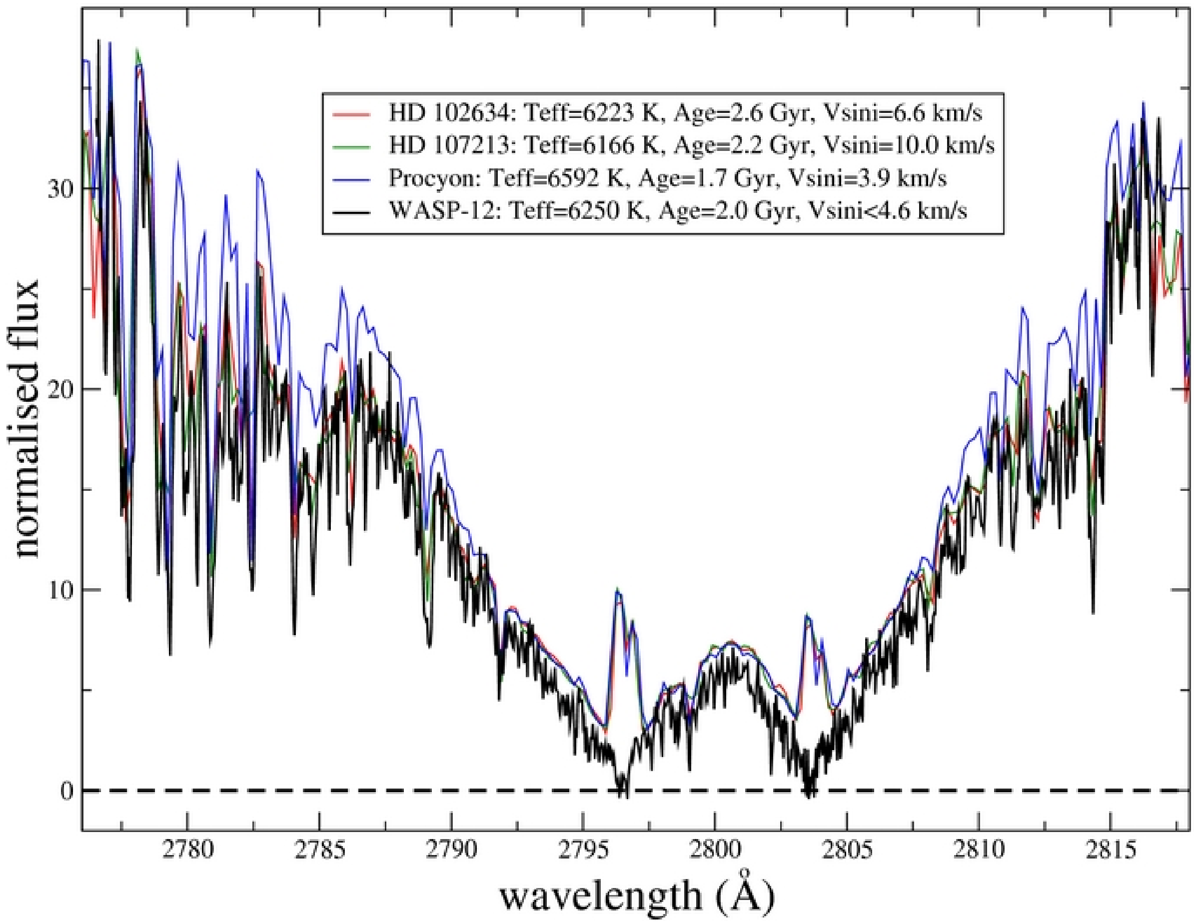

Figure 4.1: The Mg II h & k lines of WASP-12 compared to stars of similar effective temperature, age and rotational velocity. The absence of the emission cores in WASP-12 compared to the other stars is attributed to absorption from Mg II ions in circumstellar gas generated by mass loss from the hot Jupiter WASP-12b. Figure taken from Haswell et al. (2012).

these properties in common are expected to have similar activity, and Mg II h & k emission cores, this is a surprising result. They attributed the lack of observed flux due to absorption from Mg II ions in circumstellar gas generated by mass loss from the atmosphere of WASP-12 b. Later optical observations found that WASP-12 exhibited deeper Ca II H & K lines cores than expected from similar stars (Fossati et al., 2013), which was attributed to absorption from Ca II ions in the circumstellar gas.

The OU-SALT survey performed a homogeneous study of the chromospheric activity of southern hemisphere close-in transiting exoplanets (Doherty, 2020). The activity of a star is often put in terms of log R'_{HK}, which is a measure of the relative strength of the Ca II H & K emission cores to the nearby continuum (corrected for stellar type). A more active star has a higher relative line core emission and therefore has a higher log R'_{HK}. This survey found that approximately a third of the OU-SALT sample of main sequence stars displayed a log $R'_{HK} < 5.1$ compared to 2% of main sequence field stars (Doherty, 2020), possibility indicative of circumstellar gas absorbing in the Ca II H & K line cores for stars hosting hot Jupiters. However, this study does not correct for the selection effect that stars hosting giant planets are more metal rich than field stars (Adibekyan, 2019), which is problematic as stellar metallicity is negatively correlated with log R'_{HK} (Rocha-Pinto & Maciel, 1998).

Other spectral tracers can provide the additional evidence needed to confirm the presence of this circumstellar gas. Although Lyman-α is often used to probe such environments, it is not ideal due to its extinction by the interstellar medium, limiting observations to nearby stars. In contrast, the helium 10830 Å line, which does not suffer from this issue, offers a promising alternative to probe the circumstellar gas.

Since the circumstellar gas obscures the star at all orbital phases, its presence cannot be easily detected through temporal variations in the stellar spectrum. Therefore, to evaluate how helium 10830 Å observations might reveal the presence of circumstellar gas, it is necessary to understand the behaviour of this stellar line. In main sequence FGK stars, the helium 10830 Å feature is a chromospheric absorption line. Studies of the Sun show that helium 10830 Å absorption spatially traces the Hα network and soft X-ray emission, establishing a connection between these the strength of helium 10830 Å absorption and other activity tracers (Giovanelli et al., 1972). Studies have shown that there is a strong correlation between the helium 10830 Å line and X-ray flux in late type stars for non-active stars (Zirin, 1982; Smith, 2016), but that this disappears for active stars (Sanz-Forcada & Dupree, 2008). Modelling of the helium 10830 Å line in G and F stars found that there is a maximum equivalent width at $\sim$ 450 mÅ (Andretta & Giampapa, 1995). For higher levels of activity, emission starts to fill in the line. Therefore, an equivalent width deeper than $\sim$ 450 mÅ may be a good indicator of the presence of circumstellar gas. Similarly to the X-ray correlation, Smith (2016) demonstrated a strong relationship between log $\mathrm{R'_{HK}}$ and the helium 10830 Å equivalent width (EW) for non-active stars (see Figure 4.2). Deviations from this correlation are unlikely to have a stellar origin, making them promising indicators of the presence of circumstellar disks.

It is important to note that the Smith (2016) sample is unlikely to be significantly influenced by planets, allowing us to consider the observed correlation as intrinsic to the stars. The occurrence rate

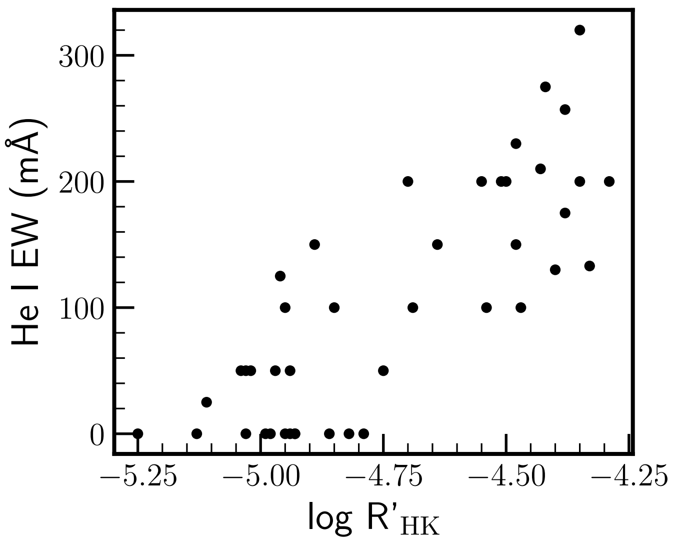

Figure 4.2: Left: The equivalent width of the helium 10830 Å line versus the Ca II H & K emission index log R'_{HK} from a sample of dwarf stars ranging from K dwarfs to late F stars compiled by Smith (2016). Right: The equivalent width of the helium 10830 Å line versus log L_x/L_{bol} for the same sample.

of hot Jupiters around FGK stars is $\lesssim 1.5\%$ (Howard et al., 2012; Petigura et al., 2017). The transit probability of the circumstellar gas is:

$$\sim \frac{h + R_*}{R} \tag{4.1}$$

where h is the scale height of the gas and R is the orbital separation of the gas. At several stellar radii, this is $\sim 20\%$. Thus, the probability of a random field star hosting a transiting circumstellar disk is $\sim 0.3\%$, and it is not likely that any star in the Smith (2016) sample is polluted by a star with an ablating planet that is producing transiting circumstellar gas.

4.1 Circumstellar Disk Model

In this section, I build a simple analytic model of the circumstellar gas disk generated by an evaporating planet. A requirement to build this disk is that the stellar wind or radiation pressure must be unable to significantly disrupt the planetary outflow. In this scenario, 3D hydrodynamic simulations indicate that the gas initially forms a torus around the star (e.g., Debrecht et al., 2018; McCann et al., 2019;

MacLeod & Oklopčić, 2022). As the planet continues to lose mass, the gas density within the torus increases, though its long-term evolution remains uncertain. Viscous forces, magnetic interactions with the star and gravitational interactions with the planet, which drive the exchange of angular momentum and energy, may subsequently alter the geometry and density of the circumstellar gas. These processes have been well studied in the context of planet evolution in protoplanetary disks, however, they have not been investigated for circumstellar material generated by photoevaporating planets, which is in a significantly different part of parameter space. 3D global photoevaporation simulations are highly computationally expensive and can typically only be run for a few orbits (e.g., Debrecht et al., 2018), far short of the timescales needed to properly explore these effects. Therefore, I develop a semi-analytical model of the circumstellar gas, incorporating the key physical processes that shape it. The primary goal is to identify the observational signatures of this gas and to determine the most effective methods for detecting it.

4.1.1 Geometry

I model the circumstellar gas as a constant density Keplerian disk with a constant height. As the planetary escape velocity is small compared to the planet's orbital velocity, the escaping gas only has a small angular momentum and energy difference compared to the planet. Therefore, initially the gas is put on approximately circular orbits at the semi-major axis of the planet (see Chapter 2). The subsequent radial evolution of the gas must be slow compared to the orbital timescale of the gas, otherwise the gas will quickly be dispersed and not build up in a disk around the star. Note that the gas may still be pushed outward slowly as a result of the stellar wind/radiation pressure; however, since this is slow, it does not greatly change the density structure of the gas. Consequently, the gas is approximated to be on circular Keplerian orbits with zero radial velocity. Figure 4.3 presents a schematic representation of the circumstellar gas model.

Because the long-term radial evolution of the gas is unknown, the positions of the inner and outer

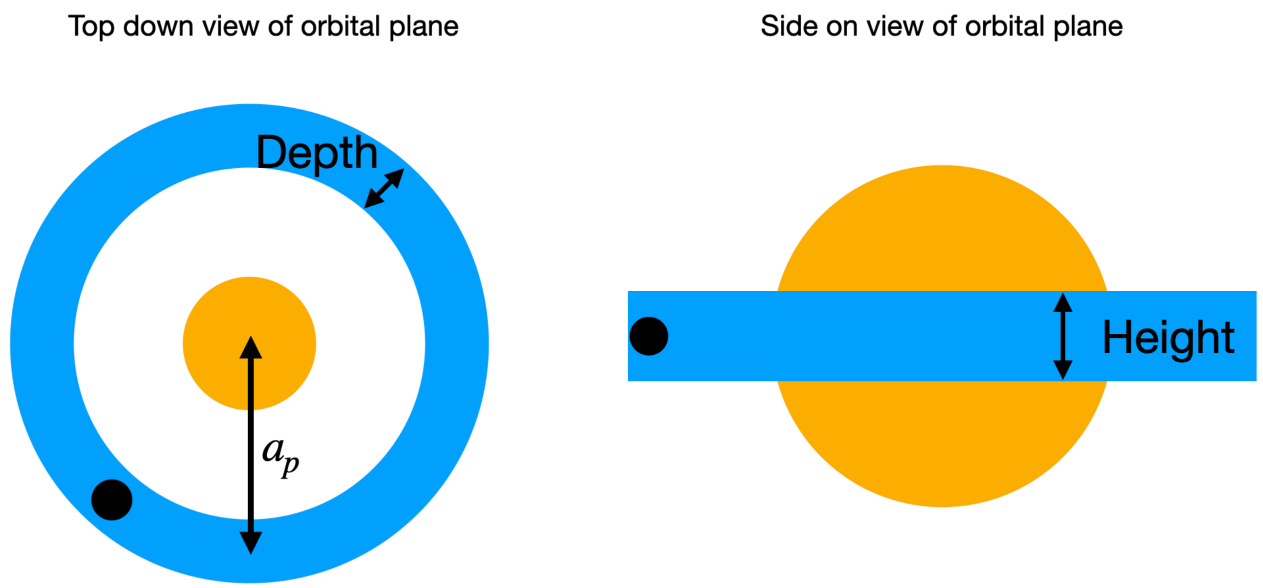

Figure 4.3: A schematic diagram of the circumstellar gas model. The gas is assumed to be azimuthally uniform, and is assumed to have constant height, depth and density.

edges of the disk are uncertain. In this work, I choose the inner edge and outer edge of the disk to be:

$$R_{\rm in} = a_p \tag{4.2}$$

$$R_{\rm out} = a_p + L_{\rm cor} \tag{4.3}$$

$$L_{\rm cor} \approx \frac{c_s}{2\Omega} \tag{4.4}$$

where a_p is the semi-major axis of the planet, c_s is the sound speed of the escaping gas and Ω is the angular velocity of the planet and $L_{\rm cor}$ is the distance the gas travels away from the planet before being deflected by the coriolis force (e.g., Owen et al., 2023). This corresponds to the case where the majority of gas is confined in a narrow ring exterior to the planet. Simulations investigating the evolution of this gas, taking into account viscous forces, gravitational interactions with the planet, and the interactions with the magnetosphere of the star are necessary to check this. Note, however, that line of sight optical depth is only weakly dependent on the radial density structure (for constant column density), through small changes to the ionization structure and vertical extent of the gas. As the gas exterior to the planet has a larger scale height (and hence vertical extent), this is likely to be the most important to setting the total absorption.

Observations are more sensitive to the height of the circumstellar gas since that determines the area of the stellar disk that is obscured. The circumstellar gas will be in vertical hydrostatic equilibrium with scale height:

$$h = \frac{c_s}{\Omega_k} \tag{4.5}$$

where Ω_k is the Keplerian angular velocity of this gas. To see this, consider the vertical sound crossing time of the gas t_{sc}:

$$t_{sc} = \frac{h}{c_s} = \frac{1}{\Omega_k} \sim \frac{1}{\Omega} \tag{4.6}$$

The final equivalence holds because the circumstellar gas is located near the planetary orbit. Therefore, the gas settles in a vertical hydrostatic equilibrium on the order of an planetary orbital period, much shorter than the lifetime of the disk. Given that the disk is narrow ($L_{\rm cor} \ll a_p$), the height remains approximately constant across the disk. Therefore, in this model, I take the height of the disk to be scale height of the gas evaluated at the middle of the disk, $R = \frac{1}{2}\left(R_{\rm in} + R_{\rm out}\right)$.

4.1.2 Mass of the disk

The gas density in the disk will continue to build as the planet loses mass. There are a variety of mechanisms that will stop this process from continuing indefinitely: accretion onto the star may balance the input of gas into the disk so that it reaches a steady state or the disk may become optically thick to EUV radiation so that EUV driven mass loss from the planet is shut down. In the latter, mass loss may shut down or continue via X-ray driven mass loss or Roche lobe overflow. Equally, a coronal mass ejection from the star may blow away the disk. Thus, the disk may not reach a steady state, and therefore may lead to variable signatures. In this work, I examine the case in which the mass of the circumstellar gas is limited by the disk becoming optically thick to EUV radiation. This assumption is not self-consistent with the choice of placing the gas exterior to the planet. However, the EUV limit provides a plausible mass scale for the gas.

The circumstellar gas, originating from the atmospheres of gas-rich planets, is predominantly hydrogen and helium containing trace amounts of heavier species. The optical depth to EUV radiation, $\tau_{\rm EUV}$ is dominated by neutral hydrogen and the gas column density which is marginally optically thick is approximately:

$$\tau_{\rm EUV} = N_{\rm HI}\sigma_{\rm phot} = 1 \tag{4.7}$$

where $N_{\rm HI}$ is the column density of neutral hydrogen and $\sigma_{\rm phot} = 6.3 \times 10^{-18}{\rm cm}^2$ is the threshold photoionization cross section of neutral hydrogen. The minimum density of gas in the disk can be approximated to be when the mass flow rate through a cross-sectional slice of the torus equals the planetary mass loss rate:

$$n_H = \frac{\dot{M}_p}{2L_{\rm cor}hc_s m_H} = \frac{\Omega^2\dot{M}_p}{c_s^3 m_H} \approx 2\times10^7\ {\rm cm}^{-3}\left(\frac{\dot{M}_p}{10^{11}\ {\rm g\ s}^{-1}}\right)\left(\frac{\Omega}{2\times10^{-5}\ {\rm s}^{-1}}\right)^2\left(\frac{c_s}{10\ {\rm km\ s}^{-1}}\right)^{-3} \tag{4.8}$$

The optically thin gas will be strongly ionized so that $n_e \approx n$, therefore the recombination time for a proton is:

$$\frac{1}{n_e\alpha_A} \approx 1\ {\rm days} \tag{4.9}$$

where $\alpha_A = 4.18\times10^{-13}\ {\rm cm}^3\ {\rm s}^{-1}$ is the Case A recombination coefficient for hydrogen at 10^4 K, which is the relevant recombination coefficient for an optically thin gas. The recombination timescale is short compared to the life of the disk so the gas quickly settles into photoionization-recombination equilibrium. In photoionization-recombination equilibrium, the equation for the fraction of ionized hydrogen is:

$$(1 - X_{\rm HII})\Gamma_H - n_{\rm H}X_{\rm HII}^2\alpha_A = 0 \tag{4.10}$$

where $X_{\rm HII}$ is the fraction of ionized hydrogen, Γ_H is the hydrogen photoionization rate, $n_{\rm H}$ is the number density of hydrogen (atomic and ionized). Solving for the fraction of ionized hydrogen gives:

$$X_{\rm HII} = \frac{\sqrt{\Gamma_H^2 + 4\alpha_A n_{\rm H}\Gamma_H} - \Gamma_H}{2\alpha_A n_{\rm H}} \tag{4.11}$$

The ionization fraction is density dependent, therefore the optical depth is:

$$\tau_{\rm EUV} = n_{\rm HI}\sigma_{\rm phot}w = (1 - X_{\rm HII})n_{\rm H}\sigma_{\rm phot}w = 1 \tag{4.12}$$

where w is the length of the gas column. Solving for n_H gives a maximum density of the gas:

$$n_H^{\rm max} = \frac{1}{\sigma_{\rm phot}w}\left(1 + \sqrt{\frac{\sigma_{\rm phot}w\Gamma}{\alpha_A}}\right) \tag{4.13}$$

For $w = L_{\rm cor}$ and $\Gamma_H = 10^3$, this gives a maximum mass of the circumstellar gas of:

$$M_{\rm disk} \approx 4\pi L_{\rm cor}hn_H^{\rm max}a_p m_p = \frac{2\pi c_s^2 n_H^{\rm max}a_p m_p}{\Omega^2} \approx 10^{18}\ {\rm g} \tag{4.14}$$

The time for this mass to built up is:

$$\frac{M_{\rm disk}}{\dot{M}_p} \sim 100\ {\rm days} \tag{4.15}$$

4.1.3 Ionization structure

The number density of the various species is obtained by calculating the ionization structure of the gas in the disk. This is done by computing the radiative transfer of stellar ionizing radiation through the disk. As the density of the disk is limited such that is optically thin to EUV radiation, the photoionization rate of a species is approximately constant throughout the disk. The optically thin ionization rate for a species is given by:

$$\Gamma = \int_{\nu_0}^{\infty} \frac{L_\nu}{4\pi r^2 h\nu}\sigma_\nu d\nu \tag{4.16}$$

where L_ν is the stellar luminosity, ν_0 is the photoionization threshold frequency and σ_ν is the photoionization cross section. To calculate these values, we numerically integrate equation 4.16 using analytic photoionization cross section fits presented in Verner et al. (1996) and stellar spectra from the MUSCLES library (e.g. France et al., 2016), which stitches a combination of observed and theoretical spectra to create template high energy spectra from the NUV to X-rays for different stellar types.

In photoionization equilibrium, the fraction of a species (of atomic number Z) in each ionization state is described by a system of equations:

$$X_i \Gamma_i - n_e X_{i+1} \alpha_i = 0 \qquad i = \{0, 1, ..., Z-1\} \tag{4.17}$$

where i ranges from the ground state to fully ionized, X_i is the ionization fraction, Γ_i is the photoionization rate, α_i is the Case A recombination coefficient (since the gas is optically thin) and n_e is the number density of electrons. The temperature dependent Case A recombination coefficients are taken from the CHIANTI database (Dere et al., 1997; Del Zanna et al., 2021). The number density of electrons depends on the ionization structure of all species therefore all the species are coupled. As the metallicity of the gas is low, we approximate the number density of electrons to be equal to the number density of electrons produced from the photoionization of hydrogen atoms, given in Equation 4.10. This decouples Equations 4.17, so that they each can be solved separately for each species using matrix inversion. This is done using a LU decomposition routine from LAPACK (Anderson et al., 1999).

Population of helium in the metastable triplet state

Helium needs to be considered separately since the 10830 Å absorption line of interest is from the metastable triplet state. To calculate the fraction of helium atoms in the triplet state, I use the method described in Chapter 3 (and Oklopčić & Hirata 2018).

4.2 Synthetic Observations

To perform synthetic observations of a star occulted by the torus, I use the same ray-tracing scheme as in Chapter 2, Section 2.4. For each species and line, the oscillator strengths and Einstein A coefficients needed to calculate the optical depth are taken from the CHIANTI atomic database (Dere et al., 1997; Del Zanna et al., 2021). For this calculation, the star's surface brightness is assumed to be spatially homogeneous. In reality, the brightness of stars is inhomogeneous, particularly in chromospheric lines that are dominated by active regions. Nevertheless, the large occulting area of the circumstellar gas likely covers both active and non-active regions, reducing the overall impact of surface inhomogeneity on the observed signal.

4.3 Results

I construct a synthetic ensemble of stars that host circumstellar gas and compare their characteristics to those of the field star sample presented by Smith (2016). This ensemble is generated by drawing a set of base stellar and planetary parameters from chosen distributions, as described below. From these, all other properties required to simulate the helium 10830 Å line can be derived from known relations. The drawn stellar parameters are: mass (M_*), helium 10830 Å EW, $\mathrm{L}_X/\mathrm{L}_{\mathrm{bol}}$ and the drawn planetary parameter is orbital period. The temperature of the circumstellar gas is fixed at 10^4 K, consistent with expectations for a hydrogen-dominated gas in ionization-recombination equilibrium and the EUV optical depth of the circumstellar gas is fixed at $\tau_{\mathrm{EUV}} = 0.1$.

As the He 10830 Å EW, log R'_{HK} and stellar $\mathrm{L}_X/\mathrm{L}_{\mathrm{bol}}$ are strongly correlated they cannot be drawn independently. Instead, these properties are jointly obtained by randomly drawing a star from the Smith (2016) sample with replacement. The mass of the star is drawn from a uniform distribution ranging from $0.45 M_\odot - 1.2 M_\odot$, for which the Smith (2016) correlation holds. From the mass, the radius and bolometric luminosity is calculated using the equations (from Demircan & Kahraman 1991):

$$\frac{R_*}{R_\odot} = 1.06 \left(\frac{M_*}{M_\odot} \right)^{0.945} \tag{4.18}$$

$$\frac{L_{*,\mathrm{bol}}}{L_{\odot,\mathrm{bol}}} = 1.02 \left(\frac{M_*}{M_\odot} \right)^{3.92} \tag{4.19}$$

The star is matched to a stellar type, which determines the shape of the spectrum in EUV. The template for each stellar type comes from the MUSCLES survey (France et al., 2016). The total stellar luminosity in the EUV band (defined as 124-912 Å) is calculated using the X-ray to EUV relations from King & Wheatley (2021). The template spectrum is then normalized to this value. For the stellar helium profile, I adopt a Gaussian shape corresponding to a thermally broadened line at 2.5×10^4 K, a corresponding to a typical upper chromospheric temperature, with the equivalent width corresponding to the drawn value for the star. The planetary orbital period (P) is drawn from a uniform distribution between 1 and 3 days, which is typical of hot Jupiter periods (Dawson & Johnson, 2018).

Using these parameters, I calculate the synthetic helium 10830 Å EW, accounting for obscuration by the circumstellar gas. For simplicity, I do not include any potential absorption in the Ca H & K lines from the circumstellar gas. Such absorption would shift the observed stellar properties even further from those of field stars. Figure 4.4 shows the comparison between the helium 10830 Å EW and log R'_{HK} for stars hosting circumstellar disks and the field star sample of Smith (2016). This illustrates that stars that host circumstellar gas are typically differentiable from field stars. A survey of stars hosting extreme hot Jupiters with the helium 10830 Å line will be able to show if these lie in a different part of parameter space than field stars.

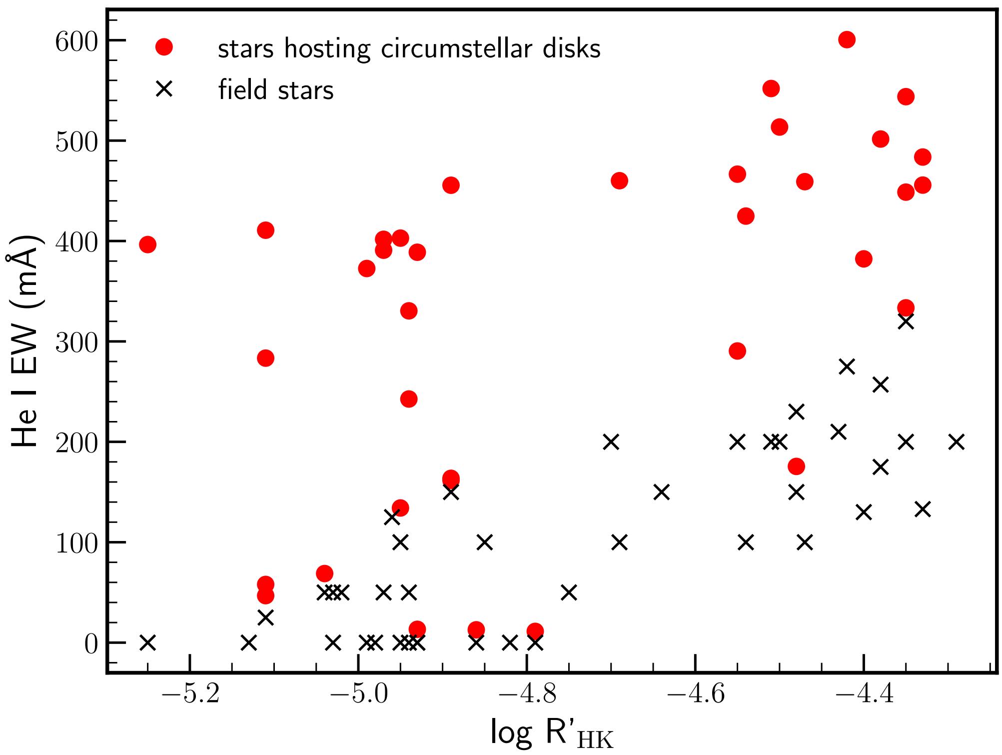

Figure 4.4: A synthetic population of stars hosting circumstellar disks compared to the field star sample from Smith (2016). Stars with circumstellar disks exhibit deeper helium absorption lines compared to field stars with similar log R'_{HK} values. This effect is significant enough to often make these stars stand out as outliers.

4.3.1 The effect of circumstellar gas on observed planetary transits

As the circumstellar gas obscures the star at specific wavelengths, it affects the observed 10830 Å transit of the planet, whose mass loss is generating the circumstellar gas in the first place. To investigate this, I separate the long-lived circumstellar gas and the planetary outflow inside the Hill sphere into components. I simulate the planetary outflow using PWINDS (Dos Santos et al., 2022) and perform synthetic 10830 Å planetary transits around stars hosting circumstellar gas of varying density.

Figure 4.5 illustrates the planet's excess absorption at mid-transit as the optical depth of the gas torus increases. When the torus is optically thin (blue line), the spectrum looks as expected in the absence of a circumstellar disk. However, as the optical depth increases (orange and green), the excess absorption weakens, particularly at the line center where the circumstellar gas is most opaque. When the torus is completely optically thick, the centre of the 10830 Å helium line is already fully absorbed by the torus, and therefore the planet does not contribute to any additional shrouding of the star at these wavelengths. Therefore, the planet actually appears to absorb less light at 10830 Å than in the optical, where the torus is optically thin. This results in a measured negative excess absorption.

The circumstellar gas also influences the transit light curve. The radial velocities of the planet and the circumstellar gas do not align throughout the entire transit because the gas and planet do not share the same orbit. When the radially velocities do not align, near ingress and egress, the circumstellar gas and the escaping planetary gas do not absorb at the same wavelengths meaning that the transit of the planet is not muted. However, when the radial velocities do align, such as near mid-transit, the circumstellar gas mutes the planet's absorption. In Figure 4.6, I plot the photometric 10830 Å transit of a planet around a star with and without a circumstellar disk. This was calculated by integrating in a 6 Å bin around line centre. The presence of circumstellar gas creates a distinctive W-shaped transit profile, with deeper absorption at ingress and egress compared to mid-transit. Notably, the transits of KELT-9 b (Lowson et al., 2023) and KELT-20 b (Casasayas-Barris et al., 2019), both orbiting A-type stars, have been observed to exhibit W-shaped profiles in H-α and other optical metal lines. These shapes have been attributed to center-to-limb variations in the stellar spectral lines. We speculate that a circumstellar gas torus around these stars may contribute to the formation of this W-shape.

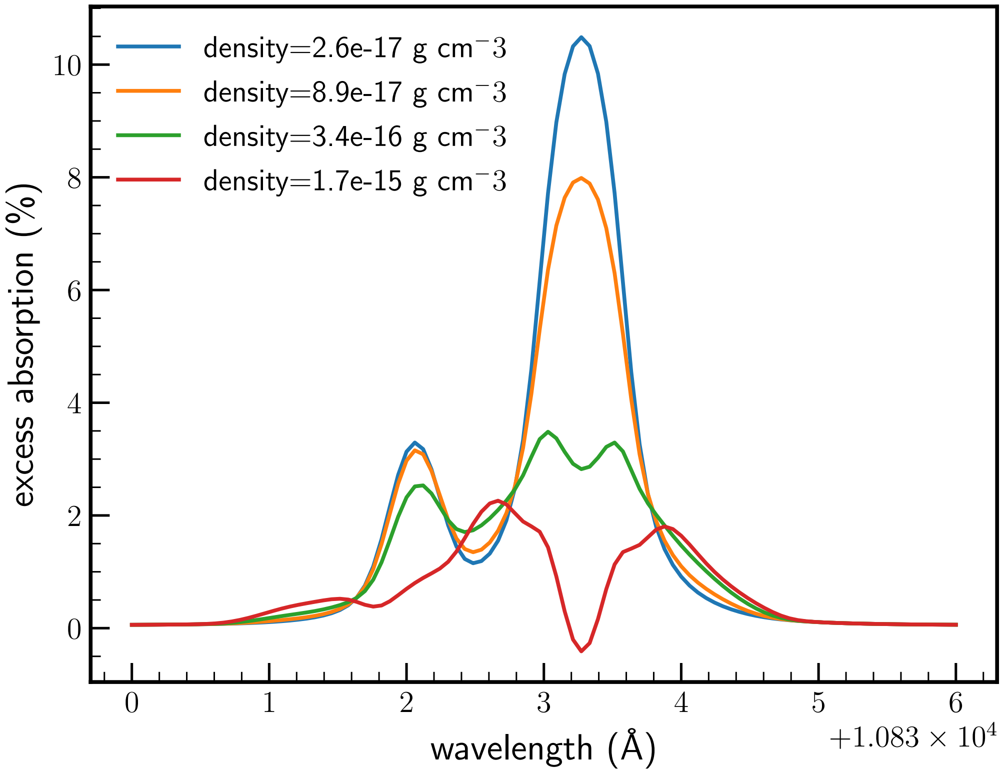

Figure 4.5: 10830 Å transmission spectra around 10830 Å for a planet with an escaping H/He atmosphere orbiting a star surrounded by a circumstellar disk. The lines illustrate how the observed excess absorption varies with the optical depth of the circumstellar gas at 10830 Å. At low optical depths (blue), the spectrum appears typical. However, as the circumstellar gas becomes optically thick (orange and green), the planet's ability to further dim the starlight is reduced, decreasing the measured excess absorption. In extreme cases (red), this can even result in a negative excess absorption, where the helium transit appears shallower than the planet's optical transit.

4.4 Discussion and Summary

The aim of this work was to develop a semi-analytical model of circumstellar gas produced by an evaporating planet and to highlight the key observable signatures of this gas. I have demonstrated that these stars hosting circumstellar gas can generally be distinguished from field stars by considering their helium 10830 Å EW and log R'_{HK}. In field stars, these properties are correlated, so deviations are unlikely to be of stellar origin and may indicate the presence of circumstellar gas. Additionally, I have also demonstrated that the presence of circumstellar gas can result in distinctive planetary transits, including W-shaped transits, when observed at wavelengths that are also absorbed by the circumstellar gas.

In the future, several limitations of this model should be addressed. First, full hydrodynamic (or

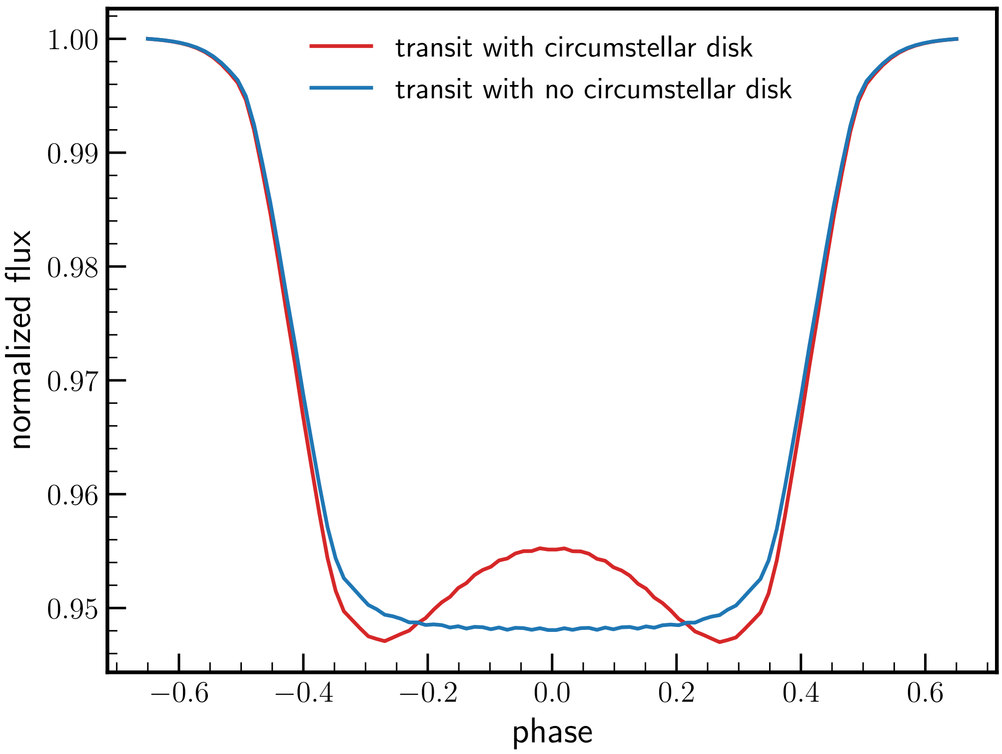

Figure 4.6: Helium light curve for a transiting planet with an escaping helium atmosphere around a star surrounded by a circumstellar disk. The presence of circumstellar gas creates a distinctive W-shaped transit profile (red), in contrast to the typical U-shaped profile (blue). At mid-transit, the line-of-sight velocities of the circumstellar gas and the planet align, muting the planet's transit signal. During ingress and egress, the velocity offset between the circumstellar gas and the planet prevents this muting, resulting in the characteristic W-shape.

magnetohydrodynamic) simulations, run over longer timescales, are needed to provide a more accurate representation of the circumstellar gas and to assess its stability across different regions of parameter space. Additionally, further investigation is required into the assumption that the gas remains optically thin to EUV radiation. This may not hold if mass loss continues via X-rays, Roche lobe overflow, or if the disk only extends beyond the planet's semi-major axis. If the gas becomes optically thick to EUV radiation, its temperature and ionization state would change, altering the observability of key spectral features. Understanding these effects is crucial for accurately modeling specific systems, such as WASP-12b, which are thought to host such disks.

Chapter 5

Summary and Outlook

In this thesis I have investigated atmospheric escape from close-in exoplanets. I have theoretically modelled the escape process, and using these models investigated what we can learn about the properties of planets and their escaping atmospheres.

5.1 Summary

In Chapter 2, I explored the Lyman-α transits of exoplanets experiencing mass loss. Guided by the results of hydrodynamics simulations, I developed a semi-analytical model for the outflow that determines its trajectory, ionization state, and 3D geometry from the properties of the escaping atmosphere, planet and star. I coupled this model with a ray-tracing routine to produce synthetic transits. To validate this approach, I successfully reproduced the outflow trajectories observed in 3D simulations. I applied the model by performing a retrieval on the transit spectrum of GJ 436 b, finding that the constraints on the planetary outflow velocity and mass-loss rates align with a photoevaporative wind scenario.

In Chapter 3, I presented a method to detect the magnetic fields of close-in exoplanets undergoing atmospheric escape using transit spectroscopy of the helium 10830 Å line. Building on previous research in hydrodynamic and magneto-hydrodynamic photoevaporation, I propose that planets with weak magnetic fields, which are unable to control the outflow's topology, produce blue-shifted transits due to day-to-night flows. In contrast, planets with strong magnetic fields suppress this flow, forcing the gas to follow a dipolar magnetic topology, resulting in unshifted or slightly red-shifted transit profiles. To test this concept, I post-processed existing 2D photoevaporation simulations, computing synthetic helium transit profiles. As expected, I found that hydrodynamically dominated outflows generate blue-shifted transits of order the sound speed. Meanwhile, strong surface magnetic fields lead to unshifted or sub-sound speed red-shifted profiles. Ground-based, high-resolution observations can distinguish between these different profiles, although uncertainties in orbital eccentricity often make it difficult to conclusively attribute velocity shifts to the outflow in individual planets. Interestingly, most observed helium profiles are blue-shifted, which I suggest is a tentative indication that many close-in planets have surface dipole magnetic field strengths $\lesssim 0.3$ G. This is in agreement with demographic arguments that require hydrodynamically controlled outflows to explain the position of the radius-gap.

In Chapter 4, I explore the detectability of circumstellar disks generated by mass loss from the atmospheres of close-in giant planets with helium 10830 Å observations. I speculate that combining helium 10830 Å and log R'_{HK} measurements of the star provides a more robust test of the presence of this gas than one of these alone. I showed that stars hosting these disks typically have a deeper helium 10830 Å EW than field stars with the same log R'_{HK}. I additionally showed that the presence of circumstellar disks may be inferred from transit observations of the planet, as they produce a distinctive W-shaped lightcurve.

5.2 Outlook

In this section, I discuss future avenues of research, in-light of the findings in this thesis.

5.2.1 Using Lyman-α transits to learn about the nature of escape and the composition of planets

One of the primary objectives of this thesis was the development of a semi-analytical model for Lyman-α transits, with the ultimate goal of using it to test theories of atmospheric escape. I demonstrated the utility of this model by performing a retrieval on the velocity-resolved Lyman-α transit of GJ 436 b. Encouragingly, the model successfully fit the data with parameters that matched expectations from theoretical models. However, fitting a single object is not enough to fully validate and calibrate this model. To further test this framework, and the physical understanding of Lyman-α transits developed over the past decade, it is necessary to extend this analysis to a larger sample of Lyman-α transits. The ideal approach would be to conduct a population-wide, homogeneous analysis of archival Lyman-α observations, shown in Figure 5.1. To date, no comprehensive, homogeneous analysis of Lyman-α transits has been performed. This broader study will show whether the current understanding of Lyman-α transits is sufficient to explain the observations or if revisions to the model are needed. This is crucial to confirm that Lyman-α transit observations can reliably and quantitatively constrain the properties of escaping planetary outflows.

This work is particularly necessary, as a large multi-cycle Hubble treasury program is underway to conduct a comprehensive survey of transiting exoplanets in Lyman-α, called STELα (Program Number 17804). This will significantly expand the current dataset, increasing the number of Lyman-α transits that have their full transit measured to around 20–23 planets, compared to the two currently available. As photoevaporative outflows are faster than core-powered mass loss ones, they are expected to lead to longer transits. Therefore with a sample of observed full transits, it will be possible to distinguish between these two mechanisms. The model I developed in Chapter 2 is able to put tight constraints on the outflow velocity therefore will enable this to be done.

It has recently been recognized that atmospheric escape can be used to constrain a planet's atmospheric metallicity (Piaulet-Ghorayeb et al., 2024). The outflow composition is important as the radiative properties and the mean molecular weight of the species impact key properties, such as the velocity and mass loss rate of the outflow. Outflows with higher metallicity have a greater mean molecular weight, which results in slower outflow velocities. As Lyman-α transits are a good measure of outflow

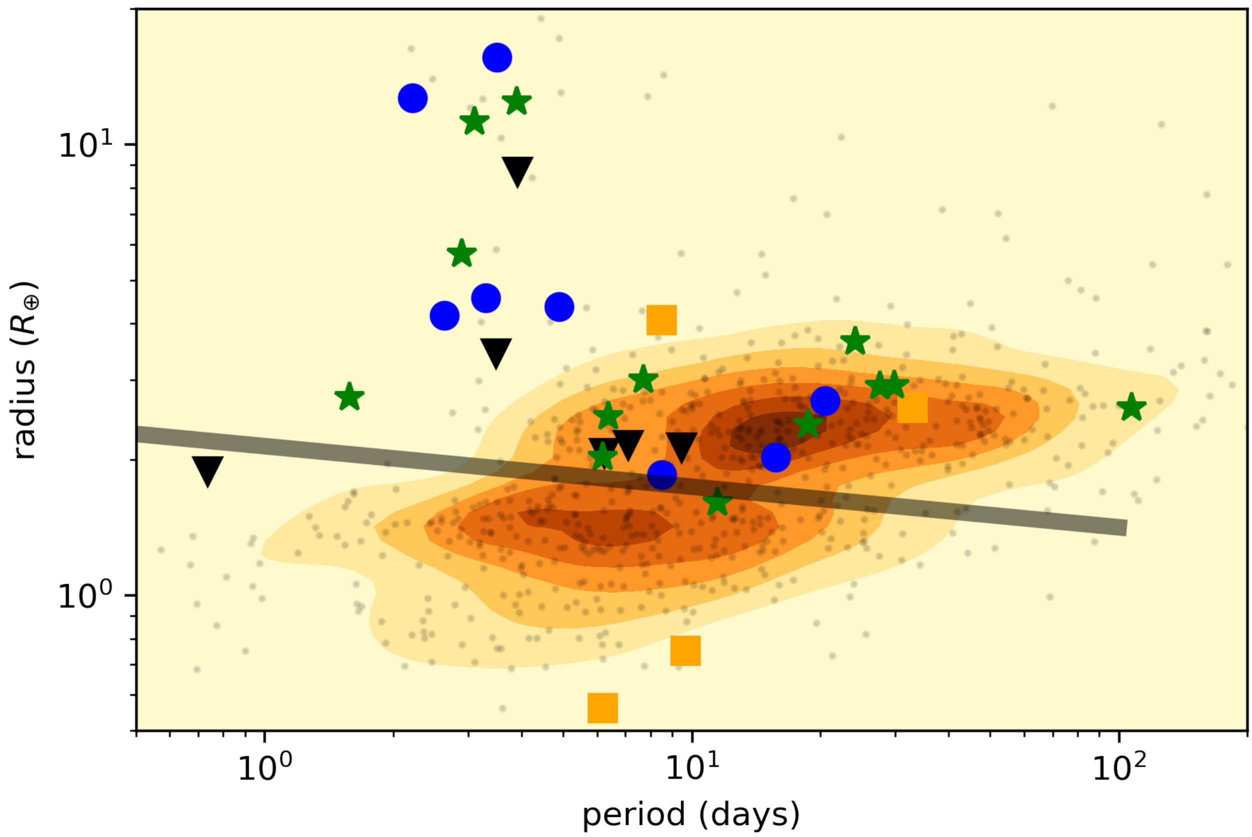

Figure 5.1: The archival Lyman-α transit sample plotted over the California Kepler Survey (CKS) planet sample (Petigura et al., 2017; Johnson et al., 2017). Blue circles are Ly-α detections, yellow squares are tentative detections and black triangles are non-detections. The green stars are datasets that are yet to be analysed. The black line marks the radius gap (Fulton et al., 2017)

velocities, they can be instrumental in distinguishing between these higher and lower metallicity scenarios.

This methodology was used to rule out the possibility that a TOI-776 c, a small planet with an intermediate density, is a water world. With the model developed in Chapter 2, I ran a retrieval on the Lyman-α transits of TOI-776 b & c, the results of which are shown in Figure 5.2.

For TOI-776 c, the retrieved mass loss rate of hydrogen is higher than that required to drag oxygen in the outflow, which is estimated using the formulism of (Hunten et al., 1987). Therefore, oxygen present at the base of the outflow should be entrained in the outflow. However, the presence of oxygen at mixing ratios greater than 10 % in the outflow requires unphysically high temperatures to match the sound speed of the transit. This rules out an outflow originating from a thermosphere of dissociated water, rich in oxygen. The constraints on TOI-776 b are not strong enough to come to the same conclusion. There are also JWST transit observations of TOI-776 b & c, thus there are potential avenues to combine lower atmosphere studies, done with JWST, and upper atmosphere studies, done with Lyman-α transits, to learn about the atmosphere of a planet more globally.

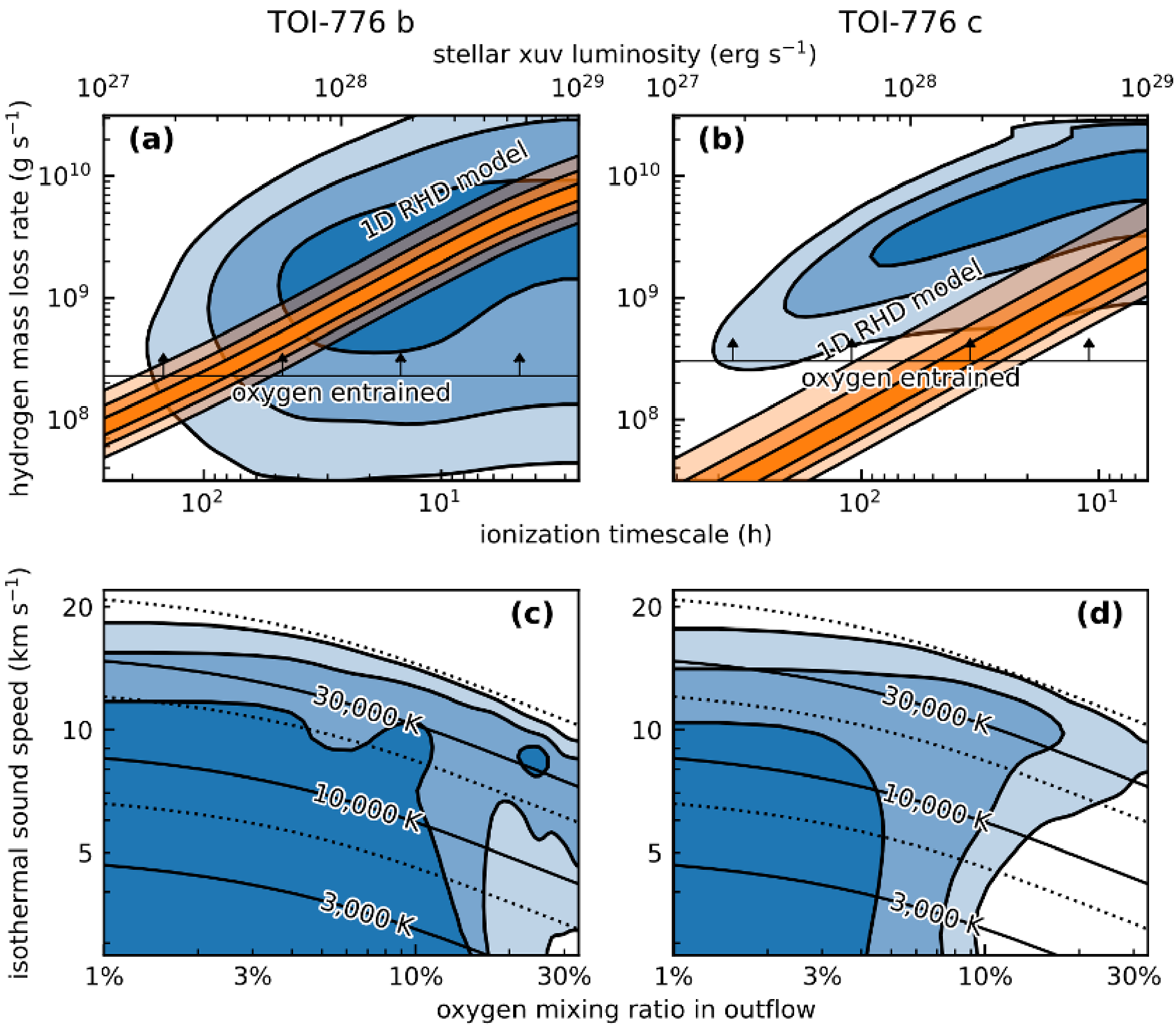

Figure 5.2: The blue contours show the posteriors from the fits to the Lyman-α transits of TOI-776 b & c. For TOI-776 c, the mass loss rate is high enough such that oxygen should be entrained in the flow. However, the retrieved sound speed is inconsistent with oxygen mixing ratios above 10 % for realistic outflow temperatures. This is inconsistent with the outflow coming from the steam dominated thermosphere of a water world.

In general, high metallicity outflows are not expected to produce strong Lyman-α signatures. These outflows are slow such that the hydrogen is ionized close to the planet and does not produce a large Lyman-α signal (Schulik, private communications). Consequently, Lyman-α transits are a good direct test of the metallicity of the atmosphere. STELα will observe the Lyman-α transit of tens of planets of unknown composition providing direct constraints of their atmospheric composition.

5.2.2 Expanding the tracers used to detect circumstellar disks

In Chapter 4, I discussed the absorption of helium 10830 Å from a circumstellar disk, formed through mass loss from a giant planet's atmosphere. I showed that stars hosting these disks typically have a deeper helium 10830 Å EW than field stars with the same log R'_{HK}. A natural next step to enhance this analysis would be to incorporate absorption from Ca II into this study, as observations indicate that this is present in the circumstellar gas (Haswell et al., 2012, 2020; Doherty, 2020). To achieve this, I plan to use HARPS-North spectra of stellar Ca H & K lines to create a template of these line profiles as a function of log R'_{HK}. These template spectra provide the unocculted stellar spectrum to which the absorption from Ca II in the circumstellar disk can be applied, allowing us to obtain the observed profile and hence the log R'_{HK}.

An avenue for future work would be to expand this analysis to include additional spectral lines. While helium 10830 Å is valuable, it is not a universal tracer due to its dependence on the underlying stellar spectrum. By incorporating multiple tracers, we could achieve broader coverage of these disks and gain further insights into their composition, ultimately improving our understanding of the structure of these disks and the outflows from hot Jupiters. For example, Hα is another promising tracer. Figure 5.3 illustrates the Hα transit of KELT-9 b, revealing an asymmetric, W-shaped profile. Similar to the effect seen with circumstellar disks, the star's rapid rotation modulates the transit differently at various phases, contributing to the W-shape. However, this center-to-limb variation alone cannot fully account for the observed asymmetry. Therefore, I speculate that a circumstellar disk around KELT-9 b may be contributing to the observed profile.

To accurately match observed profiles, more advanced models of these disks are required. One approach is to use FARGO simulations to study the evolution of the escaping gas. These simulations can account for viscous evolution, gravitational interactions between the planet and the circumstellar disk, and magnetic torques exerted on the disk by the star's magnetic field. Understanding these processes is crucial, as the torque exerted by the disk on the planet can drive planetary migration.

Therefore, refining these models is essential for studying the evolution of hot Jupiters.

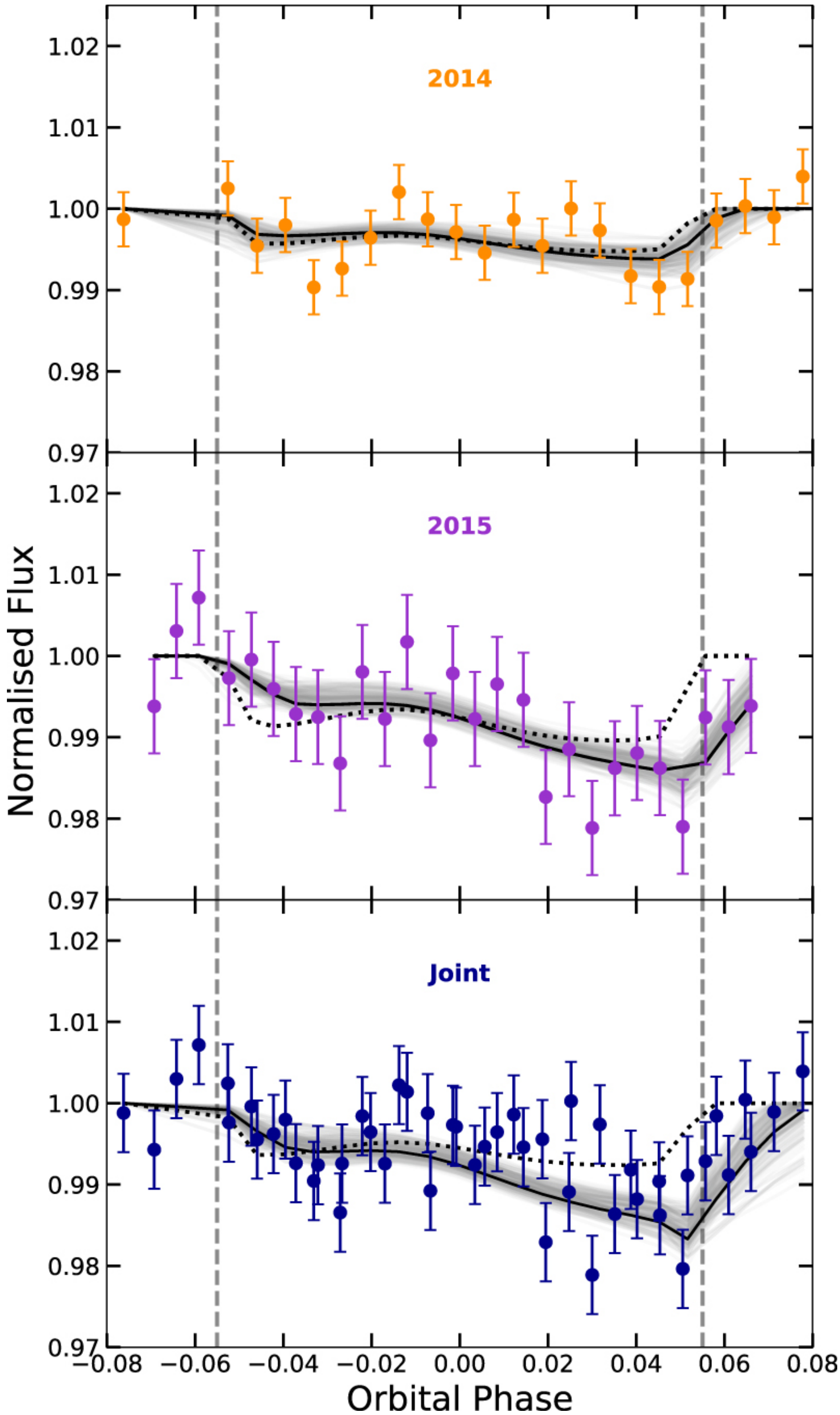

Figure 5.3: Transit lightcurves of KELT-9 b in Hα at different epochs. These profiles display a distinctive W-shape. The dotted line represents a synthetic light curve generated by modeling a spherical outflow transiting a rapidly rotating star (without a surrounding disk), but it does not fully capture the observed data. Figure from Lowson et al. (2023).

Bibliography

Adams F. C., 2011, ApJ, 730, 27

Adibekyan V., 2019, Geosciences, 9, 105

Allart R., et al., 2018, Science, 362, 1384

Alonso-Floriano F. J., et al., 2019, A&A, 629, A110

Anderson E., et al., 1999, LAPACK Users' Guide, third edn. Society for Industrial and Applied Mathematics, Philadelphia, PA

Andretta V., Giampapa M. S., 1995, ApJ, 439, 405

Arakcheev A. S., Zhilkin A. G., Kaigorodov P. V., Bisikalo D. V., Kosovichev A. G., 2017, Astronomy Reports, 61, 932

Baraffe I., Selsis F., Chabrier G., Barman T. S., Allard F., Hauschildt P. H., Lammer H., 2004, A&A, 419, L13

Bashi D., Helled R., Zucker S., Mordasini C., 2017, A&A, 604, A83

Bellotti S., et al., 2023, arXiv e-prints, p. arXiv:2306.15391

Ben-Jaffel L., et al., 2022, Nature Astronomy, 6, 141

Benneke B., et al., 2024, arXiv e-prints, p. arXiv:2403.03325

Biermann L., 1951, Z. Astrophys., 29, 274

Biermann L., 1952, Zeitschrift Naturforschung Teil A, 7, 127

Biermann L., 1957, The Observatory, 77, 109

Bisikalo D., Kaygorodov P., Ionov D., Shematovich V., Lammer H., Fossati L., 2013, ApJ, 764, 19

Borucki W. J., et al., 2011, ApJ, 736, 19

Bourrier V., Lecavelier des Etangs A., 2013, A&A, 557, A124

Bourrier V., Ehrenreich D., Lecavelier des Etangs A., 2015, A&A, 582, A65

Bourrier V., Lecavelier des Etangs A., Ehrenreich D., Tanaka Y. A., Vidotto A. A., 2016, A&A, 591, A121

Bourrier V., et al., 2018, A&A, 620, A147

Bourrier V., et al., 2022, A&A, 663, A160

Brain D. A., Kao M. M., O'Rourke J. G., 2024, arXiv e-prints, p. arXiv:2404.15429

Bray I., Burgess A., Fursa D. V., Tully J. A., 2000, A&AS, 146, 481

Brown R. L., 1971, ApJ, 164, 387

Byrne G. D., Hindmarsh A. C., 1975, ACM Trans. Math. Softw., 1, 71

Caldiroli A., Haardt F., Gallo E., Spinelli R., Malsky I., Rauscher E., 2022, A&A, 663, A122

Carolan S., Vidotto A. A., Villarreal D'Angelo C., Hazra G., 2021a, MNRAS, 500, 3382

Carolan S., Vidotto A. A., Hazra G., Villarreal D'Angelo C., Kubyshkina D., 2021b, MNRAS, 508, 6001

Carroll-Nellenback J., Frank A., Liu B., Quillen A. C., Blackman E. G., Dobbs-Dixon I., 2016, Monthly Notices of the Royal Astronomical Society, 466, 2458

Casasayas-Barris N., et al., 2019, A&A, 628, A9

Chabrier G., Baraffe I., 2000, ARA&A, 38, 337

Chance Q., Ballard S., Stassun K., 2022, ApJ, 937, 39

Chen J., Kipping D., 2017, ApJ, 834, 17

Christensen U. R., Holzwarth V., Reiners A., 2009, Nature, 457, 167

Christiansen J. L., et al., 2013, ApJS, 207, 35

Christie D., Arras P., Li Z.-Y., 2013, ApJ, 772, 144

Clarke C. J., Alexander R. D., 2016, Monthly Notices of the Royal Astronomical Society, 460, 3044

Connerney J. E. P., et al., 2022, Journal of Geophysical Research (Planets), 127, e07055

Cranmer S. R., 2004, American Journal of Physics, 72, 1397

Currie T., Biller B., Lagrange A., Marois C., Guyon O., Nielsen E. L., Bonnefoy M., De Rosa R. J., 2023, in Inutsuka S., Aikawa Y., Muto T., Tomida K., Tamura M., eds, Astronomical Society of the Pacific Conference Series Vol. 534, Protostars and Planets VII. p. 799 (`arXiv:2205.05696`), doi:10.48550/arXiv.2205.05696

Dattilo A., Batalha N. M., Bryson S., 2023, AJ, 166, 122

Dawson R. I., Johnson J. A., 2018, ARA&A, 56, 175

Debrecht A., Carroll-Nellenback J., Frank A., Fossati L., Blackman E. G., Dobbs-Dixon I., 2018, MNRAS, 478, 2592

Debrecht A., Carroll-Nellenback J., Frank A., Blackman E. G., Fossati L., McCann J., Murray-Clay R., 2020, MNRAS, 493, 1292

Debrecht A., Carroll-Nellenback J., Frank A., Blackman E. G., Fossati L., Murray-Clay R., McCann J., 2022, MNRAS,

Del Zanna G., Dere K. P., Young P. R., Landi E., 2021, ApJ, 909, 38

Demircan O., Kahraman G., 1991, Ap&SS, 181, 313

Dere K. P., Landi E., Mason H. E., Monsignori Fossi B. C., Young P. R., 1997, A&AS, 125, 149

Doherty J., 2020, Enshrouding & Star-planet Interactions in Close-orbiting Systems, Unpublished, https://oro.open.ac.uk/73559/

Dos Santos L. A., 2023, in Vidotto A. A., Fossati L., Vink J. S., eds, Vol. 370, Winds of Stars and Exoplanets. pp 56–71 (arXiv:2211.16243), doi:10.1017/S1743921322004239

Dos Santos L. A., et al., 2022, A&A, 659, A62

Drake G. W., 1971, Phys. Rev. A, 3, 908

Dressing C. D., et al., 2015, The Astrophysical Journal, 800, 135

Ehrenreich D., et al., 2015, Nature, 522, 459

Ferraz-Mello S., 2013a, Celestial Mechanics and Dynamical Astronomy, 116, 109

Ferraz-Mello S., 2013b, Celestial Mechanics and Dynamical Astronomy, 116, 109

Foreman-Mackey D., Hogg D. W., Lang D., Goodman J., 2013, PASP, 125, 306

Fortney J. J., 2005, MNRAS, 364, 649

Fortney J. J., Marley M. S., Barnes J. W., 2007, ApJ, 659, 1661

Fossati L., Ayres T. R., Haswell C. A., Bohlender D., Kochukhov O., Flöer L., 2013, ApJ, 766, L20

France K., et al., 2016, ApJ, 820, 89

Fu G., et al., 2022, ApJ, 940, L35

Fukue J., Okada R., 1990, PASJ, 42, 249

Fulton B. J., et al., 2017, The Astronomical Journal, 154, 109

García Muñoz A., Youngblood A., Fossati L., Gandolfi D., Cabrera J., Rauer H., 2020, ApJ, 888, L21

Gelman A., Carlin J. B., Stern H. S., Dunson D. B., Vehtari A., Rubin D. B., 2014, Bayesian Data Analysis

Ginzburg S., Schlichting H. E., Sari R., 2018, Monthly Notices of the Royal Astronomical Society, 476, 759

Giovanelli R. G., Hall D. N. B., Harvey J. W., 1972, Sol. Phys., 22, 53

Goodman J., Weare J., 2010, Communications in Applied Mathematics and Computational Science, 5, 65

Gordino M., et al., 2022, A&A, 657, A86

Green J., et al., 2012, arXiv e-prints, p. arXiv:1208.4012

Grießmeier J. M., et al., 2004, A&A, 425, 753

Gritschneder M., Naab T., Walch S., Burkert A., Heitsch F., 2009, ApJ, 694, L26

Gronoff G., et al., 2020, Journal of Geophysical Research (Space Physics), 125, e27639

Guilluy G., et al., 2020, A&A, 639, A49

Gully-Santiago M., et al., 2023, arXiv e-prints, p. arXiv:2307.08959

Gupta A., Schlichting H. E., 2019, Monthly Notices of the Royal Astronomical Society, 487, 24

Haswell C. A., 2010, Transiting Exoplanets

Haswell C. A., et al., 2012, ApJ, 760, 79

Haswell C. A., et al., 2020, Nature Astronomy, 4, 408

Hazra G., Vidotto A. A., Carolan S., Villarreal D'Angelo C., Manchester W., 2022, MNRAS, 509, 5858

Heng K., 2017, Exoplanetary Atmospheres: Theoretical Concepts and Foundations

Holmström M., Ekenbäck A., Selsis F., Penz T., Lammer H., Wurz P., 2008, Nature, 451, 970

Howard A. W., et al., 2012, ApJS, 201, 15

Hubbard W. B., Hattori M. F., Burrows A., Hubeny I., Sudarsky D., 2007, Icarus, 187, 358

Hummer D. G., Storey P. J., 1998, MNRAS, 297, 1073

Hunten D. M., Pepin R. O., Walker J. C. G., 1987, Icarus, 69, 532

Izidoro A., Schlichting H. E., Isella A., Dasgupta R., Zimmermann C., Bitsch B., 2022, ApJ, 939, L19

Jackson A. P., Davis T. A., Wheatley P. J., 2012, MNRAS, 422, 2024

Jensen A. G., Redfield S., Endl M., Cochran W. D., Koesterke L., Barman T., 2012, ApJ, 751, 86

Jin S., Mordasini C., 2018, The Astrophysical Journal, 853, 163

Jin S., Mordasini C., Parmentier V., van Boekel R., Henning T., Ji J., 2014, The Astrophysical Journal, 795, 65

Johnson J. A., et al., 2017, AJ, 154, 108

Johnstone C. P., Güdel M., Lammer H., Kislyakova K. G., 2018, A&A, 617, A107

Jontof-Hutter D., et al., 2016, ApJ, 820, 39

Kempton E. M. R., et al., 2023, Nature, 620, 67

Khodachenko M. L., Shaikhislamov I. F., Lammer H., Prokopov P. A., 2015, ApJ, 813, 50

Khodachenko M. L., Shaikhislamov I. F., Lammer H., Berezutsky A. G., Miroshnichenko I. B., Rumenskikh M. S., Kislyakova K. G., Dwivedi N. K., 2019, ApJ, 885, 67

Khodachenko M. L., Shaikhislamov I. F., Fossati L., Lammer H., Rumenskikh M. S., Berezutsky A. G., Miroshnichenko I. B., Efimof M. A., 2021, MNRAS, 503, L23

King G. W., Wheatley P. J., 2021, MNRAS, 501, L28

Kirk J., Alam M. K., López-Morales M., Zeng L., 2020, AJ, 159, 115

Kirk J., Dos Santos L. A., López-Morales M., Alam M. K., Oklopčić A., MacLeod M., Zeng L., Zhou G., 2022, AJ, 164, 24

Kislyakova K. G., Holmström M., Lammer H., Odert P., Khodachenko M. L., 2014, Science, 346, 981

Kite E. S., Barnett M. N., 2020, Proceedings of the National Academy of Science, 117, 18264

Kite E. S., Schaefer L., 2021, ApJ, 909, L22

Kramida A., Yu. Ralchenko Reader J., and NIST ASD Team 2022, NIST Atomic Spectra Database (ver. 5.10), [Online]. Available: `https://physics.nist.gov/asd` [2017, April 9]. National Institute of Standards and Technology, Gaithersburg, MD.

Kreidberg L., et al., 2014, Nature, 505, 69

Krista L. D., 2011, PhD thesis, University of Dublin Trinity College, Ireland

Kubyshkina D., et al., 2018, A&A, 619, A151

Kulow J. R., France K., Linsky J., Loyd R. O. P., 2014, ApJ, 786, 132

Landsman W., Simon T., 1993, ApJ, 408, 305

Lavie B., et al., 2017, A&A, 605, L7

Lecavelier des Etangs A., Vidal-Madjar A., McConnell J. C., Hébrard G., 2004, A&A, 418, L1

Lee E. J., Chiang E., Ormel C. W., 2014, ApJ, 797, 95

Linssen D. C., Oklopčić A., 2023, A&A, 675, A193

Lopez E. D., Fortney J. J., 2013, ApJ, 776, 2

Lowson N., et al., 2023, AJ, 165, 101

Loyd R. O. P., et al., 2016, ApJ, 824, 102

Lundkvist M. S., et al., 2016, Nature Communications, 7, 11201

MacLeod M., Oklopčić A., 2022, ApJ, 926, 226

Madhusudhan N., Sarkar S., Constantinou S., Holmberg M., Piette A. A. A., Moses J. I., 2023, ApJ, 956, L13

Malsky I., Rogers L. A., 2020, ApJ, 896, 48

Martin W. C., 1973, Journal of Physical and Chemical Reference Data, 2, 257

Matsakos T., Königl A., 2016, ApJ, 820, L8

Matsakos T., Uribe A., Königl A., 2015, A&A, 578, A6

Mayor M., Queloz D., 1995, Nature, 378, 355

McCann J., Murray-Clay R. A., Kratter K., Krumholz M. R., 2019, ApJ, 873, 89

Melo C., Santos N. C., Pont F., Guillot T., Israelian G., Mayor M., Queloz D., Udry S., 2006, A&A, 460, 251

Melosh H. J., Vickery A. M., 1989, Nature, 338, 487

Misener W., Schlichting H. E., 2021, MNRAS, 503, 5658

Misener W., Schulik M., Schlichting H. E., Owen J. E., 2024, arXiv e-prints, p. arXiv:2405.15221

Morton T. D., Swift J., 2014, ApJ, 791, 10

Murray C. D., Correia A. C. M., 2010, in Seager S., ed., , Exoplanets. pp 15–23, doi:10.48550/arXiv.1009.1738

Murray-Clay R. A., Chiang E. I., Murray N., 2009, ApJ, 693, 23

Nortmann L., et al., 2018, Science, 362, 1388

Oklopčić A., 2019, ApJ, 881, 133

Oklopčić A., Hirata C. M., 2018, ApJ, 855, L11

Orell-Miquel J., et al., 2022, A&A, 659, A55

Orell-Miquel J., et al., 2024, arXiv e-prints, p. arXiv:2404.16732

Osterbrock D. E., Ferland G. J., 2006, Astrophysics of gaseous nebulae and active galactic nuclei. University Science Books

Owen J. E., 2019, Annual Review of Earth and Planetary Sciences, 47, 67

Owen J. E., Adams F. C., 2014, MNRAS, 444, 3761

Owen J. E., Adams F. C., 2019, MNRAS, 490, 15

Owen J. E., Alvarez M. A., 2016, ApJ, 816, 34

Owen J. E., Jackson A. P., 2012, MNRAS, 425, 2931

Owen J. E., Lai D., 2018, MNRAS, 479, 5012

Owen J. E., Schlichting H. E., 2024, MNRAS, 528, 1615

Owen J. E., Wu Y., 2013, ApJ, 775, 105

Owen J. E., Wu Y., 2017, The Astrophysical Journal, 847, 29

Owen J. E., et al., 2023, MNRAS, 518, 4357

Palle E., et al., 2020, A&A, 638, A61

Parc L., Bouchy F., Venturini J., Dorn C., Helled R., 2024, A&A, 688, A59

Parker E. N., 1958, ApJ, 128, 664

Patapis P., et al., 2022, A&A, 658, A72

Perryman M., Hartman J., Bakos G. Á., Lindegren L., 2014, ApJ, 797, 14

Petigura E. A., et al., 2017, AJ, 154, 107

Petzold L., 1983, SIAM Journal on Scientific and Statistical Computing, 4, 136

Piaulet-Ghorayeb C., et al., 2024, ApJ, 974, L10

Pinto C., Galli D., 2008, A&A, 484, 17

Piso A.-M. A., Youdin A. N., 2014, ApJ, 786, 21

Raga A. C., Cabrit S., Canto J., 1995, MNRAS, 273, 422

Roberge W., Dalgarno A., 1982, ApJ, 255, 489

Rocha-Pinto H. J., Maciel W. J., 1998, MNRAS, 298, 332

Rockcliffe K. E., Newton E. R., Youngblood A., Duvvuri G. M., Plavchan P., Gao P., Mann A. W., Lowrance P. J., 2023, AJ, 166, 77

Rogers J. G., Owen J. E., 2021, MNRAS, 503, 1526

Rogers L. A., Bodenheimer P., Lissauer J. J., Seager S., 2011, ApJ, 738, 59

Rogers J. G., Owen J. E., Schlichting H. E., 2024a, MNRAS, 529, 2716

Rogers J. G., Schlichting H. E., Young E. D., 2024b, ApJ, 970, 47

Salz M., et al., 2018, A&A, 620, A97

Sanz-Forcada J., Dupree A. K., 2008, A&A, 488, 715

Schlichting H. E., Sari R., Yalinewich A., 2015, Icarus, 247, 81

Schreyer E., Owen J. E., Loyd R. O. P., Murray-Clay R., 2024, MNRAS, 533, 3296

Schulik M., Booth R. A., 2023, MNRAS, 523, 286

Schulreich M. M., Breitschwerdt D., 2011, A&A, 531, A13

Schultz D. R., Krstic P. S., Lee T. G., Raymond J. C., 2008, ApJ, 678, 950

Schunk R. W., Nagy A. F., 1980, Reviews of Geophysics and Space Physics, 18, 813

Shematovich V. I., Ionov D. E., Lammer H., 2014, A&A, 571, A94

Silva Aguirre V., et al., 2015, MNRAS, 452, 2127

Sing D. K., et al., 2019, AJ, 158, 91

Smith G. H., 2016, Publ. Astron. Soc. Australia, 33, e057

Spake J. J., et al., 2018, Nature, 557, 68

Spake J. J., Oklopčić A., Hillenbrand L. A., 2021, AJ, 162, 284

Spake J. J., et al., 2022, ApJ, 939, L11

Spitzer L., 1978, Physical processes in the interstellar medium, doi:10.1002/9783527617722.

Stevenson D. J., 2003, Earth and Planetary Science Letters, 208, 1

Stone J. M., Proga D., 2009, ApJ, 694, 205

Szabó G. M., Kiss L. L., 2011, The Astrophysical Journal, 727, L44

Tanaka Y. A., Suzuki T. K., Inutsuka S.-i., 2014, ApJ, 792, 18

Tian F., Toon O. B., Pavlov A. A., De Sterck H., 2005, ApJ, 621, 1049

Trammell G. B., Arras P., Li Z.-Y., 2011, ApJ, 728, 152

Trammell G. B., Li Z.-Y., Arras P., 2014, The Astrophysical Journal, 788, 161

Tremblin P., Chiang E., 2012, Monthly Notices of the Royal Astronomical Society, 428, 2565

Tripathi A., Kratter K. M., Murray-Clay R. A., Krumholz M. R., 2015, ApJ, 808, 173

Tsapras Y., 2018, Geosciences, 8, 365

Valencia D., Ikoma M., Guillot T., Nettelmann N., 2010, A&A, 516, A20

Valsecchi F., Rasio F. A., Steffen J. H., 2014, ApJ, 793, L3

Valsecchi F., Rappaport S., Rasio F. A., Marchant P., Rogers L. A., 2015, ApJ, 813, 101

Van Eylen V., Albrecht S., 2015, ApJ, 808, 126

Van Eylen V., Agentoft C., Lundkvist M. S., Kjeldsen H., Owen J. E., Fulton B. J., Petigura E., Snellen I., 2018, Monthly Notices of the Royal Astronomical Society, 479, 4786

Van Eylen V., et al., 2019, AJ, 157, 61

Verner D. A., Ferland G. J., Korista K. T., Yakovlev D. G., 1996, ApJ, 465, 487

2023, Winds of Stars and Exoplanets Vol. 370, doi:10.1017/S1743921323001011.

Vidal-Madjar A., Lecavelier des Etangs A., Désert J. M., Ballester G. E., Ferlet R., Hébrard G., Mayor M., 2003, Nature, 422, 143

Villarreal D'Angelo C., Vidotto A. A., Esquivel A., Hazra G., Youngblood A., 2021, MNRAS, 501, 4383

Virtanen P., et al., 2020, Nature Methods, 17, 261

Vissapragada S., et al., 2022, AJ, 164, 234

Wallack N. L., et al., 2024, AJ, 168, 77

Wang L., Dai F., 2021, ApJ, 914, 99

Waugh 1961, Technical report, Evaluation Of Integral Of Elliptic Gaussian Distribution Over A Centred Ellipse, `https://apps.dtic.mil/sti/pdfs/AD0271430.pdf`. U.S Navy, `https://apps.dtic.mil/sti/pdfs/AD0271430.pdf`

Wilson D. J., et al., 2022, ApJ, 936, 189

Winn J. N., 2010, in Seager S., ed., , Exoplanets. pp 55–77

Wogan N. F., Batalha N. E., Zahnle K. J., Krissansen-Totton J., Tsai S.-M., Hu R., 2024, ApJ, 963, L7

Wolszczan A., Frail D. A., 1992, Nature, 355, 145

Wood B. E., Redfield S., Linsky J. L., Müller H.-R., Zank G. P., 2005, ApJS, 159, 118

Wood B. E., et al., 2021, ApJ, 915, 37

Xing L., Yan D., Guo J., 2023, ApJ, 953, 166

Yan F., Henning T., 2018, Nature Astronomy, 2, 714

Yan D., Guo J., Huang C., Xing L., 2021, ApJ, 907, L47

Yelle R. V., 2004, Icarus, 170, 167

Youngblood A., et al., 2016, ApJ, 824, 101

Zhang M., Knutson H. A., Wang L., Dai F., Barragán O., 2022a, AJ, 163, 67

Zhang M., et al., 2022b, AJ, 163, 68

Zhang Z., et al., 2023a, Science Advances, 9, eadf8736

Zhang M., Knutson H. A., Dai F., Wang L., Ricker G. R., Schwarz R. P., Mann C., Collins K., 2023b, AJ, 165, 62

Zirin H., 1982, ApJ, 260, 655

dos Santos L. A., et al., 2019, A&A, 629, A47

dos Santos L. A., et al., 2020, A&A, 634, L4